# DEVELOPMENT AND INVESTIGATION OF ALKALINE ELECTROLYTE BASED DIRECT AMMONIA FUEL CELLS

**By**

**OSAMAH SIDDIQUI**

**A Thesis Submitted in Partial Fulfillment**

**of the Requirements for the degree of Master of Applied Science**

**in**

**Mechanical Engineering**

**University of Ontario Institute of Technology**

**Faculty of Engineering and Applied Science**

**Oshawa, Ontario, Canada**

## ABSTRACT

In the present thesis study, alkaline electrolyte based direct ammonia fuel cells are developed, and their performances are evaluated through various parameters and efficiencies, such as open circuit voltages, polarization curves, peak power densities and energy and exergy efficiencies. The open circuit voltage and peak power density for the anion exchange membrane based direct ammonia single-cell fuel cell are observed to be 279 mV and 19.2 $W/m^2$ respectively, and the energy and exergy efficiencies are evaluated to be 15.2% and 14.4% respectively. Furthermore, a molten alkaline electrolyte based fuel cell provides an open circuit voltage and peak power density of 520 mV and 2.1 $W/m^2$ respectively. The energy and exergy efficiencies for this type of fuel cell are evaluated to be 24.9% and 23.4%. Lastly, a novel hybrid ammonia fuel cell and battery system is developed that provides an energy efficiency of 27.5% and an exergy efficiency of 27.5%.



**Keywords:** Ammonia fuel cell; alkaline electrolyte; open circuit voltage; peak power density; energy; exergy; efficiency

## ACKNOWLEDGEMENTS

I express my earnest gratitude, respect, appreciation and love for my supervisor, mentor and teacher Professor Dr. Ibrahim Dincer. Professor Dincer's stellar support, confidence, energy and exergy kept me motivated and inspired throughout my degree. Working under his supervision helped me comprehend the difference between a person's energy and exergy. His continuous support and guidance were significant for the successful completion of this thesis. His outstanding comprehension and experience helped me overcome various obstacles during my research. Through his wise supervision, he trained and educated me about various technical and non-technical aspects and instilled in me the immense passion he entails.

In addition, I am grateful to Dr. Calin Zamfirescu for his help in the experimental measurements during my research. Furthermore, I am thankful to Mr. Ghassan Chehade for the help he provided at the Clean Energy Research Laboratory. Moreover, I am thankful to Professor Bekir Sami Yilbas for his support. Also, I express my gratitude towards all my colleagues and friends from the ACE 3030B lab.

Furthermore, I am thankful to my uncle Mr. Shahed Siddiqui for his continuous assistance and support throughout my stay in Canada.

The most sincere and honest relation in this world comprises of parents. I express my utmost appreciation, love and thankfulness for my beloved parents Mr. Abdul Bari Siddiqui and Mrs. Nusrat Sultana for their continuous prayers, support, help, guidance and supervision. In addition, I am thankful to all my siblings. I hope to serve them all with the best of my abilities.

## TABLE OF CONTENTS

**ABSTRACT** ii

**ACKNOWLEDGEMENTS** iii

**TABLE OF CONTENTS** iv

**LIST OF FIGURES** vi

**LIST OF TABLES** vii

**NOMENCLATURE** ix

**CHAPTER 1 : INTRODUCTION** 1

1.1 Significance of renewable energy resources 1

1.2 Hydrogen as an energy carrier 1

1.3 Challenges associated with hydrogen 3

1.4 Energy from Ammonia 3

1.5 Methods utilized for ammonia production 5

1.6 Direct ammonia fuel cells 7

1.7 Motivation 8

1.8 Objectives 8

**CHAPTER 2 : LITERATURE REVIEW** 10

2.1 Oxygen anion conducting electrolyte based solid oxide fuel cells (SOFC-O) 10

2.2 Proton conducting electrolyte based solid oxide fuel cells (SOFC-H) 13

2.4 Ammonia borane fuel cells 16

2.5 Alkaline electrolyte-based direct ammonia fuel cells 16

2.6 Gaps in the literature 19

**CHAPTER 3 : EXPERIMENTAL APPARATUS AND PROCEDURE** 21

3.1 Fuel cell components 21

3.1.1 Anion exchange membrane 21

3.1.2 Gas diffusion layers 23

3.1.3 Flow channel plates 24

3.1.5 Gaskets 26

3.1.6 End plates 26

3.1.7 Humidifier 27

3.1.8 Fuel cell stack assembly 27

3.2 Measurement devices 31

3.2.1 Potentiostat ..... 31
3.2.2 Flow meters ..... 32
3.2.3 Thermocouples ..... 33
3.3 Experimental setup for the anion exchange membrane-based direct ammonia fuel cell ..... 33
3.4 Experimental setup for a molten alkaline electrolyte based direct ammonia fuel cell ..... 36
**CHAPTER 4 : ANALYSIS AND MODELLING ..... 38**
4.1 Thermodynamic and electrochemical modelling ..... 38
4.2 Electrochemical impedance spectroscopy modeling ..... 42
4.3 Modelling of a novel hybrid system ..... 44
4.3.1 System description ..... 44
4.3.2 Analysis ..... 46
**CHAPTER 5 : RESULTS AND DISCUSSION ..... 50**
5.1 Performance results of the single-cell anion exchange membrane direct ammonia fuel cell ..... 50
5.2 Effects of humidifier temperature on the performance of the single-cell arrangement fuel cell ..... 54
5.3 Performance results of anion exchange membrane direct ammonia fuel cell with aqueous ammonia as fuel ..... 58
5.4 Performance results of a five-cell anion exchange membrane direct ammonia fuel cell stack ..... 62
5.5 Effects of humidifier temperature on the performance of five-cell fuel cell stack . 65
5.6 Performance comparison with literature studies ..... 70
5.7 Electrochemical impedance spectroscopy results ..... 71
5.7 Molten alkaline electrolyte based direct ammonia fuel cell results ..... 74
5.8 Hybrid ammonia fuel cell and battery system results ..... 76
5.8.1 Effects of electrolyte concentration on the fuel cell and battery performance . 77
5.8.2 Effects of operating temperature on the fuel cell and battery performance ..... 79
5.8.3 Effects of input ammonia pressure on the fuel cell performance ..... 81
5.8.4 Effects of KOH concentration on the fuel cell energy and exergy efficiencies 81
5.8.5 Advantages and disadvantages of the hybrid ammonia fuel cell and battery system ..... 86
5.9 Comparison of energy and exergy efficiencies ..... 87

**CHAPTER 6 : CONCLUSIONS AND RECOMMENDATIONS..... 88**
6.1 Conclusions ..... 88
6.2 Recommendations ..... 90

## LIST OF FIGURES

Fig. 1.1 Breakdown of global energy resources utilized for electricity generation as of 2015 (data from [10]). 2
Fig. 1.2 Capacity of hydrogen production from U.S. refineries (data from [22]). 2
Fig. 1.3 Rise in global ammonia production (data from [50]). 4
Fig. 1.4 Various possible routes for energy from ammonia 5
Fig. 1.5 Different types of direct ammonia fuel cells 7
Fig. 2.1 Working principle of SOFC-O 11
Fig. 2.2 Working principle of SOFC-H. 13
Fig. 3.1 Quaternary ammonium cation 21
Fig. 3.2 Anion exchange membrane 22
Fig. 3.3 Gas diffusion layer 24
Fig. 3.4 Flow channel plate 25
Fig. 3.5 Rubber gaskets for bipolar plates 26
Fig. 3.6 Fuel cell endplate 27
Fig. 3.7 Steps in the development of direct ammonia fuel cell: (A) Anion exchange membrane, (B) Membrane electrode assembly, (C) Preparing flow channel plates sealed with rubber gaskets, (D) Membrane electrode assembly sandwiched between two flow channel plates, (E) Flow channel plates and membrane electrode assembly place with the end plate, (F) Top plate enclosing the assembly, (G) Tightening of assembly with washers and nuts. 28
Fig. 3.8 Exploded view of the single cell fuel cell assembly 29
Fig. 3.9 CAD model of single cell assembly 30
Fig. 3.10 Five-cell direct ammonia fuel cell stack 31
Fig. 3.11 CAD model of the five-cell direct ammonia fuel cell stack 31
Fig. 3.12 Schematic of direct ammonia anion exchange membrane fuel cell 33
Fig. 3.13 Experimental setup to test the fuel cell performance. 34
Fig. 3.14 Schematic of the experimental setup with gaseous ammonia 35
Fig. 3.15 Schematic of the experimental setup with aqueous ammonia 35
Fig. 3.16 Schematic representing the experimental setup utilized to test the molten alkaline electrolyte based direct ammonia fuel cell 37
Fig. 4.1 Electrochemical impedance equivalent circuit model 43
Fig. 4.2 Schematic of proposed regenerative-electrode hybrid ammonia fuel cell-battery system. 45
Fig. 5.1 Schematic representing short-circuit currents due to fuel cross over 50
Fig. 5.2 Experimental and theoretical voltage vs current curves 52
Fig. 5.3 Experimental and theoretical power density vs current density curves 52
Fig. 5.4 Voltage vs current density curves for a humidifier temperature of 25$^{o}$C 53
Fig. 5.5 Power density vs current density curves for a humidifier temperature of 25$^{o}$C 53
Fig. 5.6 Voltage vs current density curves for a humidifier temperature of 60$^{o}$C 55
Fig. 5.7 Power density vs current density curves for a humidifier temperature of 60$^{o}$C 55
Fig. 5.8 Voltage vs current density curves for a humidifier temperature of 80$^{o}$C 56
Fig. 5.9 Power density vs current density curves for a humidifier temperature of 80$^{o}$C 57
Fig. 5.10 Average voltage vs current density curves for varying humidifier temperatures 57
Fig. 5.11 Average power density vs current density curves for varying humidifier temperatures 58

Fig. 5.12 Voltage vs current density curves for aqueous ammonia at 25ºC ..... 59
Fig. 5.13 Power density vs current density curves for aqueous ammonia at 25ºC ..... 60
Fig. 5.14 Voltage vs current density curves for aqueous ammonia at 45ºC ..... 60
Fig. 5.15 Power density vs current density curves for aqueous ammonia at 45ºC ..... 61
Fig. 5.16 Voltage vs current density curves for aqueous ammonia at 65ºC ..... 62
Fig. 5.17 Power density vs current density curves for aqueous ammonia at 65ºC ..... 63
Fig. 5.18 Average voltage vs current density curves for varying solution temperatures ..... 63
Fig. 5.19 Average power density vs current density curves for varying solution temperatures .... 64
Fig. 5.20 Voltage vs current density curves for a five-cell stack and humidifier temperature of 25ºC ..... 64
Fig. 5.21 Power density vs current density curves for a five-cell stack and humidifier temperature of 25ºC ..... 65
Fig. 5.22 Voltage vs current density curves for a five-cell stack and humidifier temperature of 60ºC ..... 66
Fig. 5.23 Power density vs current density curves for a five-cell stack and humidifier temperature of 60ºC ..... 67
Fig. 5.24 Voltage vs current density curves for a five-cell stack and humidifier temperature of 80ºC ..... 67
Fig. 5.25 Power density vs current density curves for a five-cell stack and humidifier temperature of 80ºC ..... 68
Fig. 5.26 Average voltage vs current density curves for five-cell stack for varying humidifier temperatures. ..... 68
Fig. 5.27 Average power density vs current density curves for five-cell stack for varying humidifier temperatures ..... 69
Fig. 5.28 A comparison of open circuit voltage obtained for the anion exchange membrane direct ammonia fuel cell in the current study with other previous studies ..... 70
Fig. 5.29 A benchmarking of open circuit voltage at 100 $A/m^2$ current density obtained for the single cell anion exchange membrane direct ammonia fuel cell ..... 71
Fig. 5.30 A benchmarking of power density at 100 $A/m^2$ current density obtained for the single cell anion exchange membrane direct ammonia fuel cell ..... 71
Fig. 5.31 Bode plot obtained from electrochemical impedance spectroscopy ..... 73
Fig. 5.32 Nyquist plot obtained from electrochemical impedance spectroscopy ..... 73
Fig. 5.33 Voltage vs current density curves for varying electrolyte temperatures for the molten alkaline electrolyte based direct ammonia fuel cell ..... 75
Fig. 5.34 Voltage vs current density curves for varying electrolyte temperatures for the molten alkaline electrolyte based direct ammonia fuel cell ..... 75
Fig. 5.35 Comparison of energy and exergy efficiencies of the molten alkaline electrolyte based direct ammonia fuel cell at varying electrolyte temperatures ..... 76
Fig. 5.36 Comparison of open circuit voltages between present study fuel cell system (PS:FC), present study battery system (PS:B), silver based thermally regenerative ammonia battery (Ag-TRAB), copper based thermally regenerative ammonia battery (Cu-TRAB) and chemically regenerative redox cathode (CRRC) polymer electrolyte fuel cell. ..... 77
Fig. 5.37 Voltage Vs current density curves for different KOH concentrations for the fuel cell system. ..... 78

Fig. 5.38 Power density Vs current density curves for different KOH concentrations for the fuel cell system. 79
Fig. 5.39 Voltage Vs current density curves for different operating temperatures for the fuel cell system. 80
Fig. 5.40 Power density Vs current density curves for different operating temperatures for the fuel cell system. 80
Fig. 5.41 Voltage Vs current density curves for different input ammonia pressures for the fuel cell system 82
Fig. 5.42 Power density Vs current density curves for different input ammonia pressures for the fuel cell system 82
Fig. 5.43 Variation of fuel cell energy efficiency with current density at varying KOH concentrations 83
Fig. 5.44 Variation of fuel cell exergy efficiencies with current density at Varying KOH concentrations 83
Fig. 5.45 Variation of fuel cell energy efficiencies with current density at varying operating temperatures. 84
Fig. 5.46 Variation of fuel cell exergy efficiencies with current density at varying operating temperatures. 84
Fig. 5.47 Polarization curves for the battery system at different concentrations of $NH_4Cl$ 85
Fig. 5.48 Polarization curves for the battery system at different concentrations of $NiSO_4$ 85
Fig. 5.49 Polarization curves for the battery system at different operating temperatures. 86
Fig. 5.50 A comparison of energy and exergy efficiencies of the developed direct ammonia fuel cell systems 87

# LIST OF TABLES

Table 1.1 Comparison of energy and volumetric density of ammonia and hydrogen ..... 4
Table 2.1 Peak power densities and open circuit voltages of various ammonia fed SOFC-O operated at varying temperatures and electrolyte thicknesses. ..... 12
Table 2.2 Peak power densities and open circuit voltages of various ammonia fed SOFC-H operated at varying temperatures and electrolyte thicknesses. ..... 15
Table 2.3 Peak power densities of ammonia borane fuel cells operated at varying temperatures, electrolyte and electrode materials. ..... 18
Table 2.4 Peak power densities and open circuit voltages of various ammonia fed alkaline fuel cells operated at varying temperatures and electrolyte and electrode materials. ..... 19
Table 3.1 Technical specifications of the anion exchange membrane ..... 22
Table 3.2 Specifications of the gas diffusion layer ..... 24
Table 3.3 Specifications of the FMA-1600A flow meter ..... 32
Table 3.4 Specifications of the OM-DAQPRO-5300 temperature measurement system ..... 33
Table 5.1 Theoretical modelling parameters for anion exchange membrane direct ammonia fuel cell ..... 51
Table 5.2 Results of electrochemical impedance spectroscopy ..... 72
Table 5.3 Advantages and disadvantages of the novel hybrid ammonia fuel cell and battery system ..... 86

## NOMENCLATURE

| | |
|---|---|
| $A$ | area ($m^2$) |
| C | concentration (M) |
| $ex$ | specific exergy (kJ/kg) |
| $E$ | potential (V) |
| $En$ | energy (kJ) |
| $\dot{E}n$ | energy rate (kW) |
| $Ex$ | exergy (kJ) |
| $\dot{E}x$ | exergy rate (kW) |
| F | Faraday constant (96500 C/mol) |
| G | Gibbs free energy (J) |
| $h$ | specific enthalpy (kJ/kg) |
| J | current density ($A/m^2$ or $mA/cm^2$) |
| $J_L$ | limiting current density ($A/m^2$) |
| $J_0$ | exchange current density ($A/m^2$) |
| k | thermal conductivity (W/mK) |
| L | inductance (H) |
| LHV | lower heating value (kJ) |
| $m$ | mass (kg) |
| $\dot{m}$ | mass flow rate (kg/s) |
| $\dot{M}_i''$ | molar diffusion rate flux (mol/s $m^2$) |
| $\dot{N}$ | molar flow rate (mol/s) |
| $P$ | pressure (Pa or kPa) |
| R | resistance (ohm) |
| $R$ | universal gas constant (8.314 kJ/kmol K) |
| s | specific entropy (kJ/kgK) |
| Sh | Sherwood number (-) |
| $\dot{S}$ | entropy rate (kW/K) |
| t | time (seconds) |
| $T$ | temperature ($^oC$) |
| V | voltage (mV or V) |
| $\dot{V}$ | volume flow rate ($m^3/s$) |
| $W$ | work (kJ) |
| $\dot{W}$ | work rate (W or kW) |
| $Z$ | impedance (Ω) |

***Greek letters***

| | |
|---|---|
| $\alpha$ | transfer coefficient |
| $\delta$ | Nernst diffusion layer thickness |
| Δ | change |
| $\eta$ | efficiency |
| $\rho$ | density ($kg/m^3$) |
| $\pi$ | Pi number |

| | |
|---|---|
| $\sigma$ | membrane conductivity (1/Ωcm) |
| $\phi$ | phase angle ($^{o}$) |
| $\omega$ | angular frequency (rad/s) |

***Subscripts***

| | |
|---|---|
| 0 | ambient condition |
| a | anode |
| *act* | activation |
| *B* | battery, bulk |
| c | cathode |
| C | capacitance |
| conc | concentration |
| eff | effective |
| en | energy |
| ex | exergy |
| $FC$ | fuel cell |
| gen | generation |
| imag | imaginary part |
| in | input |
| L | inductance |
| *ohm* | Ohmic |
| *out* | outlet |
| *ov* | overall |
| *r* | reversible |
| R | resistance |
| sc | short circuit |
| $S$ | specie |
| tn | thermonuetral |
| $tot$ | total |

***Acronyms***

| | |
|---|---|
| Au | Gold |
| BCG | Gadolinium-doped barium cerate |
| BCGE | Europium doped barium cerate |
| BCGO | $BaCe_{0.8}Gd_{0.2}O_{2.9}$ |
| BCGP | Gadolinium and Praseodymium-doped barium Cerate |
| BCNO | $BaCe_{0.9}Nd_{0.1}O_{3-\delta}$ |
| BSCF | $Ba_{0.5}\ Sr_{0.5}\ Co_{0.8}\ Fe_{0.2}O_{3-\delta}$ |
| BZCY | $BaZr_{0.1}Ce_{0.7}Y_{0.2}O_{3-\delta}$ |
| CDN/C | Chromium decorated nickel/carbon |
| CPPO | Chloroacetyl poly (2, 6-dimethyl-1, 4-phenylene oxide) |
| DABC | Direct ammonia borane fuel cell |
| LSCO | $La_{0.5}Sr_{0.5}CoO_{3-\delta}$ |
| LSM | $La_{0.67}Sr_{0.33}MnO_{3-\delta}$ |
| $MnO_2$ | Manganese di oxide |
| $NH_3$ | Ammonia |

| | |
|---|---|
| OCV | open circuit voltage |
| PVA | poly vinyl alcohol |
| Ru | Ruthenium |
| SDC | Samarium doped ceria |
| SSC | $Sm_{0.5}\ Sr_{0.5}\ CoO_{3-\delta}$ |
| TB | Triple phase boundary |
| YSZ | Yittria stabilized zirconia |

# CHAPTER 1 : INTRODUCTION

In this chapter, the significance of utilizing hydrogen as an energy carrier and the associated challenges are elucidated. The eminence of ammonia as a promising chemical means of storing hydrogen is also discussed. Further, the usage of ammonia in fuel cell technologies is described and the objectives of the present study are explained.

## 1.1 Significance of renewable energy resources

Energy forms an integral part of any economy. In the past decades, energy demands have been increasing incessantly across the globe. In addition, the primary demands for energy across the globe are projected to increase by 50% during the years 2016 and 2030 [1]. In the quest of meeting high energy needs and demands, the environment has been affected adversely. Utilization of fossil fuels has been the primary reason of environmental damage. The global breakdown of energy resources utilized for electricity generation is shown in Fig. 1.1. As can be depicted from the figure, the mainstream energy resources utilized globally comprised of fossil fuels and nuclear energy (76.3%) in 2015. Further, hydropower constituted 16.6% of globally utilized energy resources. However, renewable energy resources including wind, biomass, solar and geothermal energy collectively comprised of 7.3%. Colossal amounts of emissions are continuously released to the atmosphere due to the usage of fossil fuels for energy production. Massive amounts of environmental contaminants and greenhouse gases are emitted to the atmosphere [2]. In order to overcome the problems associated with the usage of fossil fuels, the resort lies in the usage of renewable resources of energy [3–9]. Renewable energy resources are environmentally benign and clean. Furthermore, conventional fossil fuel based energy resources are associated with the threat of depletion. However, renewable energy technologies provide a viable solution to attain a sustainable economy, environment and society.

## 1.2 Hydrogen as an energy carrier

Hydrogen is considered a promising energy carrier owing to its environmentally benign nature when utilized as an energy resource [11–21]. Combustion of hydrogen results in water vapor as a product. Furthermore, hydrogen provides a solution to energy storage problems. Energy can be stored in the form of hydrogen over long periods of time.

Moreover, in the case of intermitted sources of energy such as solar and wind energy, hydrogen can be produced during periods of excess energy and can be stored for later use, during periods of low energy generation. In addition to this, hydrogen is also utilized in the transportation sector. Gasoline or diesel powered vehicles cause significant harm to the environment, hence hydrogen provides a clean solution of energy. It has a high energy density when considered on a mass basis. Hydrogen can be utilized for energy production via combustion or through fuel cell technologies. The production capacity of hydrogen in the past decade from U.S. refineries is depicted in Fig. 1.2.

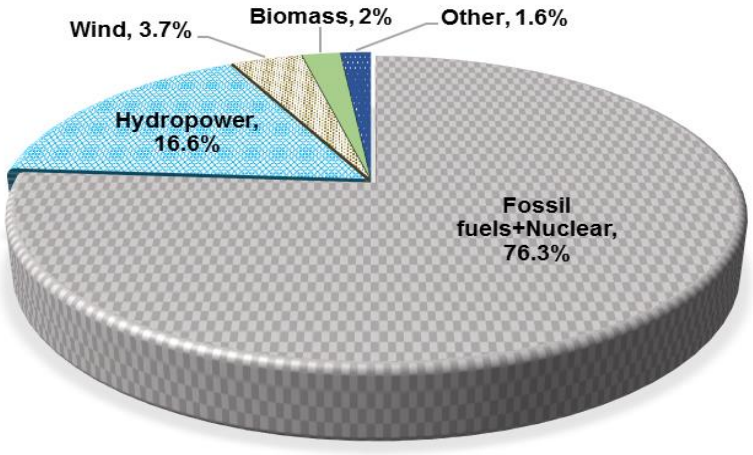


Fig. 1.1 Breakdown of global energy resources utilized for electricity generation as of 2015 (data from [10]).

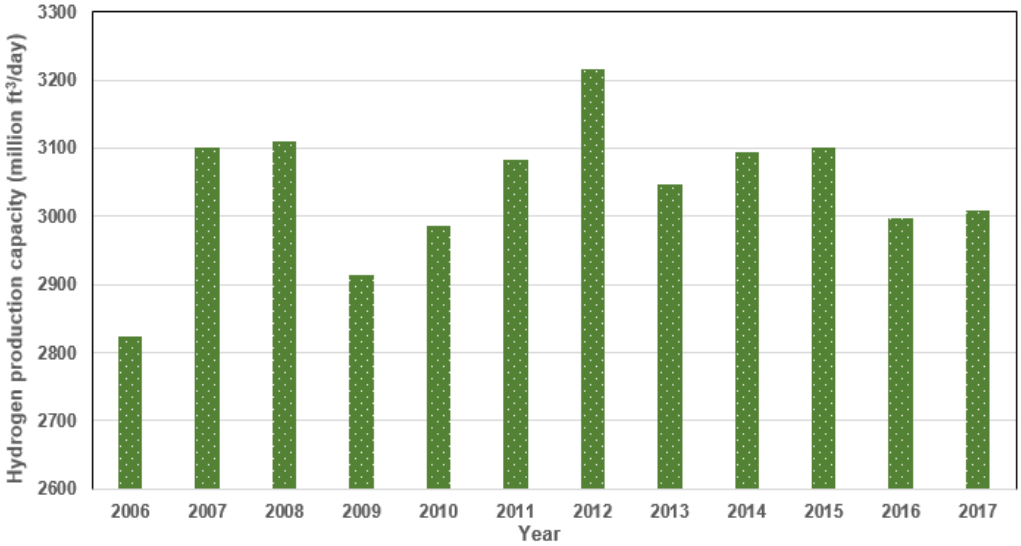


Fig. 1.2 Capacity of hydrogen production from U.S. refineries (data from [22]).

### 1.3 Challenges associated with hydrogen

Hydrogen is a promising clean fuel for energy production, however, it possesses several challenges that need to be addressed. Storage of hydrogen fuel is one of the major challenges. Hydrogen has a low volumetric density. Thus, this poses a drawback in storage as well as transportation. Comparatively high storage space is required. Additional costs are incurred to accommodate appropriate amounts of hydrogen storage. In the transportation sector, this poses a challenge in terms of vehicle mile ranges. In order to achieve high mile ranges, sufficient and efficient on-board hydrogen storage systems need to be designed and developed. Furthermore, durability and robustness of hydrogen storage systems and materials is currently inadequate. Components with longer lifetimes are required [23]. In addition, hydrogen is an odorless flammable gas. It is considered dangerous while storage or transportation. A hydrogen leakage can be undetected without the usage of sensors, posing a hazard of explosion as it has a wide range of flammability in air. The flammability limits of hydrogen lie between 4-74%. This is a comparatively high range as compared to gasoline (1.4-7.6%) and natural gas (5.3-15%). Moreover, the ignition energy required for hydrogen can be as low as 0.02 mJ at high concentrations. [24]

### 1.4 Energy from Ammonia

In order to overcome these drawbacks, alternative hydrogen carriers are being investigated. Several hydrogen carriers including ammonia, hydrocarbons and alcohols have been considered. Ammonia is a promising candidate owing to its properties [25–47]. It has a high energy density of 4 kWh/kg and is easy to liquefy as it has a boiling point of -33.4$^{o}$C at standard atmospheric pressure. Furthermore, it has comparatively high hydrogen content of 17.7 wt% and has a constricted flammable range of approximately 16-25 volume % in air [6, 7]. Table 1.1 provides a comparison of volumetric and energy density of hydrogen and ammonia. Hydrogen gas has a low energy density of 0.9 MJ/L at a temperature of 25$^{o}$C and a high pressure of 10 MPa. In order to increase the volumetric density, hydrogen can liquefied for storage and transportation. However, as shown in Table 1.1, liquefying hydrogen requires a very low temperature of -253$^{o}$C at atmospheric pressure. Ammonia liquid has significantly higher volumetric density as compared to hydrogen liquid or gas. Furthermore, ammonia also has a higher energy density than liquid hydrogen when stored as liquid at 25$^{o}$C and a pressure of 10 atmospheres. Ammonia is free of carbon and is cost

effective hence, it provides an alternative fuel source to achieve lower environmentally harmful emissions in the process of energy generation [26].

Table 1.1 Comparison of energy and volumetric density of ammonia and hydrogen

| | Temperature (°C) | Pressure (MPa) | Weight % $H_2$ | Energy density (MJ/L) | Density (g/L) |
|---|---|---|---|---|---|
| Hydrogen gas | 25 | 10 | 100 | 0.9 | 7.7 |
| Hydrogen liquid | -253 | 0.1 | 100 | 8.6 | 71.3 |
| Ammonia liquid | 25 | 1 | 17.7 | 12.9 | 603 |

Moreover, ammonia is produced by various countries in large quantities. Fig. 1.3 depicts the production of ammonia and the increase in production quantity with time. Ammonia is a primary industrial chemical that is produced in large capacities globally.

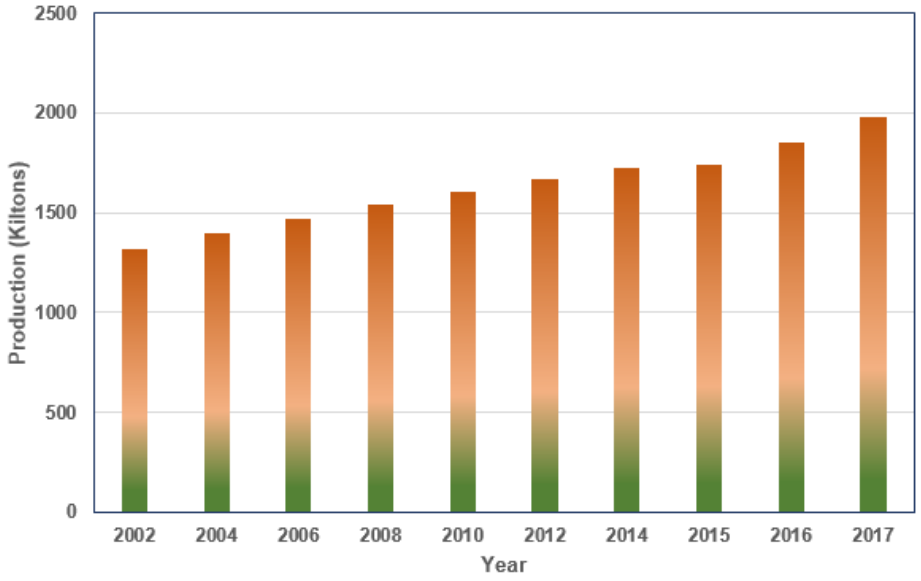


Fig. 1.3 Rise in global ammonia production (data from [50]).

Various possible methods exist for utilizing ammonia for energy production as depicted in Fig. 1.4. Technologies employ either combustion of ammonia or dissociation and electrochemical reaction through fuel cells. Technologies employing combustion processes convert the stored chemical energy in ammonia molecules to thermal energy. This thermal energy produced is utilized for power generation. However, fuel cell technologies deploy electrochemical means of power generation.

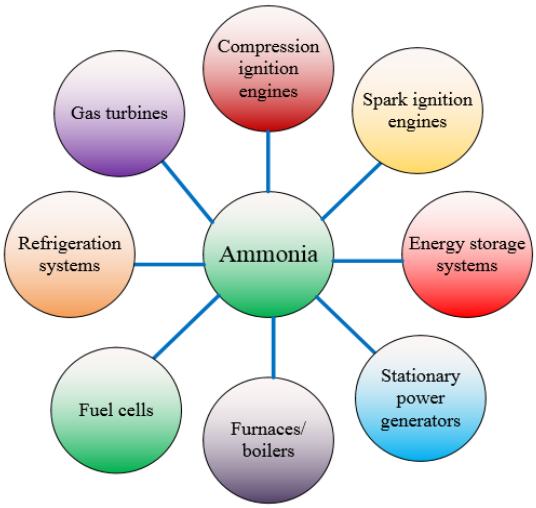


Fig. 1.4 Various possible routes for energy from ammonia

Ammonia is reacted electrochemically in a combination of anodic oxidation and cathodic reduction reactions to generate power. Depending on the type of fuel cell, ammonia can be cracked into hydrogen before the commencement of the electrochemical reaction or directly reacted electrochemically.

### 1.5 Methods utilized for ammonia production

Various methods are deployed for ammonia production. Majority of global ammonia production methods utilize methane steam reforming. In addition, other sources including coal, naphtha and oil are also used. The ammonia production method utilized is dependent on available resources. For instance, the source utilized for producing ammonia in China is coal. Primary processes utilized for producing ammonia include the Haber-Bosch process as well as the Solid-state synthesis process.

The Haber-Bosch process involves reaction of nitrogen and hydrogen at temperatures between 450-600$^{o}$C and pressures between 100 to 250 bar in the presence of catalyst [51]. The required hydrogen can be obtained from various routes. The steam methane reforming process is widely used to obtain hydrogen. Natural gas and steam react to produce hydrogen and carbon di oxide. Furthermore, an air separation unit is required to obtain pure nitrogen that can be fed in the Haber-Bosch process along with hydrogen. In addition to steam methane reforming, hydrogen can also be obtained from water electrolysis. The Haber-Bosch process at optimal conditions of pressures ranging between

100 to 250 bar and temperatures varying between 450$^{o}$C to 600$^{o}$C provides conversion rates between 25% to 35% [52]. The Haber-Bosch process plant includes a catalyst bed and heater fed with compressed nitrogen and hydrogen. The reactants fed into the reactor do not react completely. The produced ammonia and unreacted hydrogen and nitrogen are passed through a condenser where ammonia gas is liquefied, separated and collected. The nitrogen and hydrogen gases are pressurized and sent back to the heated catalyst bed. This recycling of unreacted reactants is continued throughout the process along with additional feed of reactants. The environmental burden caused by ammonia production in the Haber-Bosch process depends on the sources utilized to obtain hydrogen and nitrogen. If fossil fuel based energy resources are utilized to produce ammonia, significant environmental impacts are created. However, if clean and environmentally benign resources of energy are utilized, the environmental footprint can be reduced. Furthermore, the reactant gases of nitrogen and hydrogen have low conversion rates due to thermodynamic limitations. Further enhancements in the catalysts used in the Haber-Bosch process are necessary to achieve high yields of production. In addition, achieving and maintaining high temperatures and pressures require high energy inputs leading to high costs. The average energy requirement in North America for ammonia production is 41.6 MJ/tonne $NH_3$ and the GHG emissions are 2.34 tonne $CO_2$ eq/tonne of $NH_3$ [53].

The solid-state synthesis method of ammonia production involves nitrogen and water vapor as reactants. Similar pressure levels are utilized as in the case of the Haber-Bosch process. Solid-state synthesis process utilizes a proton conducting membrane electrolyte. The operating temperature of the membrane is around 550$^{o}$C. This method does not require an external hydrogen production system. High temperature steam is fed into the reactor, where it dissociates into oxygen and protons. With the aid of an applied voltage, the protons travel to the nitrogen side through the proton conducting membrane. Nitrogen molecules and protons ($H^+$ ions) react to from ammonia molecules. The requirement of energy in the case of solid-state synthesis is comparatively lower than the Haber-Bosch process. Hence, a lower cost of ammonia production is expected. In addition to this, solid-state synthesis excludes utilization of fossil fuels for ammonia production. Thus, is considered comparatively more environmentally benign. The primary difference between the two techniques lies in the utilization of hydrogen gas or steam as a source of hydrogen

atoms. Solid-state synthesis utilizes steam, however, hydrogen gas is required for the Haber-Bosch process.

### 1.6 Direct ammonia fuel cells

Generation of electricity through fuel cells is considered as a clean source of energy production. Currently, hydrogen is the prominent fuel for fuel cell technology. However, in order to overcome the drawbacks of hydrogen, ammonia can be used as an alternative fuel. Incorporating ammonia as a fuel for fuel cells has been considered in various studies. In the utilization of ammonia as a fuel for fuel cells, either it can be decomposed into nitrogen and hydrogen externally or it can be directly fed into the cell. Direct ammonia fuel cells allow feeding of ammonia as a fuel directly without requiring an external decomposition unit. Hence, provide more applicability for various uses. Ammonia was initially investigated as a source of electricity generation from fuel cells as well as a source to produce nitrogen oxide as a useful chemical [13,14]. Several studies have followed which investigated ammonia as a fuel source for different types of fuel cells. Different types of ammonia fuel cell technologies are presented in Fig. 1.5. Direct ammonia fuel cells can be divided into solid oxide fuel cell and alkaline electrolyte based fuel cell technologies. Solid oxide fuel cells can be further divided into proton conducting or oxygen anion conducting electrolyte based fuel cells. The second type of direct ammonia fuel cells is the alkaline electrolyte based fuel cells. These type of fuel cells employ anion exchange membrane electrolytes or molten or aqueous electrolytes for the electrochemical energy conversion process.

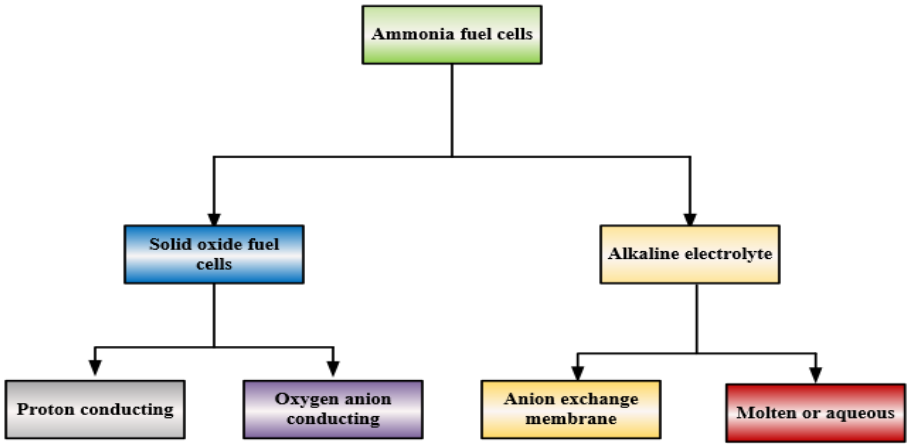


Fig. 1.5 Different types of direct ammonia fuel cells

## 1.7 Motivation

Energy production and consumption, have been in the past decades, increasing incessantly across the globe. They are projected to continuously increase in the upcoming years. While trying to meet high-energy needs and demands, the environment has been affected adversely. Fossil fuels have caused considerable environmental damage throughout the world. Hydrogen is an environmentally benign source of energy and is a promising energy carrier. As utilization of hydrogen increases, more attention and efforts are being directed towards better storage media for hydrogen owing to its low density. Ammonia is considered as a promising chemical storage medium for hydrogen owing to its high energy density. Further, ammonia is one of the most highly consumed chemical in the world owing to its extensive use in fertilizers. Electrochemical oxidation properties of ammonia provide an opportunity for its utilization in fuel cell applications. In order to investigate the possibilities of utilizing ammonia as an effective chemical storage medium for hydrogen, it is essential to investigate its use in fuel cells applications. Hence, this thesis is focused on developing and investigating direct ammonia fuel cells.

## 1.8 Objectives

Although, studies have been conducted on ammonia fuel cells. Most studies were focused on utilizing solid oxide fuel cells. However, these type of fuel cells require high working temperatures and expensive electrolytes. These requirements deter the usage of ammonia in fuel cells. Electrochemical oxidation properties of ammonia in alkaline mediums allow its usage in alkaline fuel cells at ambient temperatures. Hence, this study is focused on developing and testing anion exchange membrane direct ammonia fuel cells.

The specific objectives of this study are listed below:

- To build an anion exchange membrane direct ammonia fuel cell that operates with gaseous ammonia as anode input and humidified air as cathode input.
- To assess the performance of the single-cell direct ammonia fuel cell as well as a five-cell direct ammonia fuel cell stack at ambient conditions with gaseous ammonia and aqueous ammonia as fuels.

- To analyse the effect of varying humidifier temperatures and aqueous ammonia solution temperatures on the performance of single-cell direct ammonia fuel cell as well as the five-cell fuel cell stack.
- To develop and investigate a molten salt alkaline electrolyte based direct ammonia fuel cell and evaluate its performance at varying electrolyte temperatures.
- To develop and analyse a novel hybrid regenerative-electrode ammonia fuel cell and battery system to better utilize the electrochemical energy of ammonia.
- To perform energy, exergy and electrochemical analyses of the developed systems to assess the system performance in terms of energy and exergy efficiencies.
- To conduct parametric studies on the developed direct ammonia fuel cell systems to analyse the effect of varying operating parameters on the system performances.

# CHAPTER 2 : LITERATURE REVIEW

A review of the studies conducted on direct ammonia fuel cells is included in this chapter. Different types of fuel cells investigated and their comparative performance is presented. The effect of electrolyte and electrode materials, electrolyte thicknesses and operating temperatures on the performance of direct ammonia fuel cells is elaborated.

## 2.1 Oxygen anion conducting electrolyte based solid oxide fuel cells (SOFC-O)

Solid oxide fuel cells based on oxygen anion conducting electrolytes entail the working principle of the transport of $O^{2-}$ ions through the electrolyte. Pure oxygen gas or air is fed at the cathode side of fuel cell. At the interface between the cathode and electrolyte, reduction of oxygen gas to oxygen ions occurs. These ions pass through the electrolyte and an electrochemical reaction takes place with hydrogen at the interface of the anode and electrolyte to produce water vapor. The hydrogen is produced by thermal decomposition of ammonia fuel. The ammonia fuel is fed into the fuel cell at the anode side, where it undergoes a thermal decomposition under the presence of a catalyst.

$$NH_3 \leftrightarrow \frac{3}{2}H_2 + \frac{1}{2}N_2 \tag{2.1}$$

The hydrogen gas produced as a result of this decomposition diffuses to the interface between the anode and electrolyte where it reacts electrochemically with oxygen ions to form water vapor. The produced water vapor, nitrogen gas, unreacted ammonia fuel and hydrogen gas leave the fuel cell. The production of nitrogen during thermal decomposition of ammonia results in a dilution of hydrogen concentration, which reduces the reversible cell potential of the fuel cell. Fig. 2.1 depicts the working principle of SOFC-O. The cathodic and anodic reactions are given below:

Anodic reactions:

$$H_2 + O^{2-} \rightarrow H_2O + 2e \tag{2.2}$$

Cathodic reactions:

$$\frac{1}{2}O_2 + 2e \rightarrow O^{2-} \tag{2.3}$$

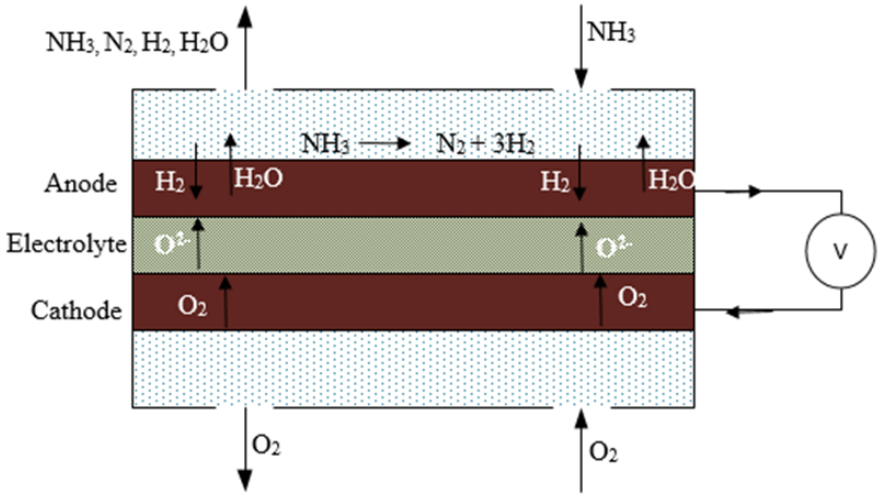


Fig. 2.1 Working principle of SOFC-O

Direct ammonia fuel cells with oxygen anion conducting Samarium doped ceria (SDC) and Yittria stabilized zirconia (YSZ) electrolytes have shown promising performance. Ma et al. [56] investigated a 50µm SDC electrolyte based SOFC-O with nickel anode and $Sm_{0.5}Sr_{0.5}CoO_{(3-\delta)}$ (SSC) cathode, a maximum power density of 168.1 mW/cm$^2$ was obtained with ammonia as the fuel at 600$^o$C. However, a peak power density of 191.8 mW/cm$^2$ was observed with hydrogen as a fuel at the same temperature. In addition, at higher temperatures, greater power densities were obtained. Furthermore, Meng et al. [57] investigated a 10 µm thick SDC electrolyte with nickel based anode and $Ba_{0.5}Sr_{0.5}Co_{0.8}Fe_{0.2}O_{3-\delta}$ (BSCF) cathode and observed a peak power density of 1190 mW/cm$^2$ at a temperature of 650$^o$C. Whereas, when fed with hydrogen as the fuel, a higher peak power density of 1872 mW/cm$^2$ was observed at the same temperature. Liu et al. [58] tested a 24µm thick SDC electrolyte with nickel oxide based anode and SSC cathode, a peak power density of 467 mW/cm$^2$ was observed at a temperature of 650$^o$C with ammonia as the fuel. Yittria stabilized zirconia (YSZ) is also used as an electrolyte in ammonia fed solid oxide fuel cells. However, lower performance is observed as compared to SDC electrolytes. Limin et al. [59] investigated an ammonia fed fuel cell with 15 µm thick YSZ electrolyte, nickel anode and LSM cathode. A peak power density of 202 mW/cm$^2$ was observed at 800$^o$C. In addition, Ma et al. [60] fabricated and tested an ammonia fed fuel cell comprised of nickel based anode and YSZ-LSM cathode with a 30µm YSZ electrolyte provides a peak power density of 299 mW/cm$^2$ and 526 mW/cm$^2$ at 750$^o$C and 850$^o$C

respectively. Moreover, Fournier et al. [61] developed and tested a 400µm thick YSZ electrolyte based ammonia fed solid oxide fuel cell with nickel oxide based anode and silver cathode, a peak power density of 60 mW/cm$^2$ was obtained at a temperature of 800$^o$C. In addition, Fuerte et al. [44] tested a 200µm thick YSZ electrolyte with nickel based anode and LSM cathode fuel cell at a high temperature of 900$^o$C, the peak power density obtained was 88 mW/cm$^2$. However, at a lower temperature of 700$^o$C, the peak power density reduced to 38 mW/cm$^2$. Wojcik et al. [62] investigated a platinum-based anode and silver-based cathode and YSZ electrolyte, the peak power density obtained at a high temperature of 1000$^o$C was 125 mW/cm$^2$. When the operating temperature was reduced to 800$^o$C, the peak power density decreased to 50 mW/cm$^2$. Table 2.1 lists the peak power density and open circuit voltages of various ammonia fed SOFC-O operated at varying temperatures and electrolyte thicknesses.

Table 2.1 Peak power densities and open circuit voltages of various ammonia fed SOFC-O operated at varying temperatures and electrolyte thicknesses.

| **Electrodes** | **Electrolyte** | **Electrolyte thickness (µm)** | **Operating Temperatures ($^o$C)** | **OCV (V)** | **Peak power density (mW/cm$^2$)** | **Reference** |
|---|---|---|---|---|---|---|
| Ni-SDC (anode)<br>SSC–SDC (cathode) | SDC | 50 | 500<br>600<br>700 | 0.9<br>0.88<br>0.83 | 65<br>168<br>250 | [56] |
| NiO (anode)<br>BSCF (cathode) | SDC | 10 | 550<br>600<br>650 | 0.795<br>0.771<br>0.768 | 167<br>434<br>1190 | [57] |
| Pt-YSZ (anode)<br>Ag (cathode) | YSZ | 200 | 800<br>900<br>1000 | 0.9 | 50<br>90<br>125 | [62] |
| NiO-YSZ (anode)<br>Ag (cathode) | YSZ | 400 | 800 | 1.22 | 60 | [61] |
| Ni-YSZ(anode)<br>YSZ-LSM(cathode) | YSZ | 30 | 750<br>850 | 1.07<br>1.03 | 299<br>526 | [60] |
| Ni-YSZ(anode)<br>YSZ-LSM(cathode) | YSZ | 15 | 800 | 1.06 | 202 | [59] |
| NiO-SDC (anode)<br>SSC-SDC (cathode) | SDC | 24 | 650 | 0.79 | 467 | [58] |
| Ni-YSZ (anode)<br>LSM (cathode) | YSZ | 200 | 800<br>900 | 1.02<br>0.99 | 65<br>88 | [44] |

## 2.2 Proton conducting electrolyte based solid oxide fuel cells (SOFC-H)

In ammonia fed proton conducting electrolyte based solid oxide fuel cells, the ammonia fuel decomposes to form nitrogen and hydrogen. The hydrogen gas produced due to the decomposition of ammonia oxidizes to protons ($H^+$) in the presence of a catalyst. The $H^+$ ions are transferred through a proton-conducting electrolyte to reach the cathode-solid electrolyte interface, where it reacts with oxygen to form water vapor. The produced water vapor and unreacted oxygen leave the fuel cell from the cathode side exit port of the fuel cell. At the anode side exit port of the fuel cell, unreacted ammonia, nitrogen gas and unreacted hydrogen leave the fuel cell. Ammonia fed SOFC-H avoid the formation of nitrogen oxides as in the case of SOFC-O. The operation principle of a SOFC-H is shown in Figure 2.2. The anode and cathode electrochemical reactions are given below:

Anodic reactions:

$$H_2 \rightarrow 2H^+ + 2e \tag{2.4}$$

Cathodic reactions:

$$\frac{1}{2}O_2 + 2H^+ + 2e \rightarrow H_2O \tag{2.5}$$

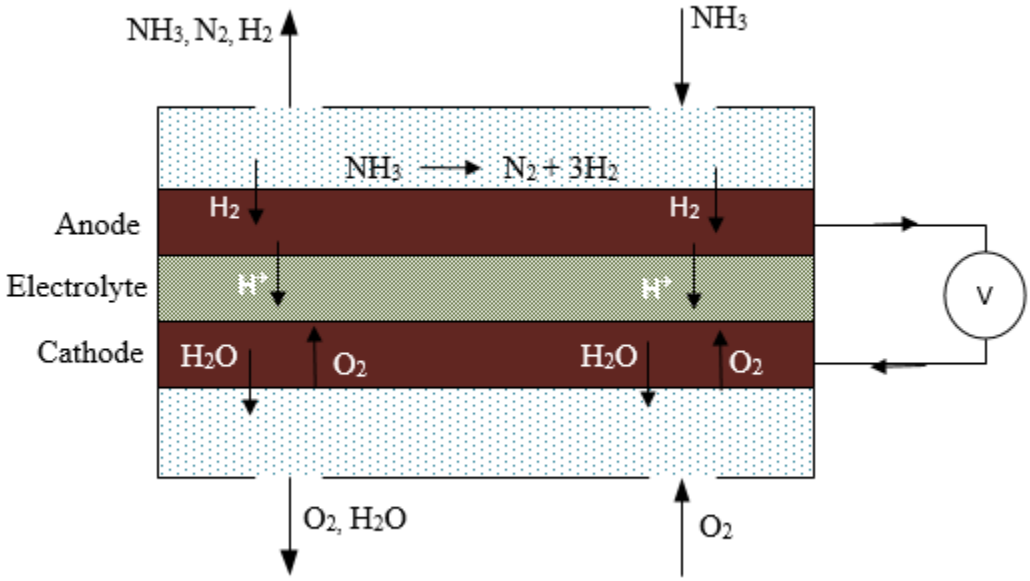


Fig. 2.2 Working principle of SOFC-H.

Ammonia fed proton conducting electrolyte based solid oxide fuel cells have lower power densities as compared to ammonia fed SOFC-O. Mainly, BCG based electrolytes have been utilized in SOFC-H with platinum or nickel based anodes. Platinum or nickel act as catalysts in the dissociation of ammonia. Pelletier et al. [63] investigated a 1300 μm thick BCGP solid electrolyte with ammonia as the fuel, the peak power density obtained with platinum electrodes at 700$^{o}$C was 35 mW/cm$^{2}$. In addition, Maffei et al. [64] tested a BCG electrolyte with the same electrode materials, electrolyte thickness and operating temperature fed with ammonia as the fuel, a peak power density of 25 mW/cm$^{2}$ was obtained. Moreover, Maffei et al. [65] investigated a BCGP electrolyte operating at a temperature of 600$^{o}$C, peak power densities of 28 and 23 mW/cm$^{2}$ were observed for Ni-BCE and platinum anodes respectively with ammonia as the fuel. Furthermore, Ma et al. [66] developed and tested a BCGE electrolyte based solid oxide fuel cell with ammonia as the fuel and observed a peak power density of 32 mW/cm$^{2}$. The electrolyte was 1000 μm thick and platinum electrodes were utilized, the operating temperature was 700$^{o}$C. In addition to this, a 50 μm thick BCGO electrolyte was investigated. The anode comprised of Ni-BCGO, and a LCSO-BCGO cathode was utilized. Temperatures were varied from 600 to 750$^{o}$C to test the performance of the fuel cell. The peak power densities were found to increase with increasing temperature. At 600$^{o}$C, a peak power density of 96 mW/cm$^{2}$ was obtained, whereas, at a temperature of 750$^{o}$C, the peak power density recorded was 384 mW/cm$^{2}$. Zhang and Yang [67] investigated a 30 μm BCGO electrolyte with Ni-CGO anode and BSCFO-CGO cathode and peak power densities of 147 and 200 mW/cm$^{2}$ were recorded at temperatures of 600 and 650$^{o}$C respectively with ammonia as the fuel. McFarlan et al. [68] tested a 1300 μm thick BCG electrolyte with platinum electrodes, a peak power density of 25 mW/cm$^{2}$ was obtained at a temperature of 700$^{o}$C. In addition, Lin et al. [69] fabricated and investigated a BZCY electrolyte based proton conducting electrolyte was also tested in an ammonia fed solid oxide fuel cell. A Ni-BZCY anode and BSCG cathode was utilized. The peak power densities were obtained in the range 25-390 mW/cm$^{2}$ with ammonia as the fuel for temperatures varied from 450 to 750$^{o}$C. Xie et al. [70] developed and tested a 20 μm thick proton conducting BCNO electrolyte based solid oxide fuel cell with a LCSO cathode and Nickel oxide based anode had a peak power density of 315 mW/cm$^{2}$ at a temperature of 700$^{o}$C. Furthermore, National Resources

Canada [71] developed a proton conducting electrolyte based direct ammonia fuel cell. A BCGP electrolyte was utilized with platinum electrodes. The peak power density was reported to be 23 mW/cm$^2$ with platinum electrodes and an operating temperature of 600$^o$C. However, it was found that NiO-BCE anode provides higher fuel cell performance with a peak power density of 27 mW/cm$^2$ .Table 2.2 lists the peak power density and open circuit voltages of various ammonia fed SOFC-H operated at varying temperatures and electrolyte thicknesses.

Table 2.2 Peak power densities and open circuit voltages of various ammonia fed SOFC-H operated at varying temperatures and electrolyte thicknesses.

| **Electrodes** | **Electrolyte** | **Electrolyte thickness (um)** | **Operating Temperature ($^o$C)** | **OCV (V)** | **Peak power density (mW/cm$^2$)** | **Reference** |
|---|---|---|---|---|---|---|
| Pt (Anode and cathode) | BCGP | 1300 | 700 | 0.85 | 35 | [63] |
| Pt (Anode and cathode) | BCG | 1300 | 700 | 0.85 | 25 | [64] |
| Pt (Anode and cathode) | BCG | 1000 | 700 | 0.66 | 32 | [72] |
| Ni-BCE (Anode)<br>Pt (Cathode) | BCGP | 1000 | 500<br>550<br>600 | <br><br>0.92 | 15<br>18<br>28 | [17] |
| Pt (Anode and cathode) | BCGP | 1000 | 600 | | 23 | [65] |
| Ni-BCGO (anode)<br>LSCO (cathode) | BCGO | 50 | 600<br>650<br>700<br>750 | 1.102<br>1.095<br>0.995<br>0.985 | 96<br>184<br>355<br>384 | [18] |
| Ni-CGO (anode)<br>BSCFO-CGO (cathode) | BCGO | 30 | 600<br>650 | 1.12<br>1.10 | 147<br>200 | [19] |
| Ni-BZCY (anode)<br>BSCF (cathode) | BZCY | 35 | 450<br>500<br>550<br>600<br>650<br>700<br>750 | 0.95 | 25<br>65<br>130<br>190<br>275<br>325<br>390 | [69] |
| NiO-BCNO (anode)<br>LSCO (cathode) | BCNO | 20 | 700 | 0.95 | 315 | [70] |
| Pt (anode and cathode) | BCG | 1300 | 700 | 0.85 | 25 | [20] |

## 2.4 Ammonia borane fuel cells

Direct ammonia borane fuel cell was first investigated by Zhang et al. [73]. Ammonia borane ($NH_3BH_3$) solution is fed as the fuel into the fuel cell at the anode side, where it reacts with hydroxyl anions. The hydroxyl anions participating in the reaction are either formed by the reduction of oxygen at the cathode side or are present in the medium. The electrolyte comprises of a cation or anion exchange membrane. The cathodic reaction of reduction of oxygen to form hydroxyl ions is similar to other types of fuel cells:

$$\frac{3}{2}O_2 + 3H_2O + 6e \rightarrow 6OH^- \tag{2.6}$$

The produced hydroxyl anions diffuse through the membrane electrolyte to reach the anode side of the fuel cell, where the oxidation of $NH_3BH_3$ occurs. The anodic reaction for a direct ammonia borane fuel cell is expressed as

$$NH_3BH_3 + 6OH^- \rightarrow BO^{2-} + NH_4^+ + 4H_2O + 6e \tag{2.7}$$

The overall reaction for an ammonia borane fuel cell can be expressed as

$$NH_3BH_3 + \frac{3}{2}O_2 \rightarrow BO^{2-} + NH_4^+ + H_2O \tag{2.8}$$

A sodium hydroxide electrolyte based ammonia borane fuel cell operating at room temperature was observed to have a peak power density of 14 mW/cm$^2$. The working electrode comprised of platinum and gold [73]. Furthermore, an ammonia borane fuel cell with an anion exchange membrane and platinum electrodes provided peak power densities of 40-110 mW/cm$^2$ when the operating temperatures were varied from 25-45$^o$C [74]. Table 2.3 lists the peak power densities of ammonia borane fuel cells operated at varying temperatures and electrolyte and electrode materials.

## 2.5 Alkaline electrolyte-based direct ammonia fuel cells

Alkaline fuel cells were investigated and developed to be utilized in practical applications in the early stages of fuel cell research and development. They were employed in space applications, vehicles, energy storage and decentralized energy supply [75]. Alkaline membrane and molten or aqueous electrolyte ammonia fuel cells employ the exchange of anions. Air is fed into the fuel cell at the cathode side. The oxygen molecules in the air react with water molecules to form hydroxide ions. The hydroxide anions travel through

the electrolyte, which can be an anion exchange membrane or an alkaline electrolyte such as aqueous or molten potassium or sodium hydroxide. In ammonia based alkaline fuel cells, ammonia is fed as a fuel into the fuel cell at the anode side. It combines with the hydroxide anions to form nitrogen and water. The reaction of oxygen with water molecules at the cathode side consumes electrons, whereas, the reaction of ammonia with hydroxide ions at the anode side produces electrons. Hence, producing an electric current through an external electrical path. The cathode, anode and overall reactions for alkaline ammonia fuel cells are given below

Anodic reaction:

$$2NH_3 + 6OH^- \rightarrow N_2 + 6H_2O + 6e \quad (2.9)$$

Cathodic reaction:

$$\frac{3}{2}O_2 + 3H_2O + 6e \rightarrow 6OH^- \quad (2.10)$$

Overall reaction:

$$2NH_3 + \frac{3}{2}O_2 \rightarrow N_2 + 3H_2O \quad (2.11)$$

In alkaline fuel cells, the presence of carbon dioxide gas degrades the performance of the cell. The carbon dioxide gas reacts with hydroxide anions present to form carbonate ions. This reaction reduces the number of hydroxide anions available to react with ammonia. In addition, the ionic conductivity of the alkaline electrolyte is reduced due to the formation of carbonate ions. Precipitates of carbonate compounds are found in alkaline molten or aqueous electrolyte, however, in alkaline membrane electrolytes, the formation of precipitates is avoided.

$$CO_2 + 2OH^- \rightarrow CO_3^{2-} + H_2O \quad (2.12)$$

A molten potassium and sodium hydroxide mixture electrolyte based ammonia fed fuel cell at operating temperatures between 200-450$^o$C was observed to have a peak power density of 16 mW/ cm$^2$ at a temperature of 200$^o$C. However, as the temperature was increased to 450$^o$C, a considerable increase in peak power density was observed. At 450$^o$C, it increased to 40 mW/cm$^2$ [76]. In addition, another study on ammonia fed alkaline fuel

cell with molten potassium and sodium hydroxide electrolyte was conducted [77]. Temperatures of 200-220$^{o}$C were chosen for the study. The peak power density obtained at 200$^{o}$C was 10.5 mW/cm$^2$. However, at a higher temperature of 220$^{o}$C, it increased to 16 mW/cm$^2$. Electrodes used comprised of platinum material. Furthermore, a CPPO-PVA based alkaline membrane electrolyte fuel cell with CDN/C anode and $MnO_2$/C cathode provided a peak power density of 16 mW/cm$^2$ at room temperature operation [78]. Furthermore, an anion exchange membrane fuel cell was developed and tested with ammonium hydroxide and ammonium carbonate as fuels [79]. Open circuit voltages of 0.36 V and 0.32 V were obtained for ammonium hydroxide and ammonium carbonate respectively. In addition, peak power densities of 0.22 mW/cm$^2$ and 0.11 mW/cm$^2$ were obtained for ammonium hydroxide and carbonate respectively. Moreover, an anion exchange membrane direct ammonia fuel cell was investigated with different types of electro catalysts. The open circuit voltage was observed to be 0.42 V at an operating temperature of 50$^{o}$C. The fuel cell performance was observed to be higher for the Pt/C electro catalyst as compared to the Pt-Ru/C catalyst. An anion exchange membrane was utilized as the electrolyte. The thickness of the membrane was specified to be 28 µm with an $OH^-$ conductivity of 42 mS/cm. In addition, a direct ammonia fuel cell was investigated with a Nafion membrane and different types of electrocatalysts. The PtAu/C electrocatalyst with atomic ratios of 70:30 ratio of Pt:Au was found to provide the highest fuel cell performance.

Table 2.3 Peak power densities of ammonia borane fuel cells operated at varying temperatures, electrolyte and electrode materials.

| **Electrodes** | **Electrolyte** | **Operating Temperature ($^{o}$C)** | **Peak power density (mW/cm$^2$)** | **Reference** |
|---|---|---|---|---|
| Au/Pt (working electrode) | NaOH | 25 | 14 | [27] |
| Pt | Anion exchange membrane | 25<br>35<br>45 | 40<br>70<br>110 | [28] |
| - | KOH | 45 | 315 (10 cell stack) | [38] |

The open circuit voltage was obtained as 0.58 V with this catalyst composition. Further, the peak power density was observed to be 2.3 $mW/cm^2mg_{Pt}$. In addition, the Au/C electrocatalyst was found to have an open circuit voltage of 0.289 V and a peak power density of 0.52 $mW/cm^2mg_{Pt.}$ In addition, other intermediate atomic ratios of Pt and Au were utilized to test the fuel cell performance. Table 2.4 lists the open circuit voltages and peak power densities of ammonia fed alkaline fuel cells at various operating temperatures.

Table 2.4 Peak power densities and open circuit voltages of various ammonia fed alkaline fuel cells operated at varying temperatures and electrolyte and electrode materials.

| **Electrodes** | **Electrolyte** | **Operating Temperature (°C)** | **OCV (V)** | **Peak power density ($mW/cm^2$)** | **Reference** |
|---|---|---|---|---|---|
| Nickel (anode and cathode) | Molten KOH+NaOH | 200<br>250<br>300<br>350<br>400<br>450 | 0.82<br>0.819<br>0.817<br>0.816<br>0.813<br>0.811 | 16<br>18<br>21<br>25<br>31<br>40 | [76] |
| Pt (anode and cathode) | Molten KOH+NaOH | 200<br>210<br>220 | 0.76<br>0.74<br>0.73 | 10.5<br>12<br>16 | [77] |
| CDN/C (anode)<br>$MnO_2$/C (cathode) | CPPO-PVA membrane | 25 | 0.85 | 16 | [78] |
| Pt/C (cathode)<br>Pt-Ru/C, Pt/C and Ru/C (anode) | Anion exchange membrane | 50°C | 0.42 | - | [80] |
| Pt-Au/C | Nafion Membrane | 40°C | 0.58 | 2.6 | [81] |

## 2.6 Gaps in the literature

Previous studies on direct ammonia fuel cells were primarily focused on high-temperature solid oxide fuel cell technologies. Proton conducting as well as oxygen anion conducting solid oxide electrolytes were utilized at high operating temperatures. Very few studies were found to focus on low temperature direct ammonia fuel cells. However, in order to attain

compatibility with a wide variety of fuel cell applications, it is essential to develop and investigate direct ammonia fuel cells that operate at low or medium temperature ranges. In addition to this, no study reporting the development of a low-temperature ammonia fuel cell stack was reported. However, to better comprehend the performance of low temperature direct ammonia fuel cells, it is essential to develop and investigate the fuel cell stacks that operate with ammonia fuel. Hence, in this study, low and medium temperature direct ammonia fuel cells are developed and their performances are investigated at varying operating conditions. Furthermore, a five-cell anion exchange membrane-based direct ammonia fuel cell stack is developed and its performance is tested. Alkaline electrolyte based direct ammonia fuel cells provide an opportunity to utilize electrochemical oxidation properties of ammonia to generate electrical energy. Marginal number of studies have investigated the performance of alkaline electrolyte based direct ammonia fuel cells. Thus, in this study, alkaline electrolytes comprising of anion exchange membranes and molten alkaline electrolyte salts are utilized to develop, analyse and evaluate the performances of direct ammonia fuel cells.

# CHAPTER 3 : EXPERIMENTAL APPARATUS AND PROCEDURE

This chapter entails the description of the experimental procedures conducted and the apparatus utilized. A detailed description of each equipment used is included. The experimental methodology followed is also discussed.

## 3.1 Fuel cell components

In this section, a detailed description of the fuel cell components utilized is provided. The specifications and properties of each component are described in detail.

### 3.1.1 Anion exchange membrane

Anion exchange membrane is the primary component of the developed fuel cell. The $O_2$ and $H_2O$ molecules react electrochemically at the cathode in the presence of a catalyst to form hydroxyl anions according to the cathodic reaction depicted by equation (2.10). The produced hydroxyl anions travel through the anion exchange membrane to reach the anode side, where ammonia fuel is fed. Ammonia molecules and the hydroxyl ions react electrochemically at the anode side to complete the half-cell electrochemical reactions required for fuel cell operation. The functionality of the anion exchange membrane utilized is described as strong base anion exchange. The functional group of the fabricated membrane belongs to quaternary ammonium. Quaternary ammonium ions are structured as depicted in Fig. 3.1. The N-R bonds comprise of a bond between the nitrogen atom and an aryl or alkyl group of atoms. These type of cations contain a permanent charge and are not dependent on the solution pH. The anion exchange membrane utilized for fabricating the direct ammonia fuel cell is shown in Fig. 3.2.

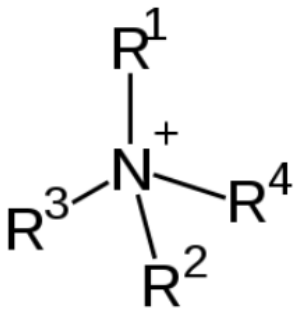


Fig. 3.1 Quaternary ammonium cation

Fig. 3.2 Anion exchange membrane

The technical specifications of the anion exchange membrane utilized are listed in Table 3.1.

Table 3.1 Technical specifications of the anion exchange membrane

| | |
|---|---|
| Functional group | Quaternary ammonium |
| Functionality | Strong base anion exchange membrane |
| Ionic form | Chloride |
| Thickness (mm) | $0.5 \pm 0.025$ |
| Max. current density ($A/m^2$) | <500 |
| Mullen burst test strength (psi) | >80 |
| Maximum stable temperature ($^oC$) | 90 |
| Color | Light yellow |
| Polymer structure | Cross link between gel polystyrene and divinylbenzene |

The functional group of the anion exchange membrane comprises of quaternary ammonium and the ionic form is chloride. The thickness of the membrane is measured to me $0.5 \pm 0.025$ mm. In addition, the maximum current density applicable with this membrane is limited to 500 $A/m^2$. Furthermore, it has a Mullen burst strength of higher than 80 psi. The maximum stable temperature that the membrane can survive is limited to

90$^{o}$C. The polymer structure utilized to develop the anion exchange membrane comprises of a gel polystyrene cross-linked with divinylbenzene. In order to activate the membrane, it was immersed in 1 M KOH solution before the experiments.

### 3.1.2 Gas diffusion layers

Gas diffusion layers are important components in majority of fuel cell and electrolyzer systems. In order to achieve efficient gas diffusion from the flow channel plates to the layers of coated catalyst or the membrane, pathways are required. Gas diffusion layers are fabricated with appropriate pathways for diffusion of reactant gases. The gas diffusion layer comprises of a micro-porous layer that aids in several functions. Firstly, the micr-porous layer helps to keep the resistance at the contact surface with the catalyst layer to a minimal value. Secondly, it aids in limiting the transfer of catalyst particles into the gas diffusion layer as the fuel cell stack is pressurized. Thirdly, in cases where water management is significant, micro-porous layers aid in effective management of water molecules. Furthermore, the gas diffusion layers are fabricated with sufficient mechanical properties to withstand pressure forces that are exerted during tightening. Sufficient strength is required to prevent deforming or cracking that may constrain the fluid flows. Moreover, the gas diffusion layers are treated with hydrophobic treatment in order to enhance the water transport and prevent flooding that can deteriorate the fuel cell performance. Teflon or PTFE is utilized to achieve the hydrophobic treatment. The gas diffusion layers utilized in this study are platinum black coated carbon fiber papers. The fabricated fuel cell entails electrochemical oxidation of ammonia. In order to initiate and facilitate the oxidation reaction, platinum black catalyst is required [39]. Furthermore, the half-cell reduction reaction occurring at the cathode also requires platinum catalyst for the electrochemical reduction of oxygen. The platinum catalyst loading of the layer is 0.45 mg/cm$^2$.The catalyst layer comprises of 40% platinum on Vulcan Carbon support. Their characteristics comprise of high strength with low electrical resistance. In addition, electrochemical corrosion is also minimal. The diffusion layer is made from carbon fibers that are known to have a high modulus as well as tensile strength. The specifications of the gas diffusion layer are listed in Table 3.2. The utilized gas diffusion layer is shown in Fig. 3.3.

Table 3.2 Specifications of the gas diffusion layer

| | |
|---|---|
| Air permeability ($cm^3/(cm^2s)$) | 1 ± 0.6 |
| Platinum black loading ($mg/cm^2$) | 0.45 |
| Catalyst Type (%) | 40% Platinum on Vulcan |
| Thickness (mm) | 0.24 ± 0.025 |
| Electrical resistivity through plane ($m\Omega cm^2$) | <12 |
| Porosity (%) | 80 |
| PTFE treatment (wt %) | 5 |

Source: [82]

The permeability of the diffusion layers to air is $1 \pm 0.6$ $cm^3/cm^2s$. Furthermore, the layers comprised of a 0.45 $mg/cm^2$ loading of platinum black catalyst. The thickness of the layers is measured to be $0.24 \pm 0.025$ mm. In addition, the electrical resistivity is lower than 12 $m\Omega cm^2$ through plane. Further, the porosity of the utilized layers is 80%. The PTFE treatment used to provide the hydrophobic surface comprises of 5 wt%.

Fig. 3.3 Gas diffusion layer

### 3.1.3 Flow channel plates

The flow channel plates are essential in fuel cell stacks to separate different cells from each other and provide a flow field for fluid flow. Each cell comprises of a membrane, catalyst layers and gas diffusion layers on both sides of the membrane. The flow channel plates complete the cell by sandwiching the assembly. The flow channel plates are also known as bipolar plates as they are designed to act as anodes as well as cathodes for two adjacent

cells. The reactant fuel flows through the flow field at the anode side of one cell and passes over to the anode sides of next adjacent cells through flow channels designed in the bipolar plates. The oxygen and water molecules fed at the cathode side of the stack, pass flow through the flow channels on the cathode side of one cell and pass through the bipolar plate flow channels to the cathode sides of other adjacent cells. The utilized flow channel plates are shown in Fig. 3.4. The bipolar plates can be fabricated from different materials including graphite, metals or composites.

Fig. 3.4 Flow channel plate

In this study, the stainless steel plates have been utilized. The Stainless steel plates have significantly high strength. High strength is desirable for stack applications, as the stacked cells are pressurized together to prevent any reactant leakages. The stainless steel plates have sufficient strength to withstand the high pressures exerted. In addition, they are resistant to corrosion. Ammonia being a corrosive gas can deteriorate the flow channel plates affecting the fuel cell performance. Hence, corrosion-resistant materials such as stainless steel are appropriate for continuous and efficient fuel cell performance.

### 3.1.5 Gaskets

Rubber gaskets are placed between every bipolar plate. These are essential to avoid any reactant gases from leaking out of the fuel cell assembly. In addition to this, rubber gaskets allow appropriate compression of the assembly. Fig. 3.5 shows the gaskets utilized in the present study. High compression pressures are applied to the fuel cell assembly to avoid any leakages and minimize the contact resistances by minimizing the separation distances between each component. Rubber gaskets enable sufficient compression pressures to be applied. Hence, resulting in higher fuel cell efficiencies and better performance. The thickness of the gasket utilized is 0.9 mm.

Fig. 3.5 Rubber gaskets for bipolar plates

### 3.1.6 End plates

Fuel cells deploy end plates that complete the stack assembly. All the components of the stack are enclosed between two end plates. Furthermore, end plates aid in the compression of the fuel components. They prevent leakage of any reactant or product gases. In addition, end plates are designed with entry and exit passages for inflow and outflow of gases. In order to avoid short-circuit of the fuel cell, it is essential to ensure the end plates are electrically insulated. End plates utilized in the present study are shown in Fig. 3.6.

Fig. 3.6 Fuel cell endplate

### 3.1.7 Humidifier

The electrochemical reduction reaction at the cathode includes oxygen as well as water molecules as depicted in the equation (2.10). In the present study, humidified compressed air is utilized at the cathode inlet. A bubbler humidifier setup is utilized in order to attain increased humidity and water molecules to react electrochemically at the cathode. An air compressor is utilized to provide pressurized air.

### 3.1.8 Fuel cell stack assembly

The procedure utilized to build the single-cell direct ammonia fuel cell is depicted in Figure 3.7. Firstly, the anion exchange membrane is taken according to the size of the flow channel plates and endplates. Secondly, the catalyst coated gas diffusion electrodes are placed on either side of the membrane to obtain a membrane electrode assembly. Thirdly, the flow channel plates are prepared with rubber gaskets to provide appropriate sealing. Next, the membrane electrode assembly is sandwiched between two flow channel plates. The sandwich of components is placed with the end plate and the top plate with gas inlet and outlet flow channels. The complete assembly is then pressurized using washers and nuts to ensure no leakages occur during operation. The procedure for stack development is similar, however, multiple cells are sandwiched together before pressuring between the end plates.

.

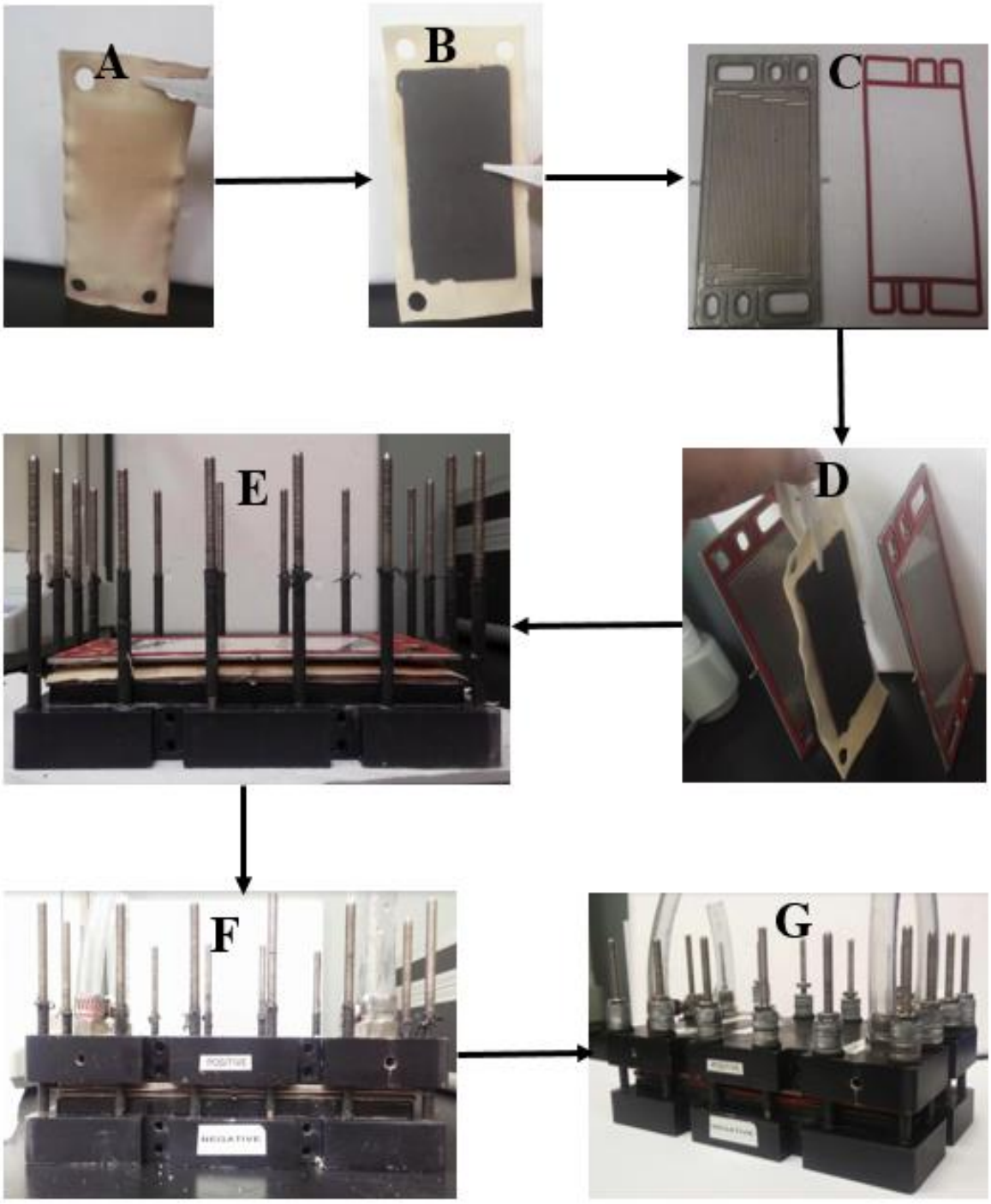


Fig. 3.7 Steps in the development of direct ammonia fuel cell: (A) Anion exchange membrane, (B) Membrane electrode assembly, (C) Preparing flow channel plates sealed with rubber gaskets, (D) Membrane electrode assembly sandwiched between two flow channel plates, (E) Flow channel plates and membrane electrode assembly place with the end plate, (F) Top plate enclosing the assembly, (G) Tightening of assembly with washers and nuts.

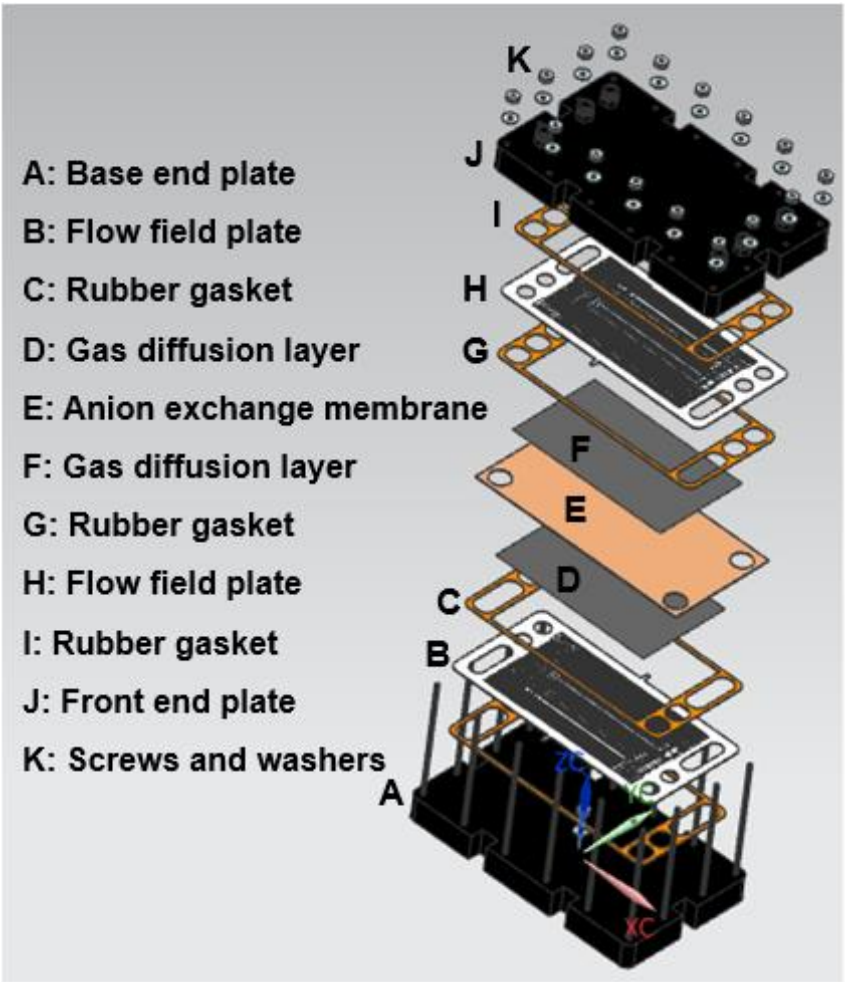


Fig. 3.8 Exploded view of the single cell fuel cell assembly

The overall single cell and stack assemblies are shown in Figures 3.8-3.10. Figure 3.8 depicts an exploded view of the single cell assembly of fuel cell components. As can be depicted from the figure, the complete assembly is sandwiched between the base end plate and the front end plate. The assembly comprises of a central component of an anion exchange membrane. Either side of the anion exchange membrane exist the platinum black catalyst coated gas diffusion electrodes forming a membrane electrode assembly. The membrane electrode assembly is placed between two flow channel plates that allow the passage of anodic reactants at the anodic side of the membrane and the cathodic reactants at the cathodic side. Rubber gaskets are placed on either side of the flow channel plates as depicted in the figure to prevent any leakages during the operation of the fuel cell.

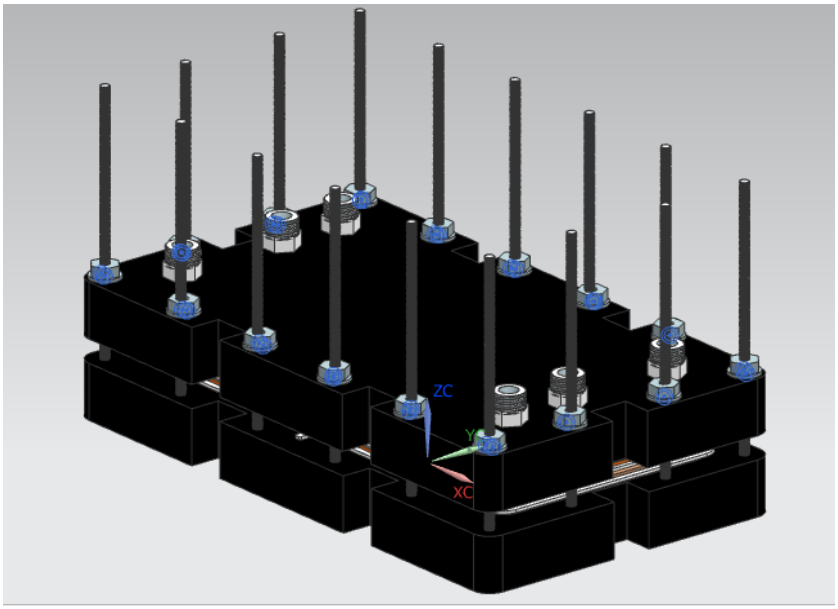


Fig. 3.9 CAD model of single cell assembly

Furthermore, a five-cell fuel cell stack is also developed and tested. The stack assemblies are depicted in Figures 3.10 and 3.11. Different components are labelled for better demonstration. Washers and nuts are used to tightly compress the assembly. Tightening and compressing are significant to prevent any fuel leakages. Leakages in case of hydrogen fuel cells can be fatal due to the high reactivity of hydrogen. However, ammonia is known to be less combustible as compared to hydrogen. In addition, ammonia leakages are also detectable due to its pungent smell. However, ammonia also poses other health hazards. Hence, the stack assembly needs to be tightly compressed to prevent any leakages. In a five-cell stack arrangement, five cells comprising of five anion exchange membranes and membrane electrode assemblies are sandwiched between bipolar flow channel plates, assembled, and pressurized between the base and front end plates. The bipolar plates comprise of flow fields that allow efficient passage of reactants over the membrane electrode assemblies. By utilizing gaskets and flow channels on the bipolar plates, the reactant flow is controlled to allow the ammonia gas to pass over the anode side of each cell in the stack. Similarly, the humidified air is allowed to flow over only the cathode side of each stack cell.


Fig. 3.10 Five-cell direct ammonia fuel cell stack

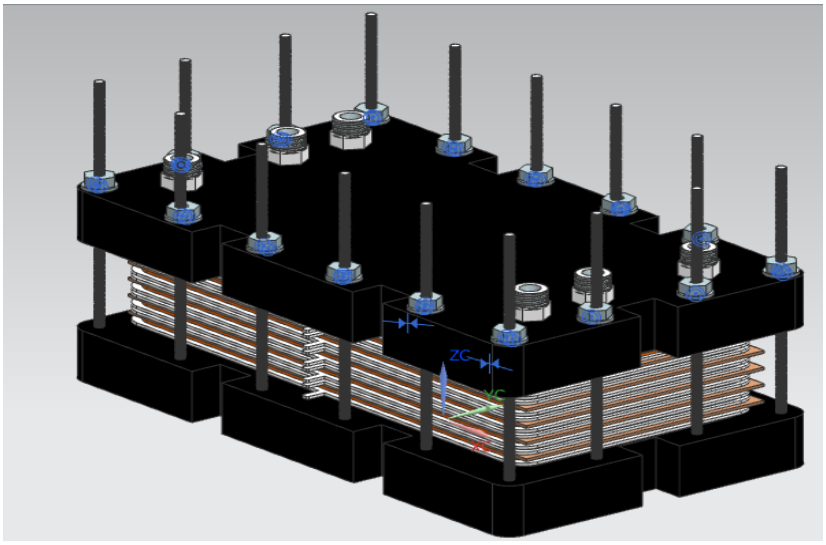

Fig. 3.11 CAD model of the five-cell direct ammonia fuel cell stack

### 3.2 Measurement devices

In this section, the devices utilized for measurements and experimentations performed to assess the performance of the fuel cell are discussed in detail.

#### 3.2.1 Potentiostat

In order to assess the fuel cell performance, several tests are performed by using the potentiostat. These include the open circuit voltage test, polarization test and electrochemical impedance spectroscopy test. In the open circuit voltage test, the voltage across the anode and cathode is measured in the absence of any load or output current. This represents the cell or stack voltage in the absence of any activation, Ohmic or concentration

losses. Furthermore, the polarization curve also known as the I-V curve provides essential information about the fuel cell performance. The potentiostat draws different output current values from the fuel cell and measures the corresponding voltage at these currents. The obtained I-V curve provides information about the activation, Ohmic and concentration losses occurring in the fuel cell at varying current density values. The electrochemical impedance spectroscopy test provides essential information about the impedances present in the cell. Alternating currents of small amplitudes are utilized at varying frequencies. Gamry Reference 3000 Galvanostat/Potentiostat/ZRA is utilized in the present study. The device has maximum currents and voltage values of ±3 A and ± 32 V respectively [83]. The Gamry Ref 3000 device is capable of operating multiple functions including voltage measurements, galvanostatic measurements, potentiostatic measurements and impedance spectroscopy measurements.

### 3.2.2 Flow meters

Flow meters utilized in the present study are FMA series FMA-1600A flow meters. These type of flow meters use the differential pressures theory in conjunction with laminar flows to determine the volume or mass flow rates. Component sections within the flow meters produce a laminar flow and the corresponding pressure drops are related to the flow rates according to the Poiseuille theory. The device contains pressure sensors to detect the amount of pressure losses in the laminar flow sections. Furthermore, other pressure and temperature sensors are attached to apply correction factors according to the actual conditions. Flow meter specifications are listed in Table 3.3.

Table 3.3 Specifications of the FMA-1600A flow meter

| | |
|---|---|
| Response time | 0.01 seconds |
| Maximum pressure | 145 psig |
| Repeatability | ±0.2% |
| Span shift | 0.02% FS/°C/atm |
| Humidity range | 0-100% |
| Turndown ratio | 200:1 |
| Operating temperature | 263 K-323 K |
| Zero shift | 0.02% |
| Supply voltage | 7-30 V |
| Accuracy | ±(0.8% of reading + 0.2% FS) |
| Flow rate measureable | 125% FS |
| Typical supply current | 35 mA |

Source: [84]

### 3.2.3 Thermocouples

For temperature measurements, K-type thermocouples are utilized along with Omega data acquisition system (OM-DAQPRO-5300 data logger). The data logging system allows temperature measurements of eight thermocouples simultaneously. In addition, the device is equipped with graphical temperature displays and acquisition systems to record the temperature variations. The specifications of the Omega DAQPRO temperature measurement device are given in Table 3.4.

Table 3.4 Specifications of the OM-DAQPRO-5300 temperature measurement system

| | |
|---|---|
| Thermocouple type | K type |
| Temperature range | -250°C-1200°C |
| Accuracy | ±0.5% |
| Resolution | 0.1°C |
| Cold junction compensation | ±0.3°C |

Source: [85]

## 3.3 Experimental setup for the anion exchange membrane-based direct ammonia fuel cell

Ammonia gas at 1 bar pressure is passed at the anode side of the fuel cell. The expected anodic electrochemical reaction is depicted by equation (2.9). The schematic of the working principle of a direct ammonia anion exchange membrane fuel cell is depicted in Fig. 3.12. The experimental setup utilized in the present study to investigate the performance of the direct ammonia fuel cell is depicted in Fig 3.13. Flow meters, thermocouples and data loggers are utilized for flow and temperature measurements.

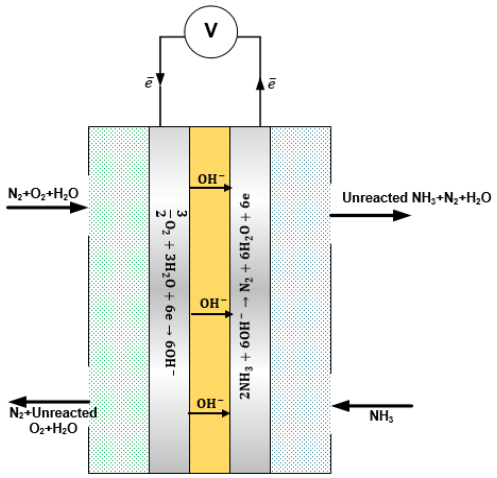


Fig. 3.12 Schematic of direct ammonia anion exchange membrane fuel cell

In case of the single cell arrangement, the ammonia gas feed is allowed contact with one side of the membrane, and the unreacted ammonia gas exits the cell from the anode exit. When ammonia is fed at the anode side of the five-cell fuel cell stack, it is allowed to be exposed to the anode side of each cell in the stack. The flow channel plates and gaskets are designed to connect the inflow of fuel at the stack anode to the anode side of each cell in the stack. Furthermore, in order to complete the cathodic half-cell fuel cell reaction depicted by equation (2.10), oxygen and water molecules are required at the cathode. These are obtained by humidified air input at the cathode side of the fuel cell. A compressor is utilized to provide compressed air at 6 L/m. The humidifying setup comprises of a bubbler humidifier. An enclosed conical flask with one inlet and one outlet filled with water is fed with pressurized air. The air bubbles become humidified prior to their exit from the conical flask as they pass through the water pool in the flask. A heater and temperature controller is utilized to control the temperature of the humidifier. Varying temperatures are utilized to assess the fuel cell performance under these conditions. For electrochemical measurements, a potentiostat is utilized as depicted in Figure 3.14. The tests conducted to assess the fuel cell performance include open circuit voltage test, polarization curves and electrochemical impedance spectroscopy.

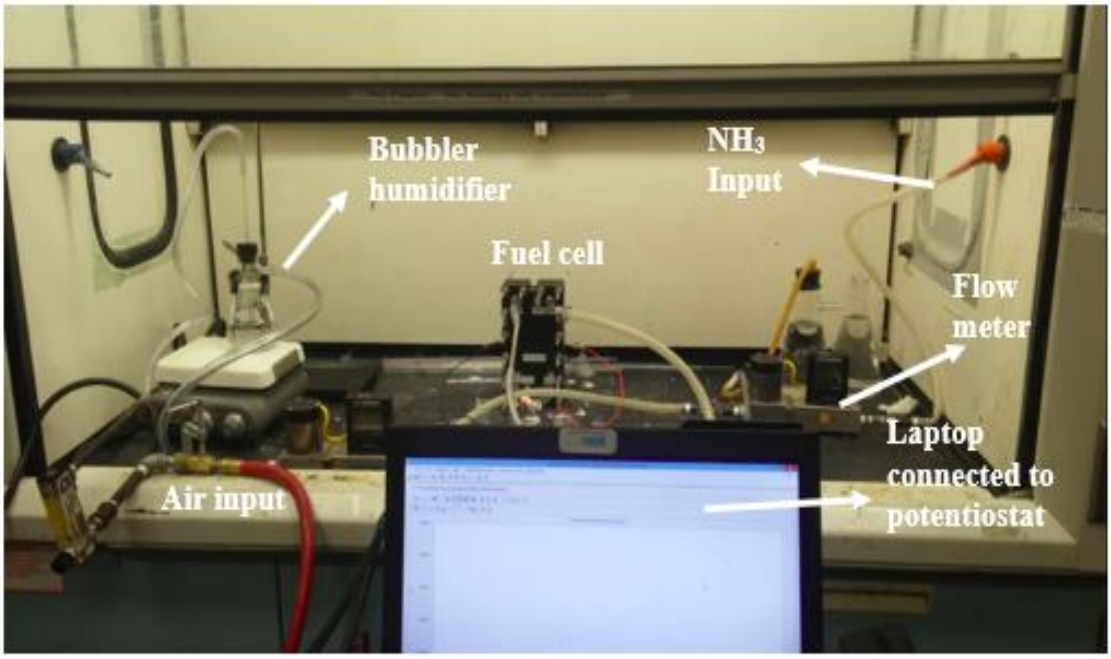


Fig. 3.13 Experimental setup to test the fuel cell performance.

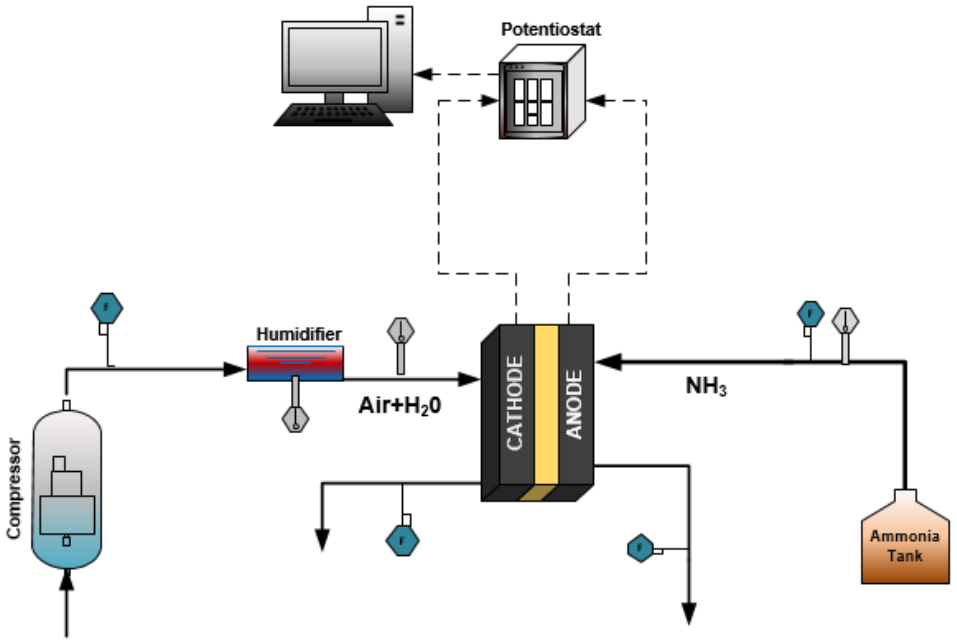


Fig. 3.14 Schematic of the experimental setup with gaseous ammonia

Ammonia gas is highly soluble in water. Dissolving gaseous ammonia in water forms aqueous ammonia that primarily comprises of gaseous $NH_3$ molecules dissolved in water. In addition, a small percentage of ammonium hydroxide ($NH_4OH$) molecules may also be found. In the present study, aqueous ammonia of concentration 1 M is utilized.

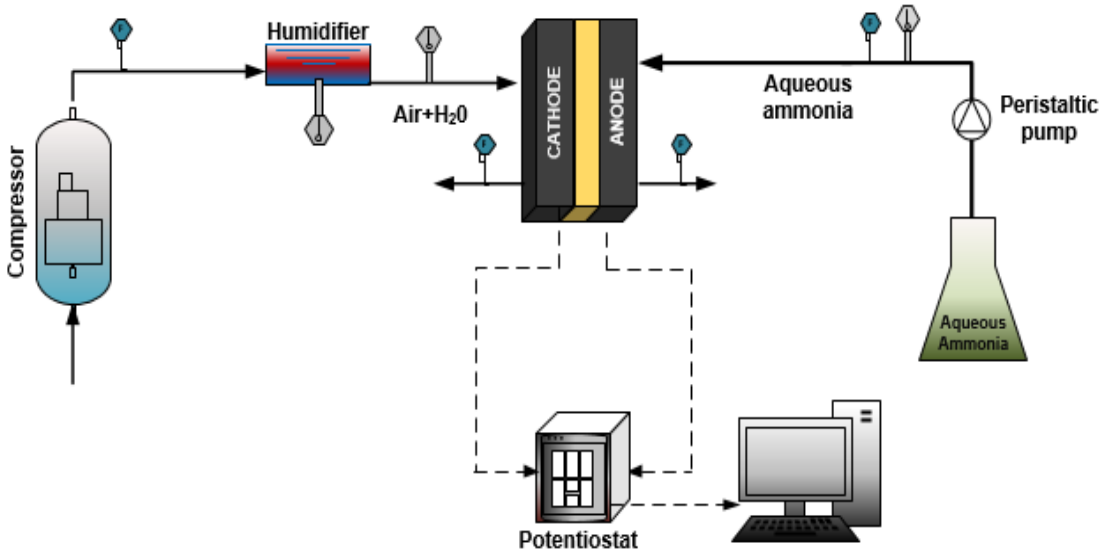


Fig. 3.15 Schematic of the experimental setup with aqueous ammonia

The schematic of the experimental setup utilized for aqueous ammonia fuel is depicted in Fig. 3.15. The aqueous ammonia solution of a concentration of 1 M is pumped through a peristaltic pump that maintains a constant flow rate of 126 ml/min. A heater with temperature controller is utilized to vary the solution temperature to analyse the effect on fuel cell performance. Humidified air is passed at the cathode side with same conditions that are set for experiments with gaseous ammonia. The anode fuel outlet comprising primarily of unreacted aqueous ammonia is recirculated by connecting the anode outlet to the ammonia solution reservoir. Sufficient sealing is required to prevent any fuel leakages as the aqueous solution can deteriorate the fuel cell components.

### 3.4 Experimental setup for a molten alkaline electrolyte based direct ammonia fuel cell

In the present study, a molten alkaline electrolyte based direct ammonia fuel cell is also developed and investigated. The molten electrolyte comprises of a mixture of potassium hydroxide and sodium hydroxide in a mole ratio of 1:1. One mole of potassium hydroxide and sodium hydroxide powders (Sigma Aldrich) are mixed together in a flask and heated to temperatures of over 200$^{o}$C. Nickel coils are utilized as the electrodes. Stainless steel tubes are utilized as gas passages. Ammonia gas is inserted in the molten salt reactor at a gage pressure of 1 Bar. Humidified air is input at the cathode side to obtain the required $O_2$ and $H_2O$ molecules for the half-cell cathodic reaction. A bubbler type humidifier setup is utilized as described earlier. All experiments are carried in the fume cupboard for safe operation. The molten electrolyte temperatures are varied between 220$^{o}$C and 280$^{o}$C to analyse the effect of varying temperatures on the fuel cell performance. These temperatures are chosen as lower temperatures than 200$^{o}$C favor the solidification of the molten electrolyte that deteriorates the fuel cell performance. In addition, temperatures higher than 300$^{o}$C are appropriate for high-temperature fuel cells. However, in the present study, low and medium temperature direct ammonia fuel cells are investigated. The nickel coil electrode area is measured to be 2.4±0.5 cm$^2$ for both anode and cathode respectively. The fuel cell performance is investigated through performance parameters of open circuit voltages, peak power densities, short circuit current densities as well as energy and exergy efficiencies.

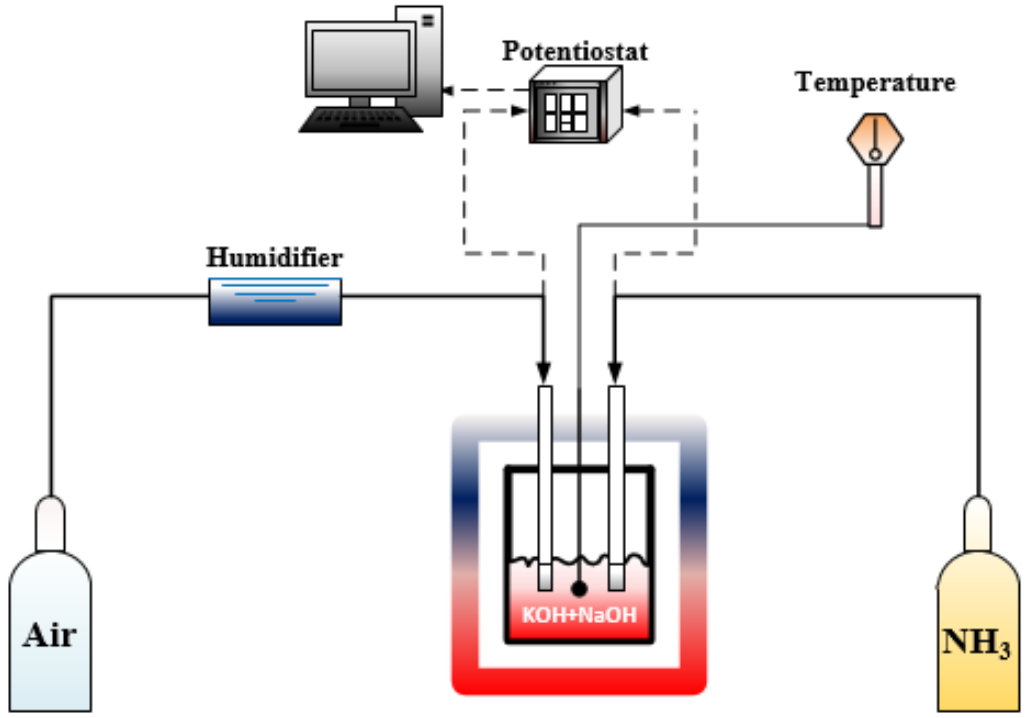


Fig. 3.16 Schematic representing the experimental setup utilized to test the molten alkaline electrolyte based direct ammonia fuel cell

Molten salt alkaline electrolyte based direct ammonia fuel cells provide the advantage of a moderately high temperature operating range increasing the reaction rates. Ammonia, being a naturally stable specie does not provide comparatively high fuel cell performances. However, higher operating temperatures are expected to increase the electrochemical reaction rates of ammonia. Hence, in the present study, a molten salt-based fuel cell is also developed to analyse and evaluate the comparative performances.

# CHAPTER 4 : ANALYSIS AND MODELLING

In this chapter, the electrochemical modelling of the direct ammonia fuel cell is described. Furthermore, the electrochemical impedance spectroscopy modelling of the studied fuel cell is also presented. In addition, a novel hybrid regenerative-electrode ammonia fuel cell and battery system is presented as an embodiment to utilize ammonia as a fuel in fuel cell systems. The system is proposed and the analysis is described in detail.

## 4.1 Thermodynamic and electrochemical modelling

The thermodynamic and electrochemical analysis of the proposed system is described in this chapter. Ammonia is utilized as the fuel and is fed into the anode compartment. The half-cell electrochemical reaction of ammonia occurring at the anode in the presence of a platinum black catalyst is expressed by equation (2.9), the oxygen reduction reaction occurring at the cathode is expressed by equation (2.10) and the overall fuel cell reaction is given by equation (2.11).

The Gibbs function for the overall reaction can be determined as follows:

$$\Delta G = \Delta H - T\Delta S \tag{4.1}$$

where $\Delta G$ denotes the change in Gibbs function between the products and reactants of the given reaction.

During fuel cell operation, the chemical energy of the reactants is converted into electrical energy. The electrical cell potential and current output exhibit the converted electrical energy. Under reversible operating conditions, maximum cell potential is achieved. This cell potential is referred to as the reversible cell potential. At standard conditions of 1 atm pressure and a temperature of 25ºC, the reversible cell potential is expressed as

$$E_r^0 = -\frac{\Delta G_{(T_0,P_0)}}{nF} \tag{4.2}$$

where $n$ denotes the number of moles of electrons transferred and $F$ denotes the Farady's constant, $\Delta G_{(T_0,P_0)}$ denotes the change in Gibbs function at standard conditions. The reversible cell potential varies with changing partial pressures or concentrations of products

and reactants of a given reaction. The Nernst equation can be utilized to obtain an expression for the reversible fuel cell potential as a function of these parameters [86]:

$$E_{FC} = E_r - \frac{RT}{nF}\ln(K) \tag{4.3}$$

where K denotes the equilibrium constant. The equilibrium constant entails the ratio between the molar fractions of reactants and products. In the presence of inert gases such as nitrogen in the reactant streams, the reversible potential is effected slightly at low temperatures. $E_{FC}$ represents the cell voltage in the absence of any current output. When current is drawn from the fuel cell, various voltage losses occur in the fuel cell, which need to be considered. The fuel cell voltage can be expressed as

$$V_{FC} = E_{FC} - V_{act} - V_{ohm} - V_{conc} \tag{4.4}$$

The activation overpotential $V_{act}$ occurs due to the electrochemical reaction resistance at the electrodes. Furthermore, in electrochemical reactions, the reactant atoms and molecules are adsorbed at the electrode surface. The accompanying physiochemical processes also affect the activation overpotential. The activation overpotential can be related to the current density by the Butler-Volmer equation:

$$J = J_0\{\exp\left(\frac{\alpha nFV_{act}}{RT}\right) - \exp\left(-\frac{(1-\alpha)nFV_{act}}{RT}\right)\} \tag{4.5}$$

where $J_0$ denotes the exchange current density. The exchange current density denotes the current density at which the rates of backward and forward reactions are equal. Hence, the charges crossing the electrolyte and electrode interface are equal, such that equal amounts of products are reduced and reactants are oxidized in the half-cell electrochemical reaction. In addition, the exchange current density indicates the ease for an electrochemical reaction to occur. The parameter $\alpha$ denotes the transfer coefficient. The transfer coefficient depends on the electrode reaction. The temperature is denoted by $T$ and the gas constant is denoted by $R$, the number of moles of electrons transferred are denoted by $n$ and the Faraday's constant is denoted by $F$. The activation overpotential is represented by $V_{act}$. Equation (4.5) can be rearranged for large electrode over potentials, to obtain a general expression for the activation overpotential:

$$V_{activation} = \frac{RT}{\alpha nF} \ln\left(\frac{J}{J_0}\right) \tag{4.6}$$

The above equation is also referred to as the Tafel equation. The total activation overpotential for the fuel cell can be expressed as the sum of the cathodic and anodic activation overpotentials:

$$V_{act} = V_{act,C} + V_{act,A} \tag{4.7}$$

where the cathodic and anodic over potentials can be determined according to equation (4.6):

$$V_{act,i} = \frac{RT}{\alpha nF} \ln\left(\frac{J}{J_{0,i}}\right) \tag{4.8}$$

where the subscript $i$ denotes the anode or cathode. According to equations 2.9 and 2.10, 6 moles of electrons ($n$) are transferred in the electrochemical reactions. The anodic and cathodic exchange current densities vary according to the reactions occurring in their vicinity. When the fuel cell current density is increased, an increase in the electrochemical reaction rate occurs in order to supply the required amount of electron transfer required. As the reaction rates increase, the reactants are consumed more swiftly at the electrodes. However, the mass transfer rate of the reactants is limited. Due to this, the reactant availability near the available reaction sites is limited. Furthermore, as the fed reactants are converted into reaction products, the reaction products can over accumulate at the reaction sites. This also hinders the transport of new reactant molecules from reaching the reaction sites. This phenomenon creates an upper limit on the amount of current that can be drawn from the cell. The maximum current density that can be drawn from the fuel cell is referred to as the limiting current density. As the current density approaches the limiting current density, the limiting mass transfer rate inhibits any further increase. The polarization loss occurring due to this phenomenon is known as concentration overpotential($V_{conc}$).

For a given half-cell reaction at an electrode, the limiting current density can be expressed as [86]

$$J_L(x) = \frac{nFC_{i,avg}}{L/D_{a-b}^{eff}} \tag{4.9}$$

where $n$ denotes the number of moles of participating electrons, $F$ represents the Faraday's constant, $C_{i,avg}$ denotes the average concentration of specie $i$, $L$ denotes the thickness of the porous layer, $D_{a-b}^{eff}$ represents the effective diffusion coefficient of specie $a$ in specie $b$. The average concentration of specie $a$ can be determined as

$$C_{a,avg}(x) = C_{a,avg,i} e^{-\frac{h_m x}{b v_{avg}}} \tag{4.10}$$

where $C_{a,avg,i}$ denotes the average concentration of specie $a$ at the inlet of the flow channel, $b$ represents the width of the flow channel, $v_{avg}$ denotes the average velocity of flow, $x$ represents the flow distance, $h_m$ denotes the mass transfer coefficient that can be obtained from:

$$Sh = \frac{h_m D_h}{D} \tag{4.11}$$

where $Sh$ represents the Sherwood number, $D$ denotes the diffusion coefficient and $D_h$ represents the hydraulic diameter. The concentration polarization can be determined from the limiting current density as

$$V_{conc,i} = \frac{RT}{nF} \ln\left(\frac{J_{L,i}}{J_{L,i} - J}\right) \tag{4.12}$$

where the subscript $i$ represents the anode or cathode. The total concentration overpotential can be expressed as

$$V_{conc} = V_{conc,a} + V_{conc,c} \tag{4.13}$$

Furthermore, as current is drawn from the cell, the voltage losses that occur due to the electrical resistances within the cell are classified as Ohmic overpotentials. The Ohmic overpotential ($V_{ohm}$) can be calculated as

$$V_{ohm} = JR \tag{4.14}$$

where $R$ represents the total electrical resistances within the cell and $J$ denotes the current density.

### 4.2 Electrochemical impedance spectroscopy modeling

In electrochemical cells, various types of impedances are present. These impedances hinder the passage of current through the cell. An ideal resistor restricts current flow according to the Ohm's law relation:

$$I = \frac{V}{R} \tag{4.15}$$

The resistance of an ideal resistor is independent of the frequency and obeys the Ohm's law in all circumstances. However, other types of circuit elements exist that are dependent on the frequency of signals. These include inductors and capacitors. For a resistor, the impedance can be evaluated from its resistance itself, as the electron flow is independent of the frequency:

$$Z_{resis} = R \tag{4.16}$$

In the case of a capacitor, the relation between the capacitance, impedance and frequency can be expressed as follows:

$$Z_{cap} = \frac{1}{jwC} \tag{4.17}$$

where $C$ denotes the capacitance and $w$ represents the frequency. Furthermore, the impedance of an inductor element can be evaluated from the relation:

$$Z_{ind} = jwL \tag{4.18}$$

where $L$ denotes the element inductance and $w$ denotes the frequency. As can be observed from equations (4.17) and (4.18), the impedance of an inductor increases with increasing frequency and the impedance of a capacitor increases with decreasing frequency. In an electrochemical cell, an electrical double layer may be formed at component interfaces due to accumulation of opposite charges. This resembles a capacitor electrical circuit element as separation of charges occur. Furthermore, an inductor is an electrical conductor that discharges or stores energy through a magnetic field that is generated due to current flow. In a fuel cell, electrical conductors are present, which behave similar to an inductor during a passage of current. In addition to this, other resistances are present within the fuel cell including charge transfer resistance as well as mass transfer resistance. Charge transfer

resistance corresponds to the constraints imposed on electron as well as ion transfer in the electrochemical cell. Mass transfer resistance relates to the resistance imposed on the diffusion of interacting species within the fuel cell.

The electrochemical impedance spectroscopy (EIS) deploys techniques to estimate the impedances present within the cell. The potentiostat creates sudden voltage signals in a sinusoidal pattern. The resulting currents are recorded with their magnitudes and phase angles. Several models exist that represent the impedance elements within the cell. EIS method attracts increased attention due to being a non-destructive testing technique. The impedances comprise of real and imaginary parts and the magnitudes can be determined as

$$|Z| = \sqrt{Z_{real}^2 + Z_{imag}^2} \tag{4.19}$$

In addition to this, the phase angle can be expressed as

$$\phi = \tan^{-1} \frac{Z_{imag}}{Z_{real}} \tag{4.20}$$

The results of the EIS method are represented through Nyquist as well as Bode plots [87]. The Nyquist plot comprises of the impedance results with real parts displayed on the x-axis and the imaginary parts shown on the y-axis at varying frequencies. However, the Bode plot is a representation of the impedances with magnitudes and phase angles displayed on the primary and secondary y-axis respectively and the frequency displayed on the x-axis. Several models of electrochemical impedance circuits have been proposed for fuel cells [88]–[92]. In the present study, several models are tested using the GAMRY Echem analyst software. The best-fit fuel cell electrochemical impedance model that provided results with least errors is depicted in Figure 4.1.

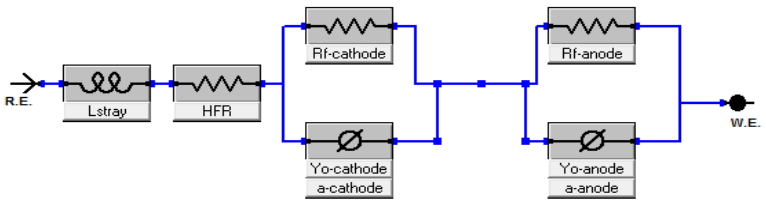


Fig. 4.1 Electrochemical impedance equivalent circuit model

The above circuit includes inductance due to electrical conductors within the fuel cell as well as the anode, cathode and membrane electrical resistances. A constant phase element is utilized in place of capacitance as in electrochemical impedance spectroscopy, ideal capacitor behavior is not observed. The capacitor element acts very similar to a constant phase element in actual cell experiments. The impedance behavior of a constant phase element can be expressed as

$$Z = \frac{\frac{1}{Y_o}}{(jw)^a} \tag{4.21}$$

The above equation resembles the capacitor impedance equation (4.17). However, in the case of a capacitor, $Y_o$ represents the capacitance magnitude and the exponent $a$ approaches unity. Gamry Echem Analyst obtains the values of impedances and parameters depicted in the model shown in Fig. 4.1 through the simplex method. The experimental EIS results are matched to the equivalent circuit model depicted in Fig. 4.1 by the simplex method. This method utilizes an algorithm that approximates the values or parameters involved in a circuit model and evaluates the goodness of fit. The trials for parameter estimates are repeated until the fit reaches its upper limit of improving.

### 4.3 Modelling of a novel hybrid system

As an embodiment of utilizing ammonia efficiently in fuel cells, a novel hybrid fuel cell and battery system is conceptually developed and analysed electrochemically and thermodynamically. The novel system proposes a new method to enhance the utilization of electrochemical energy. A regenerative electrode system is utilized.

#### 4.3.1 System description

The schematic of the proposed system is shown in Fig. 4.2. Ammonia is fed at the fuel cell anode where the anodic electrochemical reaction occurs in the presence of a platinum black catalyst. The fuel cell anolyte comprises of aqueous KOH alkaline electrolyte. The fuel cell catholyte consists of aqueous nickel sulfate solution. A nickel electrode is utilized, which acts as the cathode of the fuel cell system during fuel cell operation and as the anode of the battery system during battery operation. During fuel cell operation, the theoretical half-cell oxidation reaction of ammonia occurring at the anode is shown in equation (2.9) and the half-cell reduction reaction of nickel ions occurring at the nickel cathode is represented by

equation (4.22). As the fed ammonia is oxidized at the fuel cell anode, negatively charged electrons build up at the anode side. Whereas, positively charged nickel ions exist at the fuel cell cathode. When connected through an external electrical path, an electron flow is generated between the ammonia fed fuel cell anode and the nickel cathode. Hence, this phenomenon is utilized to generate power. During fuel cell operation, nickel ions are reduced electrochemically to solid nickel particles, this acts as a charging mechanism for the battery. During the battery operation, the nickel electrode acts as the anode where the oxidation of nickel to positive nickel ions occurs during battery discharge. A manganese (IV) oxide cathode and ammonium chloride catholyte is utilized for the battery system. The cathodic half-cell reaction of the battery during discharge results in the formation of aqueous ammonia, which is also utilized as fuel at the fuel cell anode. A salt bridge comprising of sodium chloride maintains the charge balance in the anolytes and cathloytes and avoids the buildup of a highly positive or negative potential at any electrode. The sodium and chloride ions do not participate in the electrochemical reactions.

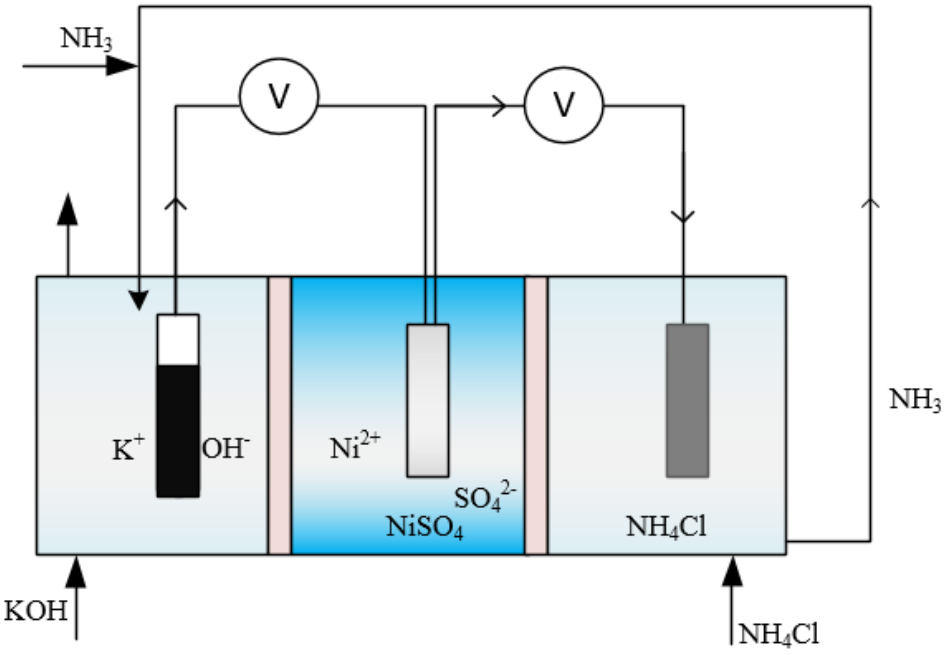


Fig. 4.2 Schematic of proposed regenerative-electrode hybrid ammonia fuel cell-battery system.

### 4.3.2 Analysis

The thermodynamic and electrochemical analysis of the proposed system is described. Ammonia is utilized as the fuel and is fed into the anode compartment. The half-cell electrochemical reaction of ammonia occurring at the anode in the presence of a platinum black catalyst can be expressed by equation (2.9)

The fuel cell cathode compartment comprises of a nickel electrode and an aqueous nickel sulfate catholyte. The cathodic half-cell reaction can be expressed as

$$3Ni^{2+} + 6\bar{e} \rightarrow 3Ni \tag{4.22}$$

The overall reaction for the fuel cell can be expressed as

$$2NH_3 + 6OH^- + 3Ni^{2+} \rightarrow N_2 + 6H_2O + Ni \tag{4.23}$$

During battery operation, the nickel electrode acts as the anode, where nickel is converted to positive nickel ions:

$$3Ni \rightarrow 3Ni^{2+} + 6\bar{e} \tag{4.24}$$

The produced positive nickel ions are utilized during fuel cell operation according to equation (4.22). Hence, a regenerative nickel electrode is utilized in the proposed system, where the nickel electrode is discharged during battery operation and is charged during the fuel cell operation. The battery cathode comprises of manganese (IV) oxide. Ammonium chloride is utilized as the battery catholyte. The cathodic half-cell reaction of the battery can be expressed as

$$6MnO_2 + 6NH_4Cl + 6\bar{e} \rightarrow 3Mn_2O_3 + 6NH_3 + 3H_2O + 6Cl^- \tag{4.25}$$

The overall reaction for the battery system can be written as

$$3Ni + 6MnO_2 + 6NH_4Cl \rightarrow 3Mn_2O_3 + 6NH_3 + 3Ni^{2+} + 3H_2O + 6Cl^- \tag{4.26}$$

At the cathode side of the battery, aqueous ammonia is produced as a product as shown in equation (4.26). This is utilized in the ammonia fuel feed at the fuel cell anode, as shown in Fig. 4.2.

The Gibbs function of a given reaction can be determined according to equation (4.1). During fuel cell or battery operation, the chemical energy of the reactants is converted into electrical energy. The electrical cell potential and current output exhibit the converted electrical energy. Under reversible operating conditions, maximum cell potential is achieved. This cell potential is referred to as the reversible cell potential. At standard conditions of 1 atm pressure and a temperature of 25°C, the reversible cell potential can be expressed by equation (4.2). The reversible cell potential varies with changing partial pressures or concentrations of products and reactants of a given reaction. The Nernst equation can be utilized to obtain an expression for the reversible fuel cell and battery potential as a function of these parameters:

$$E_{FC} = E_r + \frac{RT}{6F}\ln\left(\frac{p_{N_2}}{(p_{NH_3})^2 (C_{OH^-})^6 (C_{Ni^{2+}})^3}\right) \tag{4.27}$$

$$E_B = E_r + \frac{RT}{6F}\ln\left(\frac{(C_{NH_3})^6 (C_{Ni^{2+}})^3 (C_{Cl^-})^6}{(C_{NH_4Cl})^6}\right) \tag{4.28}$$

where $p$ denotes the partial pressure and $C$ denotes the concentration. In the products, water is formed in the liquid state and nickel is formed in the solid state, hence, are not included in equations 4.27 and 4.28.

As current is drawn from the fuel cell, various voltage losses occur, which need to be considered. These include activation, Ohmic and concentration losses. The procedure to account for these voltage losses is described in equations 4.4 to 4.14.

For the battery system, the gravimetric energy density can be expressed as

$$En_d = \frac{\Delta G}{M_{tot}} \tag{4.29}$$

where $\Delta G$ denotes the change in Gibb's function for the overall battery reaction, and $M_{tot}$ represents the total molar weight of the participating reactants.

Furthermore, the energy storage capacity of an electrode material is also an important parameter. The specific energy storage capacity can be evaluated as

$$C = \frac{nF}{3.6M} \tag{4.30}$$

where $n$ denotes the number of moles of electrons transferred, $F$ represents the Faraday's constant and $M$ denotes the molar mass of the electrode material. The molar mass of nickel is 58.7 g/mol.

The useful power output can be expressed in terms of the cell voltage and current density as [93]:

$$\dot{W} = VJ \tag{4.31}$$

where the $V$ denotes the cell voltage, $J$ represents the current density.

The energy and exergy efficiencies of the fuel cell system can be defined as the total useful energy or exergy output divided by the total energy or exergy input [94] :

$$\eta_{en,FC} = \frac{\dot{W}_{FC}}{\dot{N}_{NH_3}\overline{LHV}_{NH_3}} \tag{4.32}$$

$$\eta_{ex,FC} = \frac{\dot{W}_{FC}}{\dot{N}_{NH_3}\overline{ex}_{NH_3}} \tag{4.33}$$

where $\dot{W}_{FC}$ denotes the power output of the fuel cell, $\dot{N}_{NH_3}$ represents the molar flow rate of the ammonia input and $\overline{LHV}_{NH_3}$ denotes the lower heating value of ammonia and $\overline{ex}_{NH_3}$ represents the specific molar exergy of ammonia. The efficiency of the battery can be determined as

$$\eta_b = \frac{E_B}{E_{tn}} \tag{4.34}$$

where $E_B$ denotes the Nernst battery cell voltage and $E_{tn}$ denotes the thermoneutral cell voltage, which is expressed as

$$E_{tn} = -\frac{\Delta h}{nF} \tag{4.35}$$

Note that the thermoneutral voltage represents the voltage of the cell when all the stored chemical energy in the battery is converted to electrical energy.

### 4.4 Experimental uncertainty analysis

In an experimental study, it is essential to quantify the associated experimental uncertainties to better comprehend the differences obtained in the results at varying

operating parameters. Quantification of the experimental uncertainty can be evaluated on the basis of systematic errors and random errors. The systematic errors are classified as those errors in the experiments that are caused due to equipment inaccuracies or faulty design of experiments that lead to results being offset from the actual value. These type of errors lead to a bias in the results from the actual value. Furthermore, random errors are classified as those type of errors that cause fluctuations in the obtained results when the experiments are repeated. These can be due to various reasons including the fluctuations in the uncontrolled experimental environmental parameters as well as errors associated with personnel recording the measurements. Where $S$ denotes the systematic error and $R$ denotes the random errors, the resultant uncertainty can be evaluated as follows:

$$U = \sqrt{R^2 + S^2} \tag{4.36}$$

In the present study, the systematic error is determined from the GAMRY Reference 3000 equipment as specified by the manufacturer to be ±0.3 % of obtained readings. In order to determine the random errors, each experiment is repeated three times. The variation in the three experimental results allowed the calculation of the relative standard deviation as follows:

$$RD = \frac{SD}{Avg} \text{x} 100 \tag{4.37}$$

where $SD$ denotes the standard deviation and $Avg$ represents the mean value. Hence, in this way the experimental uncertainties are evaluated in the present study.

# CHAPTER 5 : RESULTS AND DISCUSSION

In this chapter, the results of the fuel cell modelling as well as experimental results are presented, analysed and discussed. In addition, the performance of the fuel cell at varying humidifier temperatures is presented and discussed. Furthermore, the performance of the proposed hybrid fuel cell-battery system is evaluated and analysed for varying system operating parameters.

## 5.1 Performance results of the single-cell anion exchange membrane direct ammonia fuel cell

The theoretical open circuit voltage for ammonia fuel cell is obtained by equation (4.3) as 1.17 V. However, the present study experimental results confirm the presence of unaccounted irreversibilities. At ambient temperature (25$^{o}$C) and 1 bar inlet ammonia pressure, the open circuit voltage is observed to be 280 mV from the experimental results. This difference between theoretical and experimental open circuit voltages can be attributed to various factors such as fuel crossover and low reactivity of ammonia molecules. The phenomenon of fuel cross over has been investigated in previous studies and a decrease in open circuit voltage has been attributed to other electrode reactions at either electrodes that cause short circuit currents within the cell [95]–[99]. Fig. 5.1 depicts the phenomenon of fuel crossover and the short circuit currents in an anion exchange membrane direct ammonia fuel cell.

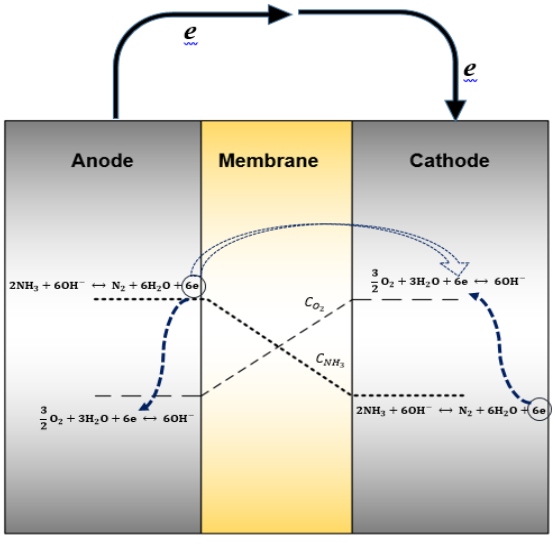


Fig. 5.1 Schematic representing short-circuit currents due to fuel cross over

In addition to this, other factors can be possible that lower the open circuit voltage of direct ammonia anion exchange membrane fuel cells from the theoretical value that lies in vicinity of 1 V. Considering these irreversibilities cause a drop in voltage from the open circuit value, voltages in the vicinity of experimentally obtained values are considered for analysis purposes. The theoretical modelling parameters of the anion exchange membrane fuel cell are listed in Table 5.1. The experimental and theoretical results of the fuel cell at ambient temperature and 1bar pressure are depicted in Figures 5.2 and 5.3. The initial part of the curve at low current densities corresponds to activation polarization, which is prevalent up to current densities of 30-40 $A/m^2$. As the current drawn from the fuel cell is increased, Ohmic polarization dominates the voltage losses as can be observed from the linear portion of the curves. As the cell current density approaches the limiting current density, sudden drops in the voltage are observed.

Table 5.1 Theoretical modelling parameters for anion exchange membrane direct ammonia fuel cell

| Parameter | Value | Units |
|---|---|---|
| Cell temperature | 298 | K |
| Cathodic exchange current density | 2.8E-3 | $A/m^2$ |
| Reactant pressures | 101.25 | kPa |
| Limiting current density | 200 | $A/m^2$ |
| Anodic exchange current density | 2.7E-2 | $A/m^2$ |
| Faradays constant | 96485 | C/mol |

The average open circuit voltage obtained experimentally is observed to be 279 mV. In addition, the average short circuit current density is obtained as 220 $A/m^2$ experimentally. The short circuit current obtained from the theoretical model is 215 $A/m^2$. The experimental and theoretical results are in close conjunction as the modelling parameters are chosen according to the actual parameters of the developed fuel cell. The peak power density obtained experimentally is 17.5 $W/m^2$ at a current density of 110 $A/m^2$ and voltage of 159 mV. Furthermore, the theoretical peak power density is obtained as 16.2 $W/m^2$ at a current density of 130 $A/m^2$ and a voltage of 124.7 mV as can be depicted from Fig. 5.3. Three experimental tests are conducted for each set of working conditions. The experiments are repeated three times as it is considered the minimum acceptable number of experiments that need to be repeated in an experimental study to analyse the associated

standard deviations and uncertainties in measurements. The polarization curves as well as the power density vs current density curves for base conditions of humidifier temperature of 25$^{o}$C are depicted in Figures 5.4 and 5.5.

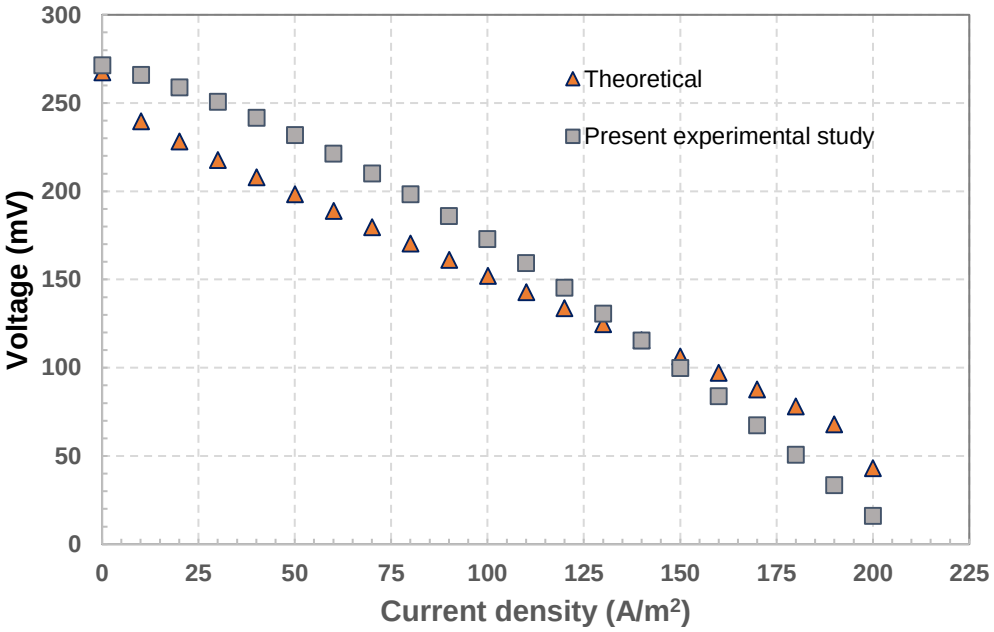


Fig. 5.2 Experimental and theoretical voltage vs current curves

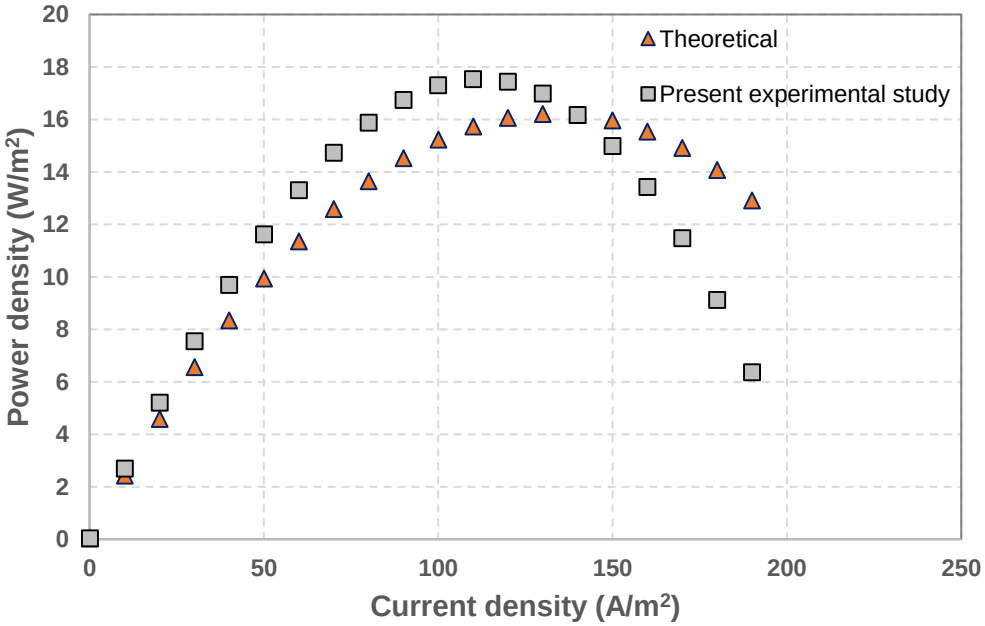


Fig. 5.3 Experimental and theoretical power density vs current density curves

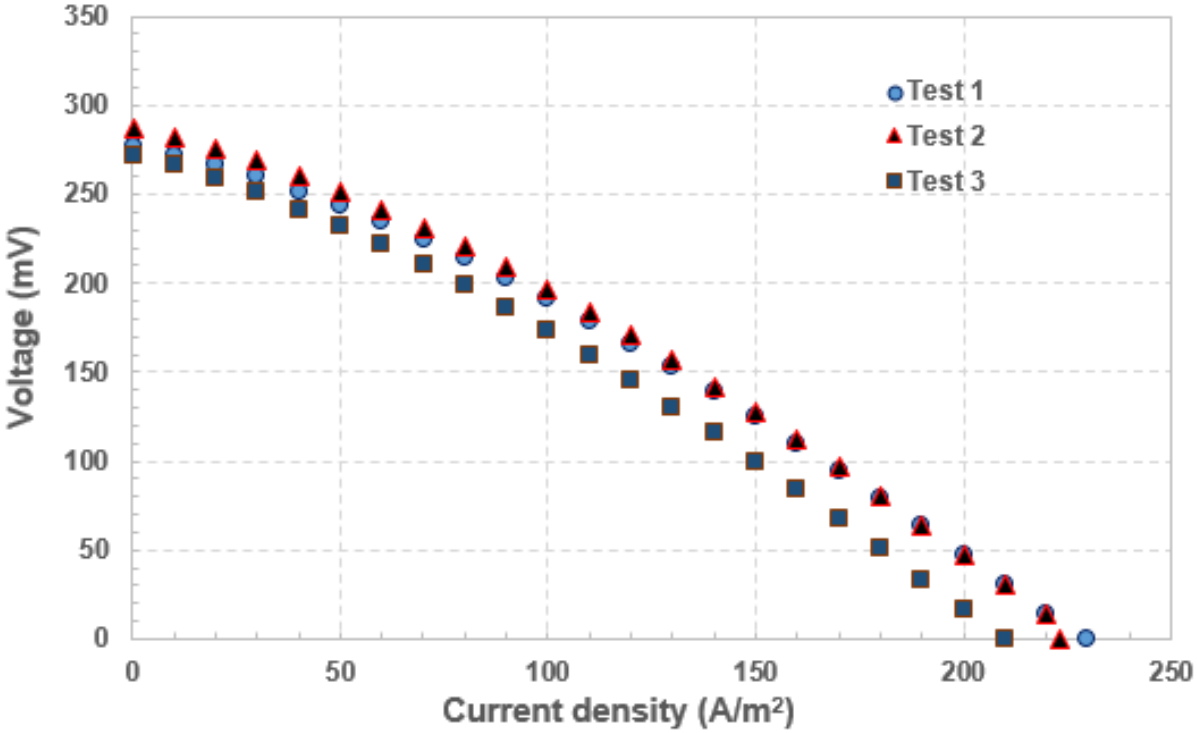


Fig. 5.4 Voltage vs current density curves for a humidifier temperature of 25ºC

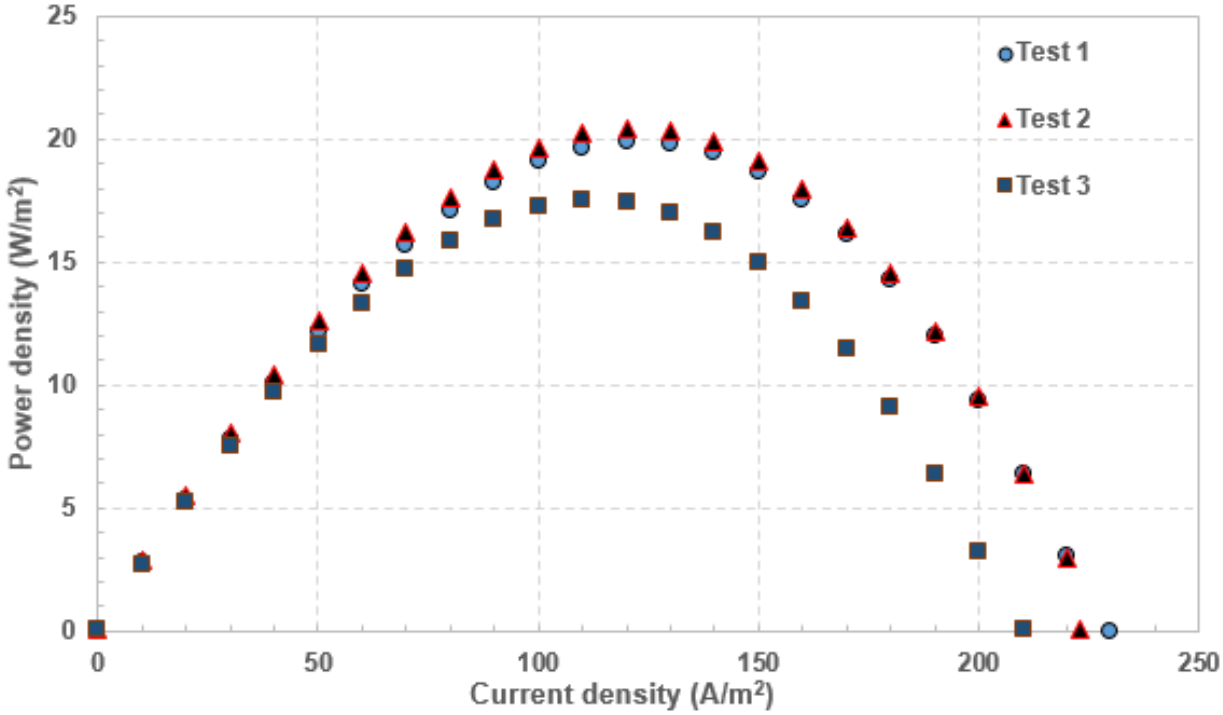


Fig. 5.5 Power density vs current density curves for a humidifier temperature of 25ºC

In the first experimental test at base conditions, an open circuit voltage of 277 mV is obtained. Furthermore, a peak power density of 20 $W/m^2$ is observed at a current density of 120 $A/m^2$. Moreover, the short circuit current density is observed to be 230 $A/m^2$ in the first test. The second experimental test of the fuel cell provided an open circuit voltage of 287 mV and a short circuit current density of 223 $A/m^2$. The peak power density is observed to be 20 $W/m^2$ at a current density of 130 $A/m^2$ and a voltage of 157 mV. The open circuit voltage obtained in the third experimental trial is 272 mV and the short circuit current density observed is 210 $A/m^2$. Furthermore, the peak power density obtained is 17.5 $W/m^2$ at a current density and voltage of 110 $A/m^2$ and 159 mV respectively.

## 5.2 Effects of humidifier temperature on the performance of the single-cell arrangement fuel cell

The performance of the developed fuel cell is tested under varying humidifier temperatures. Increasing the humidifier temperature helps in increasing the rates of reactions within the fuel cell. Specifically, as the cathode side of fuel cell comprises of humidified air input, higher humidifier temperatures aid in accelerating the oxygen reduction reaction at the cathode [100]. In the present study, the humidifier temperature is varied and the performance of the fuel cell is tested for ambient temperature (25$^oC$), 60$^oC$ and 80$^oC$. The voltage and power density vs current density curves at a humidifier temperature of 60$^oC$ are depicted in Fig. 5.6 and 5.7. As can be observed from the polarization curve, the average open circuit voltage is obtained to be 299 mV. This value is marginally higher than the open circuit voltage obtained at 25$^oC$. The rise in open circuit voltage is 7.3%. Furthermore, the short circuit current is not observed to increase significantly. At 25$^oC$, the average short circuit current density is observed to be 221 $A/m^2$ and the average fuel cell short circuit current obtained at 60$^oC$ is nearly 235 $A/m^2$. Moreover, the average peak power density obtained at 60$^oC$ is 20.2 $W/m^2$ at a current density of 150 $A/m^2$ and average voltage of 135.1 mV. The average peak power density is observed to increase by 5.4% as compared to performance at ambient conditions. A humidifier temperature rise from 25$^oC$ to 60$^oC$ is observed to marginally improve the fuel cell performance in terms of open circuit voltage and short circuit current. Furthermore, in order to assess the effect of high humidifier temperatures on the performance, a temperature of 80$^oC$ is also utilized.

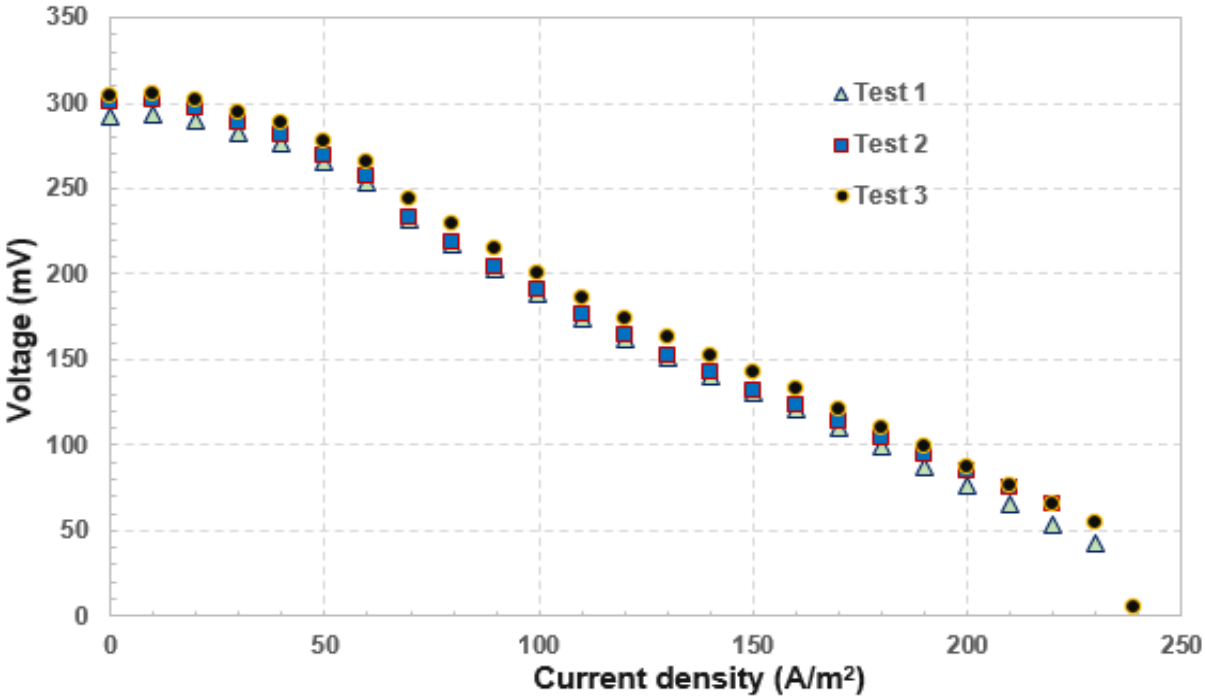


Fig. 5.6 Voltage vs current density curves for a humidifier temperature of 60°C

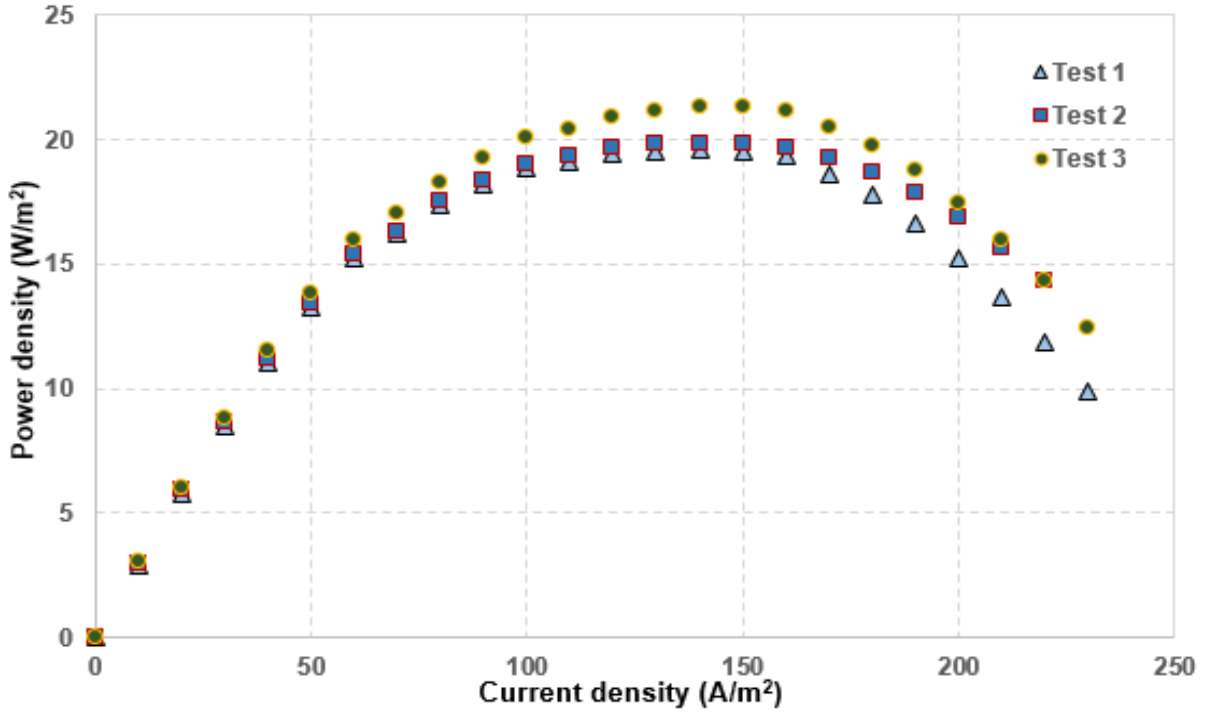


Fig. 5.7 Power density vs current density curves for a humidifier temperature of 60°C

The polarization curves and the power density vs current density curves for a humidifier temperature of 80°C are depicted in Figures 5.8 and 5.9. The open circuit voltage at 80°C is observed to be higher than the voltage values obtained at 60°C and 25°C. The average open circuit voltage is observed to be 335 mV at a humidifier temperature of 80°C. This corresponds to a 20.3% increase as compared to the open circuit voltage at 25°C. In addition, this corresponds to a 12% increase in the voltage as compared to the average value obtained at 60°C. Moreover, the peak power densities obtained at a humidifier temperature of 80°C are observed to be higher than at lower temperatures. The average peak power density obtained at 80°C is 21.2 W/m$^2$, this value is 10.2 % higher than the peak power density obtained at 25°C. In addition, this value is 4.6% higher than the value observed at 60°C. Voltage and current density values of 151.3 mV and 149.9 A/m$^2$ are obtained respectively at the highest peak power density of 22.8 W/m$^2$. Furthermore, the short circuit current densities are also observed to be marginally higher than the values obtained at ambient conditions. Figures 5.10 and 5.11 depict the average voltage and power density vs current density curves for the single-cell arrangement at varying humidifier temperatures. These values correspond to the average values of the three experimental tests conducted.

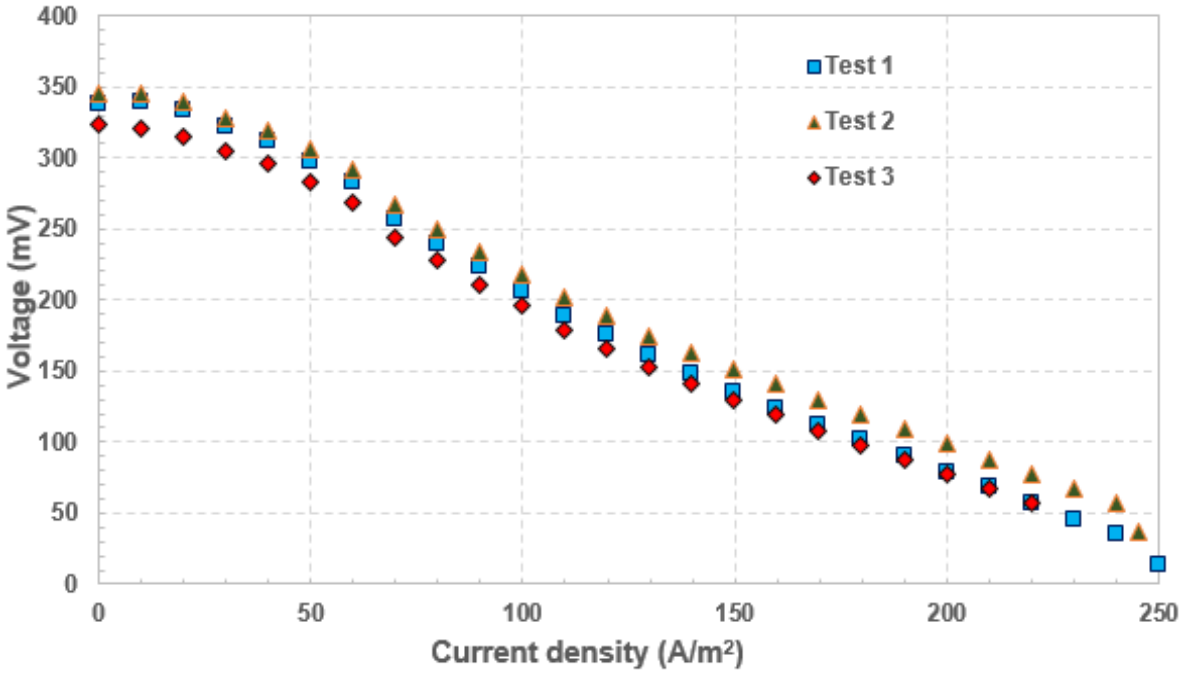


Fig. 5.8 Voltage vs current density curves for a humidifier temperature of 80°C

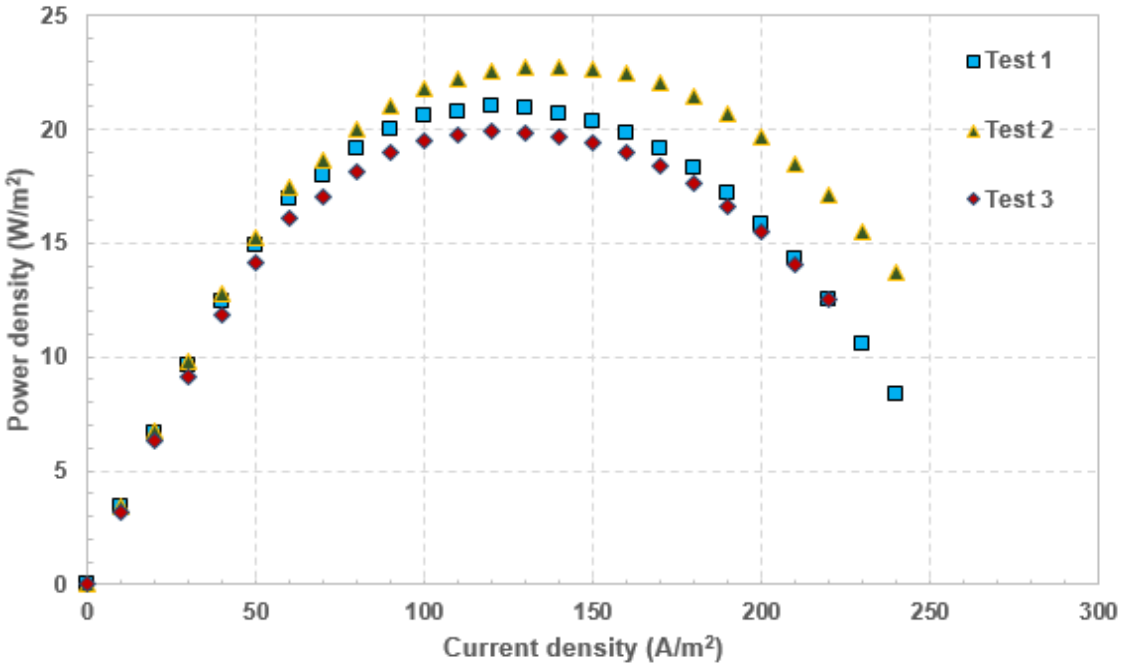


Fig. 5.9 Power density vs current density curves for a humidifier temperature of 80°C

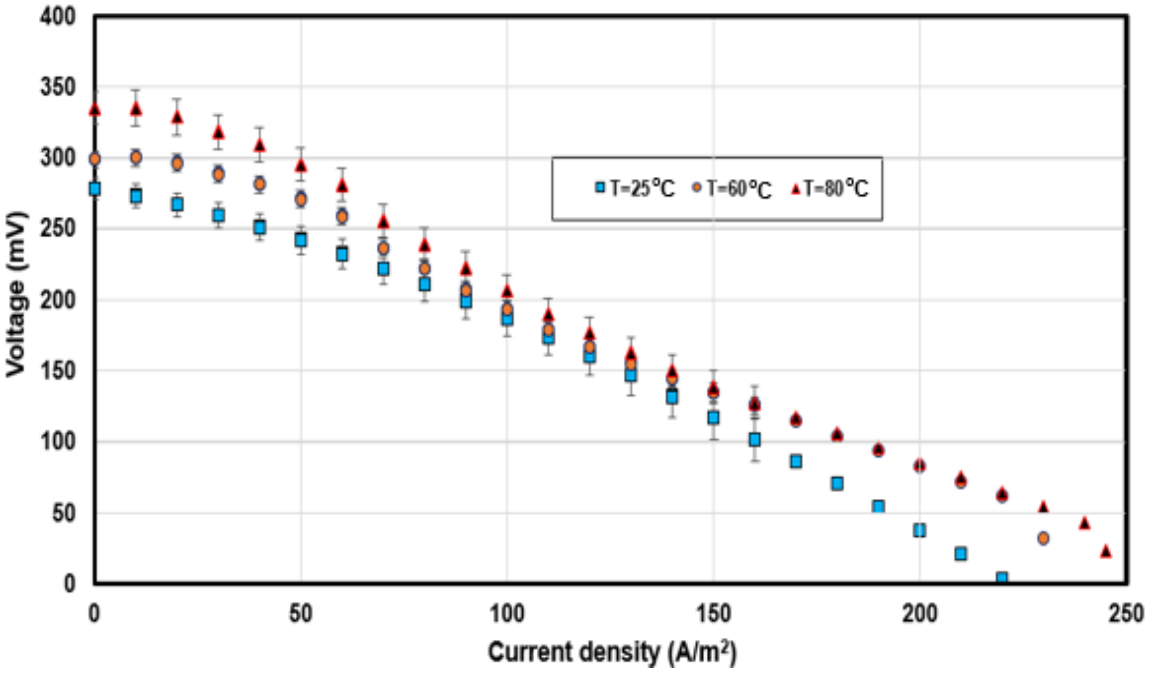


Fig. 5.10 Average voltage vs current density curves for varying humidifier temperatures

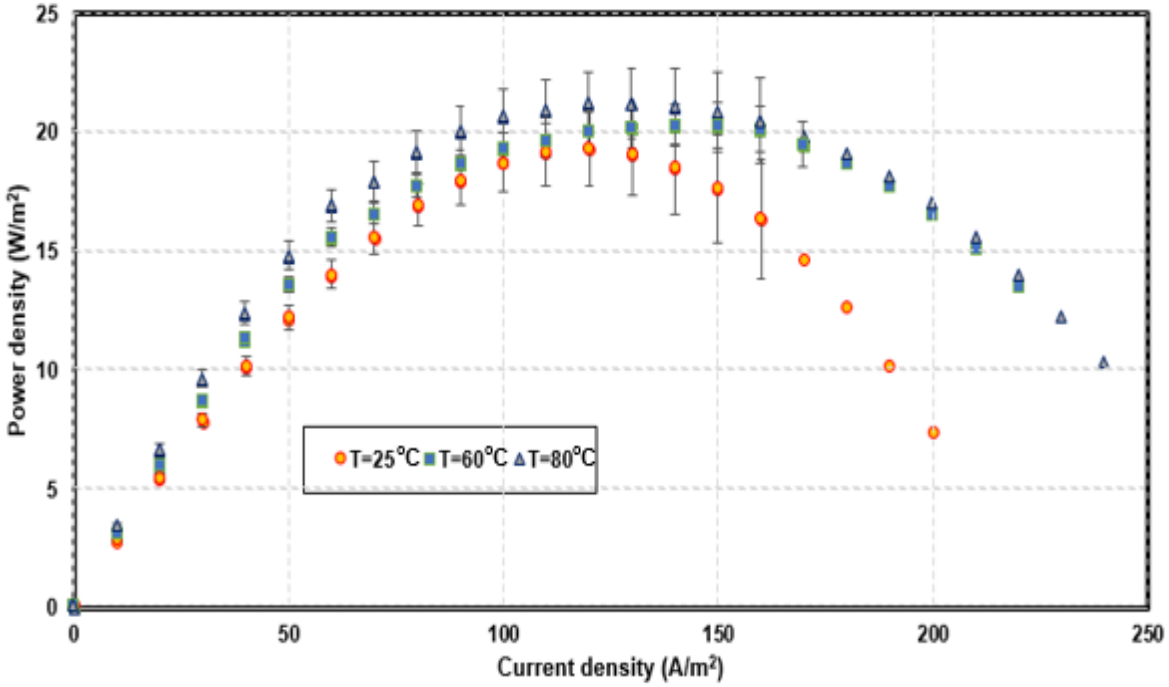


Fig. 5.11 Average power density vs current density curves for varying humidifier temperatures

### 5.3 Performance results of anion exchange membrane direct ammonia fuel cell with aqueous ammonia as fuel

The performance of the anion exchange membrane direct ammonia fuel cell is also tested with aqueous ammonia as the fuel. Ammonia gas is highly soluble in water. A solution of aqueous ammonia is formed by dissolving gaseous ammonia in water. The solution comprises of gaseous $NH_3$ molecules dissolved in water. In addition, a small percentage of ammonium hydroxide ($NH_4OH$) molecules may also be found. In the present study, aqueous ammonia of concentration 1 M is utilized. The polarization curves as well as the power density vs current density curves at ambient solution temperature of 25$^o$C are depicted in Figures 5.12 and 5.13. The average open circuit voltage is observed to be 110.2 mV. This value is significantly lower than the open circuit voltage obtained with gaseous ammonia as the fuel. This can be attributed to the high concentration of ammonia in the experiments conducted with gaseous ammonia, as the gaseous input comprised of nearly pure ammonia gas. However, the number of ammonia molecules in the aqueous solution are considerably lower than in the case of pure ammonia. Hence, lower fuel cell performance is expected. At ambient temperature of 25$^o$C, the peak power density is

obtained as 2.2 W/m$^2$. The corresponding average voltage and current density values are 71.9 mV and 30 A/m$^2$ respectively. In addition, the short circuit current density is also observed to decrease significantly. This can be attributed to higher activation, Ohmic and concentration polarization losses with the aqueous state of input fuel. The average short circuit current density is observed to be around 62 A/m$^2$. Furthermore, the performance of the single cell arrangement anion exchange membrane direct ammonia fuel cell is also investigated under varying temperatures of aqueous ammonia fuel. The polarization curves and the power density vs current density curves for the solution temperature of 45$^o$C are depicted in Figures 5.14 and 5.15. The average open circuit voltage obtained is 130.1 mV. An increase in fuel cell performance is observed as the temperature increased to 45$^o$C. An increase of 18% is observed in the open circuit voltage value as the temperature is increased from 25$^o$C to 45$^o$C. This is attributed to higher molecular activity and diffusion coefficients at higher operating temperatures. These allow higher number of molecules to react at higher reaction rates. The average peak power density obtained is 3.9 W/m$^2$. This corresponds to a significant increase of 77% as compared to ambient temperature conditions.

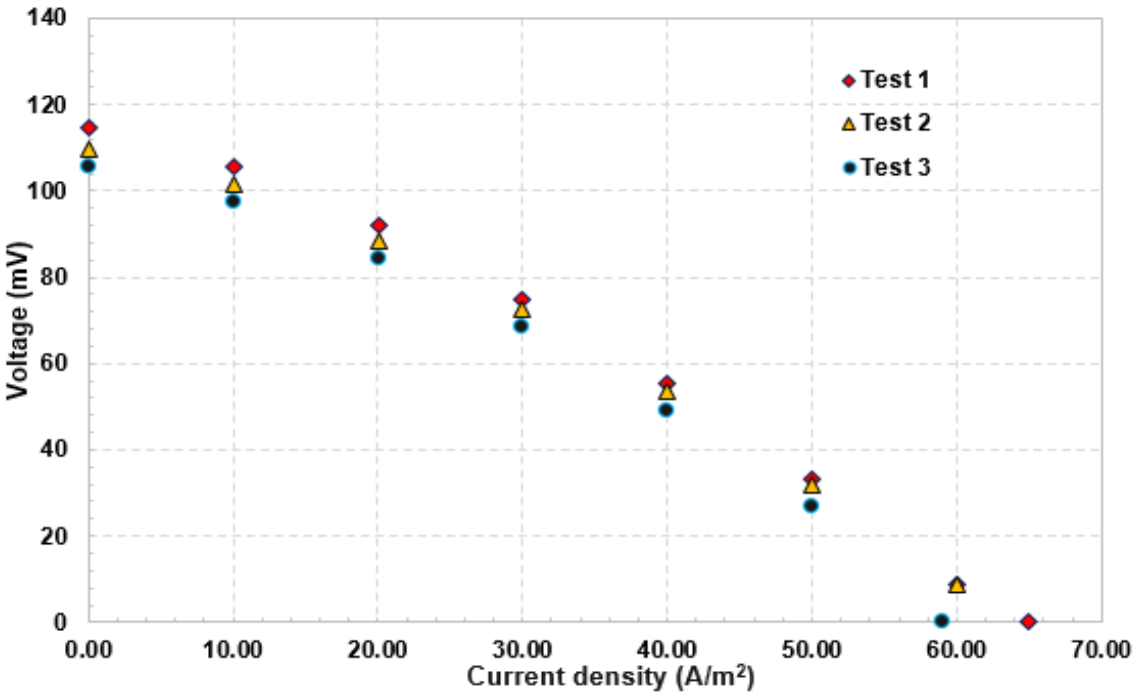


Fig. 5.12 Voltage vs current density curves for aqueous ammonia at 25$^o$C

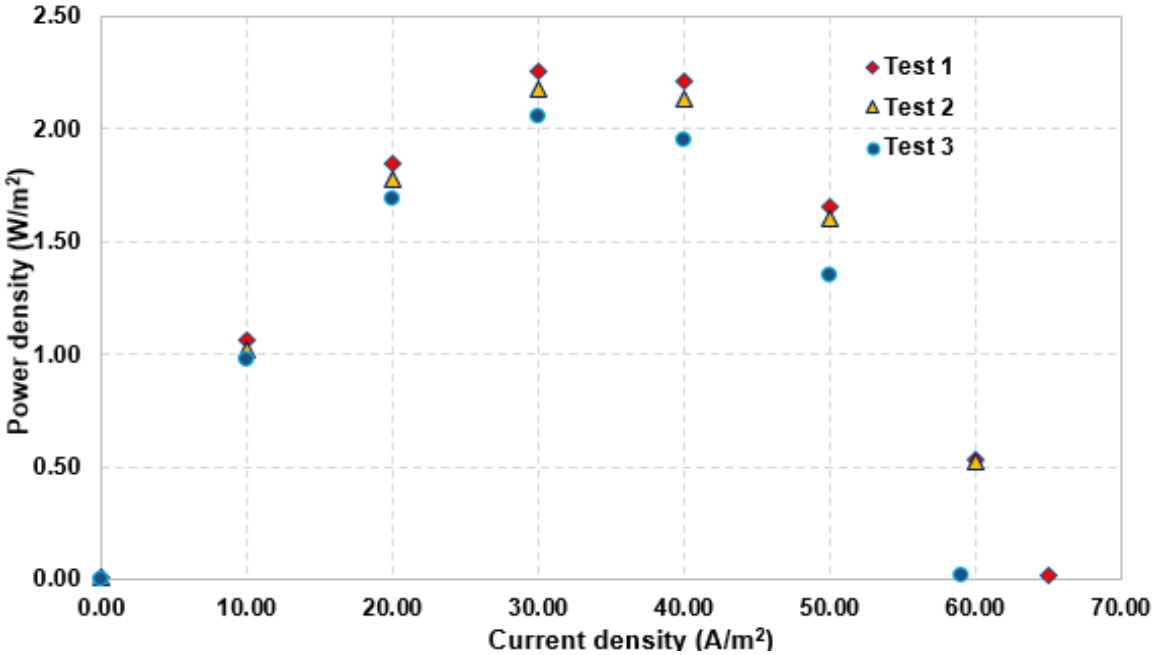


Fig. 5.13 Power density vs current density curves for aqueous ammonia at 25°C

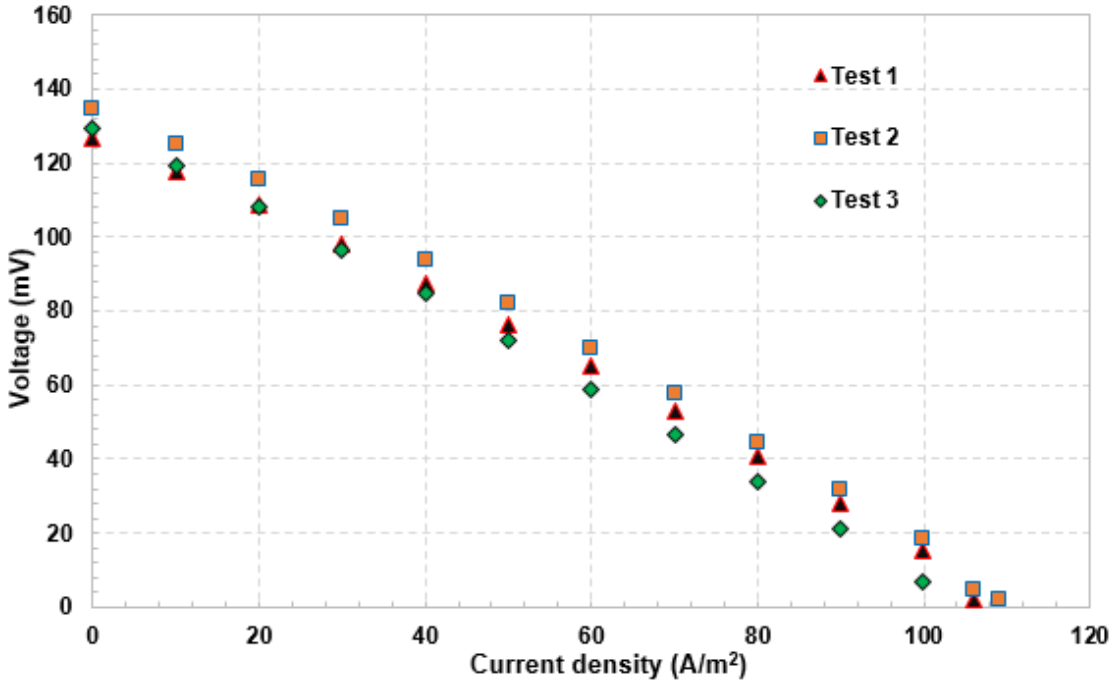


Fig. 5.14 Voltage vs current density curves for aqueous ammonia at 45°C

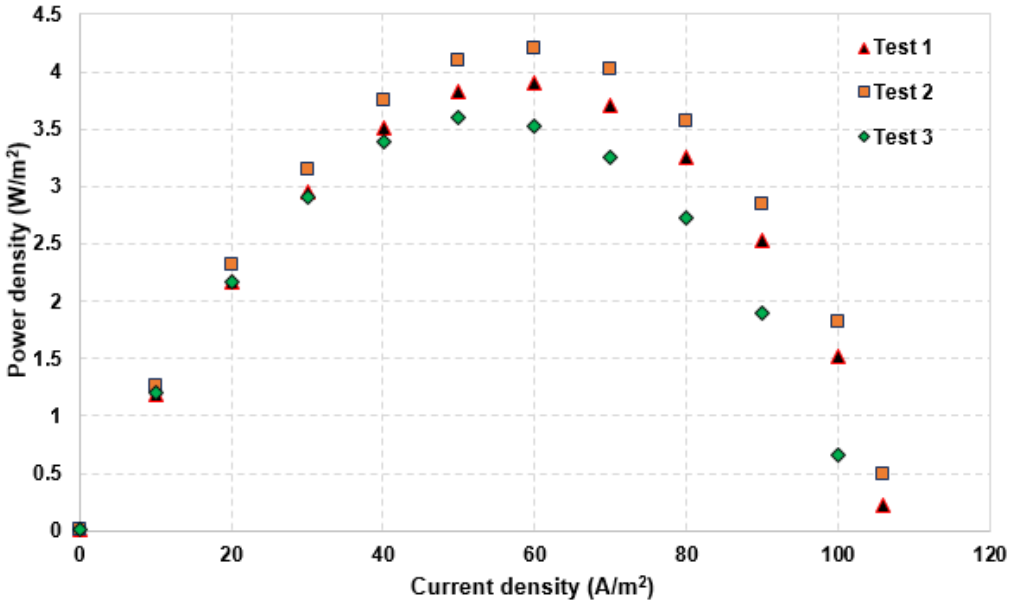


Fig. 5.15 Power density vs current density curves for aqueous ammonia at 45°C

The average voltage and current density values corresponding to the peak power density are 69 mV and 60 A/m$^2$ respectively. Moreover, the short circuit current density values are also observed to increase considerably. The average short circuit density is observed to be 106 A/m$^2$ at a solution temperature of 45°C. This value is significantly higher than the short circuit current density obtained at ambient temperature. This rise can be attributed to the decrease in the polarization losses due to temperature rise of the solution. Furthermore, the fuel cell performance in the single cell arrangement is also investigated with aqueous ammonia at 65°C. The fuel cell performance is observed to improve with increasing solution temperatures. The average open circuit voltage obtained at 65°C is 147.1 mV. This corresponds to a 33.5% increase as compared to the open circuit voltage obtained at 25°C. Furthermore, the average peak power density is observed to be 6.1 W/m$^2$. This signifies a 55% increase as compared to a solution temperature of 45°C. An average voltage of 84 mV and a current density of 73 A/m$^2$ is obtained at the peak power density. Moreover, the short circuit current density is also observed to increase at a higher temperature. The average short circuit current density is observed to be 140 A/m$^2$ as can be depicted from Fig. 5.16. The rise in short circuit current density at a solution temperature of 65°C is observed to be 32.1% as compared to a temperature of 45°C. The increase in short circuit current densities with an increase in solution temperatures can be attributed to lower polarization losses. At higher temperatures, molecular activities are

accelerated. Further, the diffusion coefficients are also enhanced at higher operating temperatures. Moreover, the rate of ammonia evaporation from the ammonia solution also increases with rising temperature. Hence, this allows more efficient diffusion of ammonia molecules that provides higher number of reaction sites as well as higher electrochemical reaction rates. Figures 5.18 and 5.19 show the average voltage vs current density polarization curves and the average power density vs current density curves when aqueous ammonia is utilized as fuel. These values correspond to the average values of the three experimental tests conducted.

### 5.4 Performance results of a five-cell anion exchange membrane direct ammonia fuel cell stack

A five-cell anion exchange membrane direct ammonia fuel cell stack is developed and investigated at varying humidifier temperatures. The polarization curves as well as the power density vs current density curves at a humidifier temperature of 25°C are depicted in Figures 5.20 and 5.21. The average open circuit voltage for the five-cell stack is observed to be 1185.3 mV. Furthermore, the average peak power density is observed to be 35.9 W/m$^2$ as can be depicted from Fig. 5.17. The average voltage value observed at the peak power density is 511 mV and the current density is observed to be around 70 A/m$^2$.

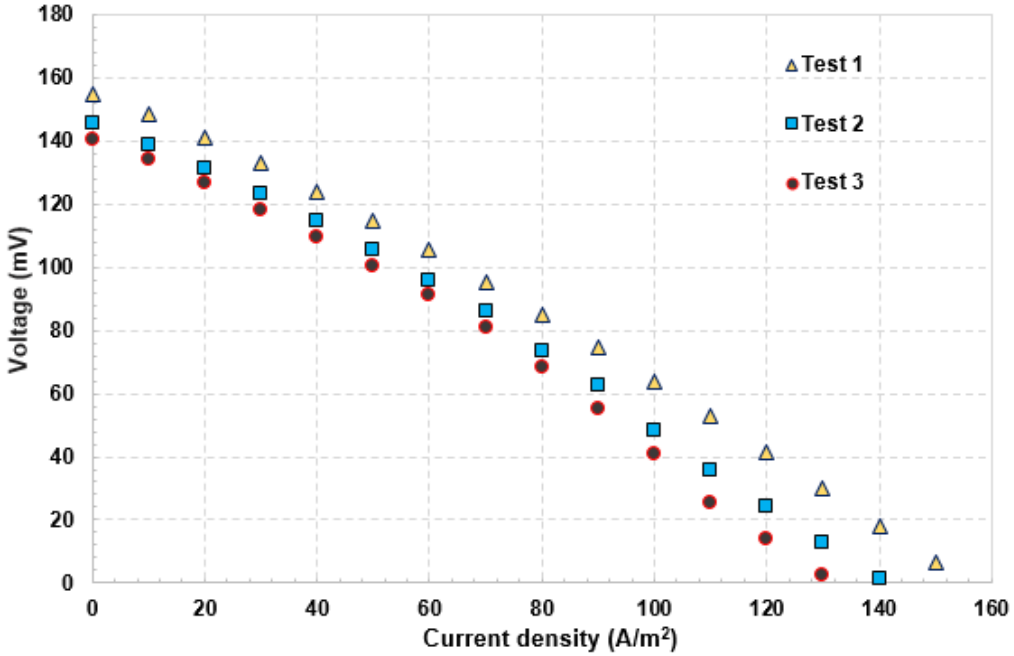


Fig. 5.16 Voltage vs current density curves for aqueous ammonia at 65°C

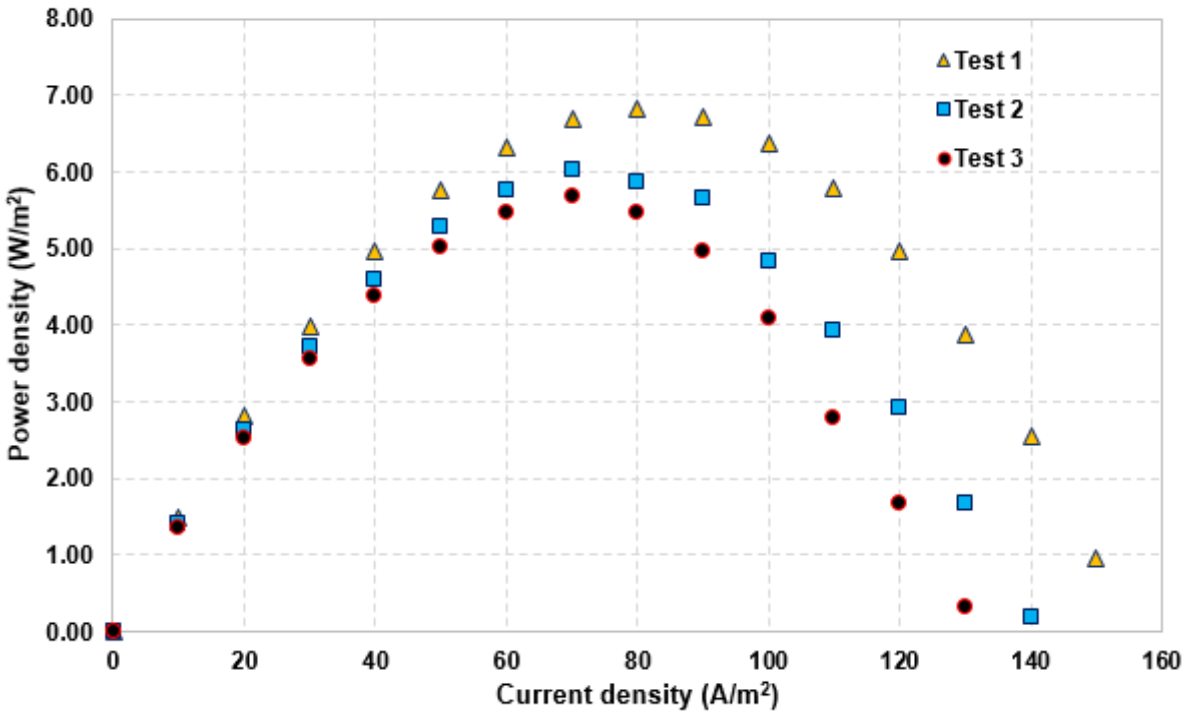


Fig. 5.17 Power density vs current density curves for aqueous ammonia at 65°C

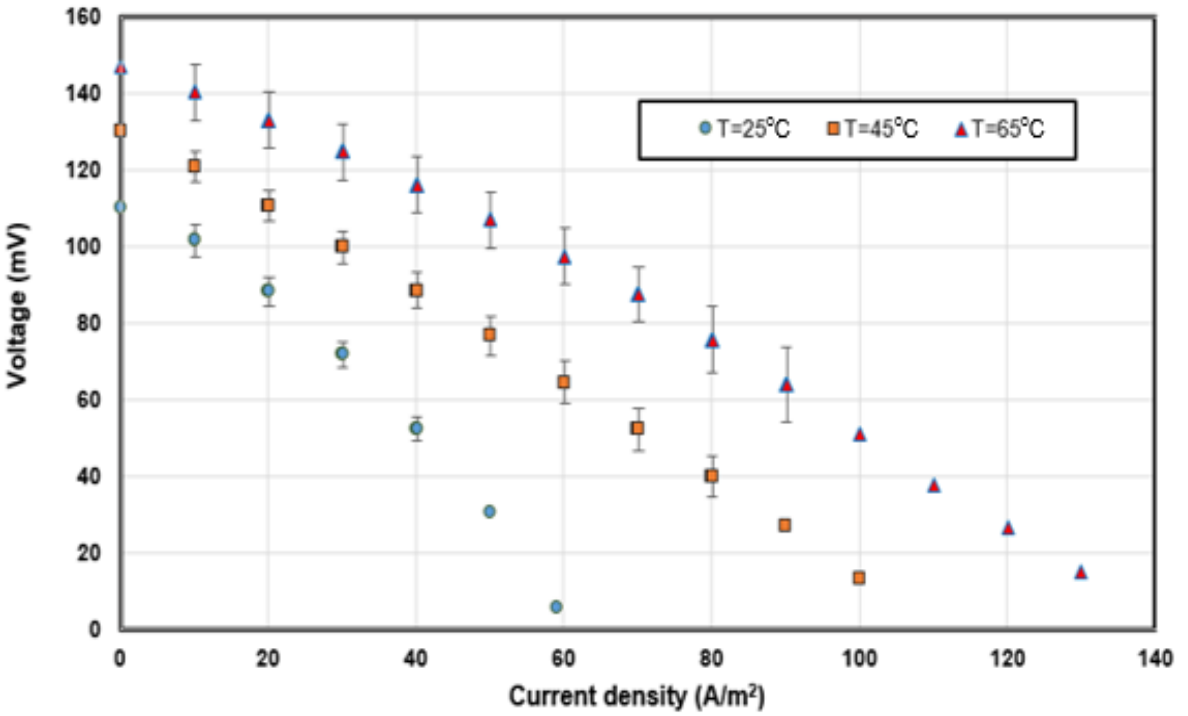


Fig. 5.18 Average voltage vs current density curves for varying solution temperatures

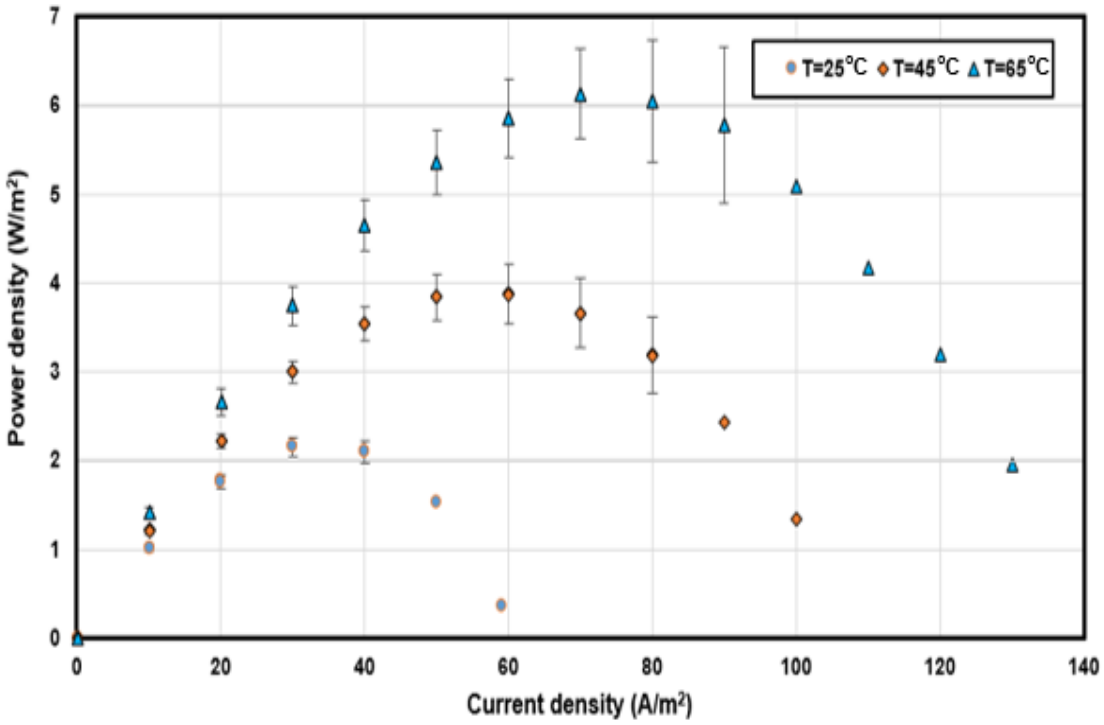


Fig. 5.19 Average power density vs current density curves for varying solution temperatures

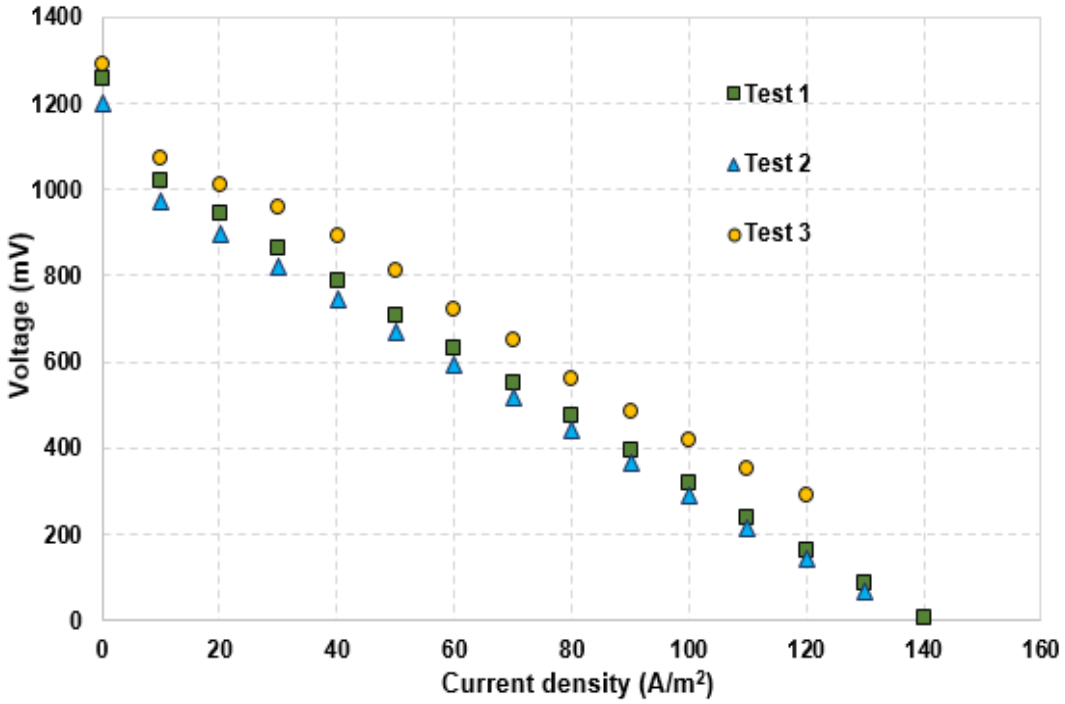


Fig. 5.20 Voltage vs current density curves for a five-cell stack and humidifier temperature of 25°C

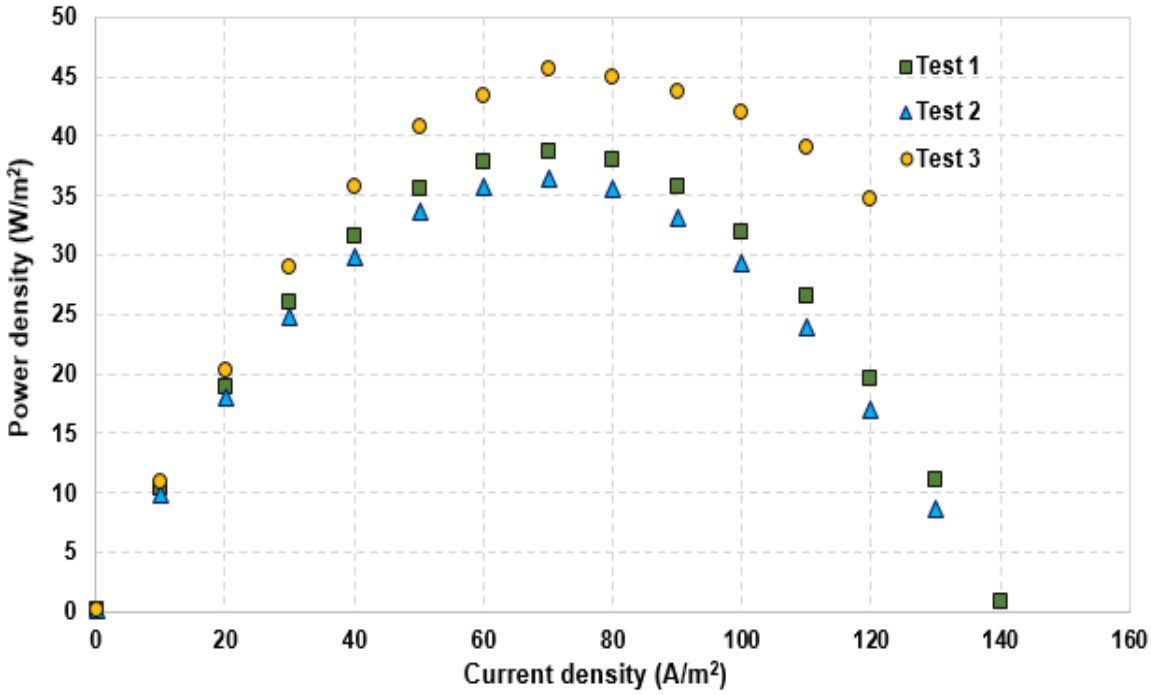


Fig. 5.21 Power density vs current density curves for a five-cell stack and humidifier temperature of 25ºC

The average short circuit current density is observed to be 133 A/m$^2$. As compared to the single cell arrangement, the peak power density of a five-cell stack is observed to be nearly 2 times higher. However, the current density at peak power density is observed to be 125 A/m$^2$ for the single cell arrangement and 70 A/m$^2$ for the five-cell stack arrangement. Hence, this infers presence of higher polarization losses in the five-cell stack. Specifically, the Ohmic losses may increase considerably due to the presence of five anion exchange membranes. Thus, as the fuel cell current density increases, the Ohmic losses cause a higher voltage drop than in the case of the single cell arrangement.

### 5.5 Effects of humidifier temperature on the performance of five-cell fuel cell stack

The performance of the five-cell anion exchange membrane direct ammonia fuel cell stack is investigated at varying humidifier temperatures. Temperatures chosen for the humidifier are kept same as in the case of single cell arrangement. The polarization curves as well as the power density vs current density curves obtained at a humidifier temperature of 60ºC are depicted in Figures 5.22 and 5.23. The average open circuit voltage is observed to be 1398.7 mV. This corresponds to 18% increase in open circuit voltage as compared to the results obtained at a humidifier temperature of 25ºC. Furthermore, the average peak power

density is obtained to be 43.3 W/m$^2$. An increase of 20.8% is observed in the peak power density. The average voltage value at the peak power density is obtained as 650.8 mV. Moreover, the average current density is observed to be 66.7 A/m$^2$ at the peak power density. In addition, the average short circuit current density is observed to be 144 A/m$^2$ at a humidifier temperature of 60$^o$C. The stack performance is also tested at a humidifier temperature of 80$^o$C as shown in Figures 5.24 and 5.25. The average open circuit voltage iss observed to be 1582 mV. In addition, the average peak power density is observed to be 51.1 W/m$^2$. This corresponds to a 15.2 W/m$^2$ rise in the average peak power density as compared to ambient humidifier temperature. The average voltage and current density obtained at this power density is observed to be 730 mV and 70 A/m$^2$ respectively. Moreover, the average short circuit current density recorded during the experiments is 146.7 A/m$^2$. This signifies an increase of nearly 2.7 A/m$^2$ as compared to the short circuit current density at 60$^o$C. As compared to the short circuit current density at an ambient humidifier temperature of 25$^o$C, an increase of 13.7 A/m$^2$ is observed in the short circuit density at a humidifier temperature of 80$^o$C. This can also be attributed to lower polarization losses as the humidifier temperature is increased to 80$^o$C.

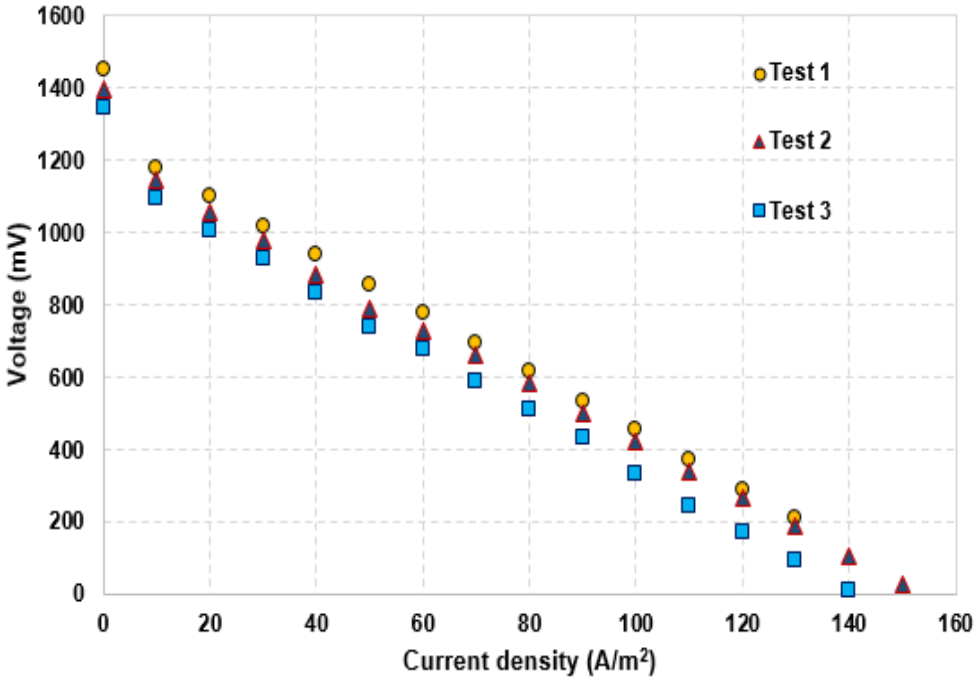


Fig. 5.22 Voltage vs current density curves for a five-cell stack and humidifier temperature of 60$^o$C

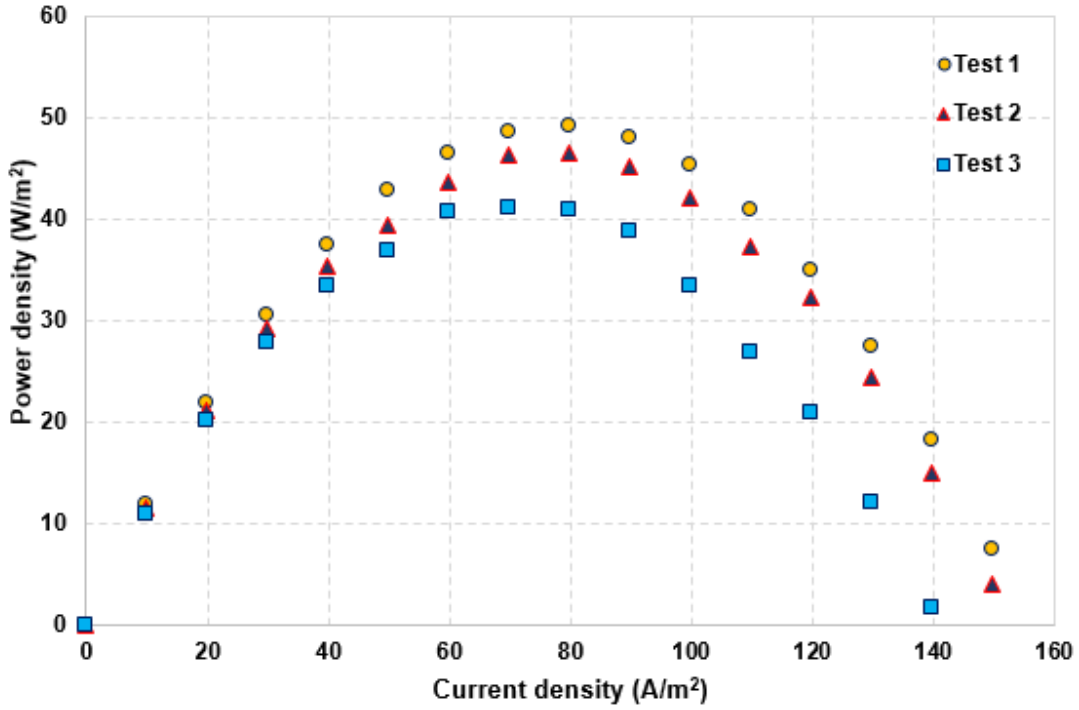


Fig. 5.23 Power density vs current density curves for a five-cell stack and humidifier temperature of 60°C

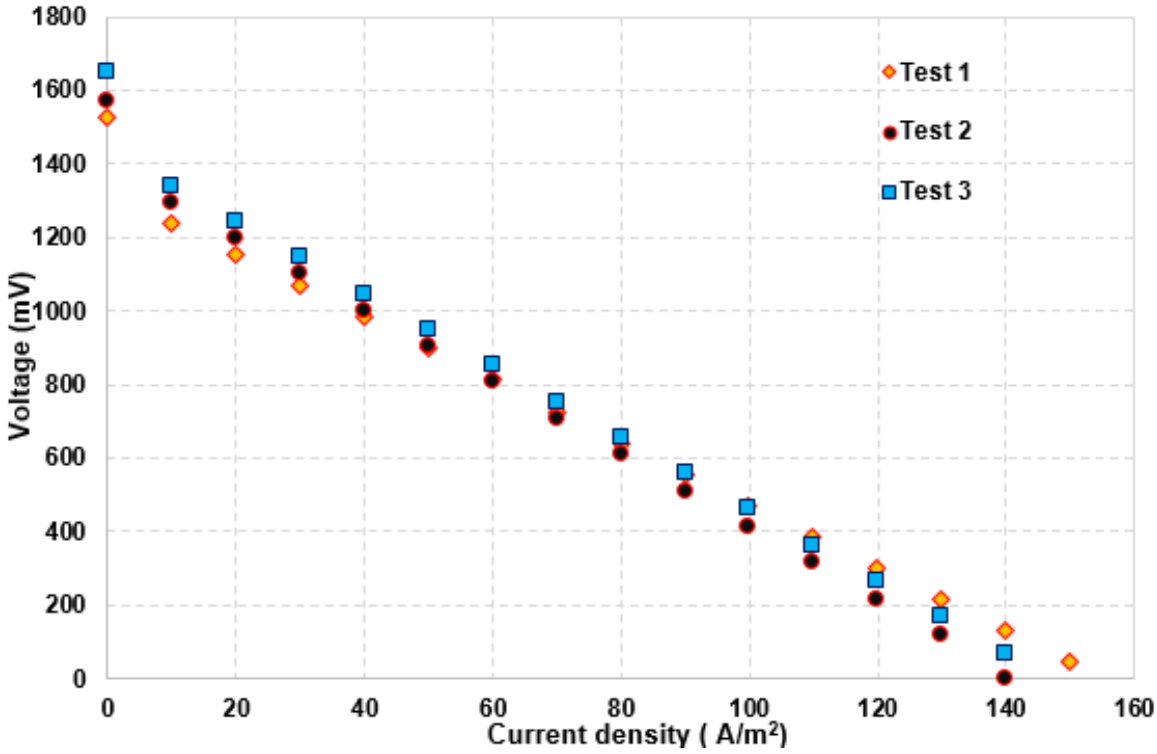


Fig. 5.24 Voltage vs current density curves for a five-cell stack and humidifier temperature of 80°C

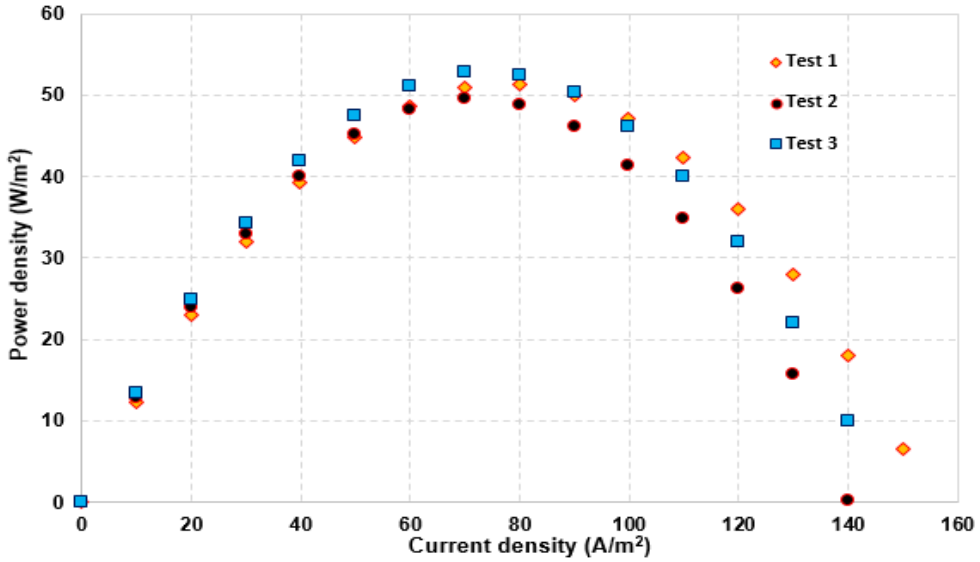


Fig. 5.25 Power density vs current density curves for a five-cell stack and humidifier temperature of 80°C

Figures 5.26 and 5.27 show the average five-cell stack voltage vs current density polarization curves and the average power density vs current density curves for varying humidifier temperatures. These open circuit voltage and power density values correspond to the average values of the three experimental tests performed.

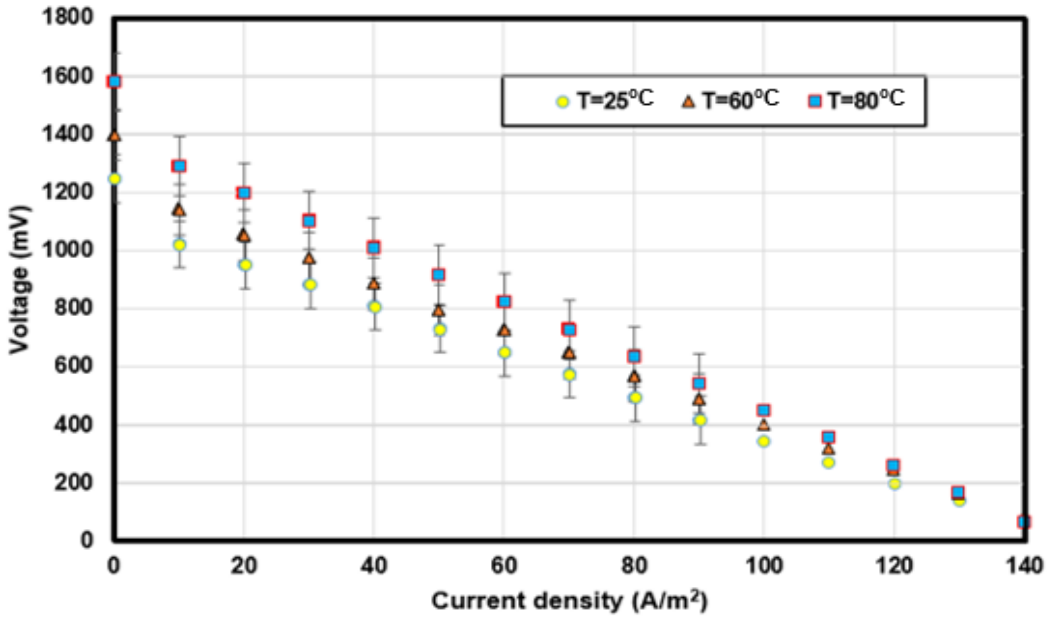


Fig. 5.26 Average voltage vs current density curves for five-cell stack for varying humidifier temperatures.

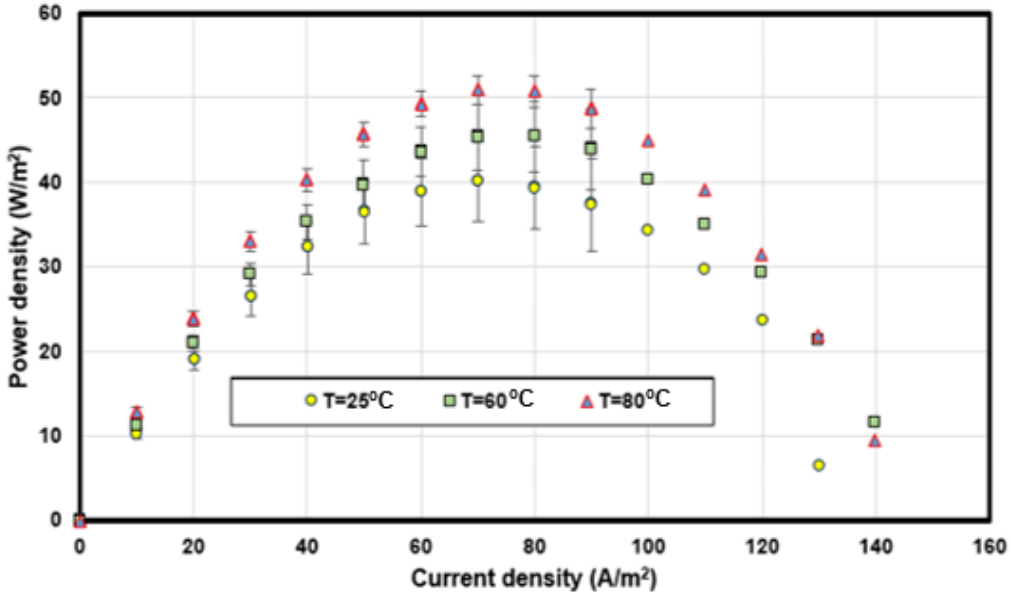


Fig. 5.27 Average power density vs current density curves for five-cell stack for varying humidifier temperatures

The obtained results indicate that higher humidifier temperatures enhance the fuel cell performances. The open circuit voltage is observed to increase by 20.3% as the humidifier temperature is increased from 25°C to 80°C. Furthermore, an 18% increase in open circuit voltage is observed for the five-cell stack as the same temperature rise is applied. However, attaining 80°C of humidifier temperature will require additional heat input to the overall system. Hence, lowering the overall efficiencies of the system. Thus, waste heat sources can be utilized to heat the humidifier to higher temperatures. Moreover, renewable sources of energy can be used to heat the humidifier to the required temperature. In the case of aqueous fuel, higher solution temperatures are found to enhance the fuel cell performance significantly. The peak power density is observed to increase by nearly 3 times as the aqueous fuel temperature is increased from 25°C to 65°C. Therefore, it is suggested to use higher solution temperatures in case of utilizing aqueous ammonia fuel. However, at temperatures above 65°C, the rate of ammonia evaporation from water increases considerably making it difficult to be used as fuel in the aqueous form. Hence, temperatures below 65°C are suggested in case of aqueous ammonia fuel. Nevertheless, if waste heat is available to be used for heating the aqueous ammonia solution, a system that stores unreacted ammonia gaseous fuel in water and discharges it when required by utilizing waste heat can be developed.

### 5.6 Performance comparison with literature studies

The benchmarking of the developed fuel cell is performed by comparing with recently conducted studies. A comparison of the open circuit voltage obtained for the single-cell arrangement direct ammonia fuel cell in the present study and other recent studies is depicted in Fig. 5.28. As can be observed from the figure, the direct ammonia fuel cell developed by Lan and Tao [78] had a combatively higher open circuit voltage. This can be attributed to the low membrane thickness utilized in their study. Furthermore, Suzuki et al. [79] also reported higher open circuit voltages that are expected to be due to their lower membrane thickness as compared to the present study. In anion exchange membrane based fuel cells, lower membrane thickness allows faster ionic transfer leading to better performances. In addition, lower membrane thicknesses lead to lower polarization losses in the fuel cell. This can be observed in Figures 5.29 and 5.30. Figure 5.29 depicts the fuel cell voltage at a current density of 100 A/m$^2$. The higher voltage obtained by Lan and Tao [78] at this current density is attributed to lower polarization losses owing to lower membrane thickness. Furthermore, as can be observed from Figure 5.30, the power density obtained at this current density is also higher due to the higher voltage. Hence, in order to enhance the performance of the fuel cell developed in the current study, lower thickness membranes are recommended.

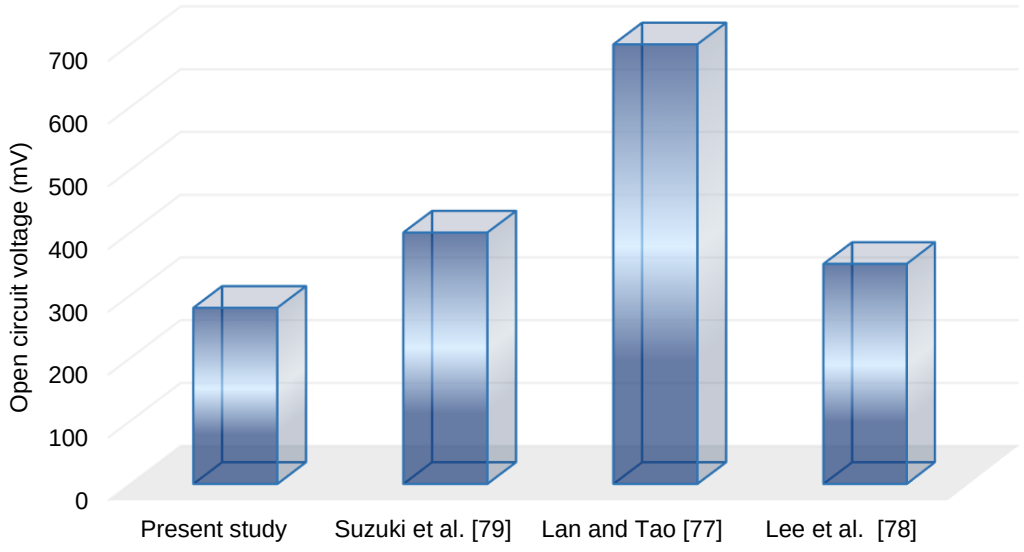


Fig. 5.28 A comparison of open circuit voltage obtained for the anion exchange membrane direct ammonia fuel cell in the current study with other previous studies

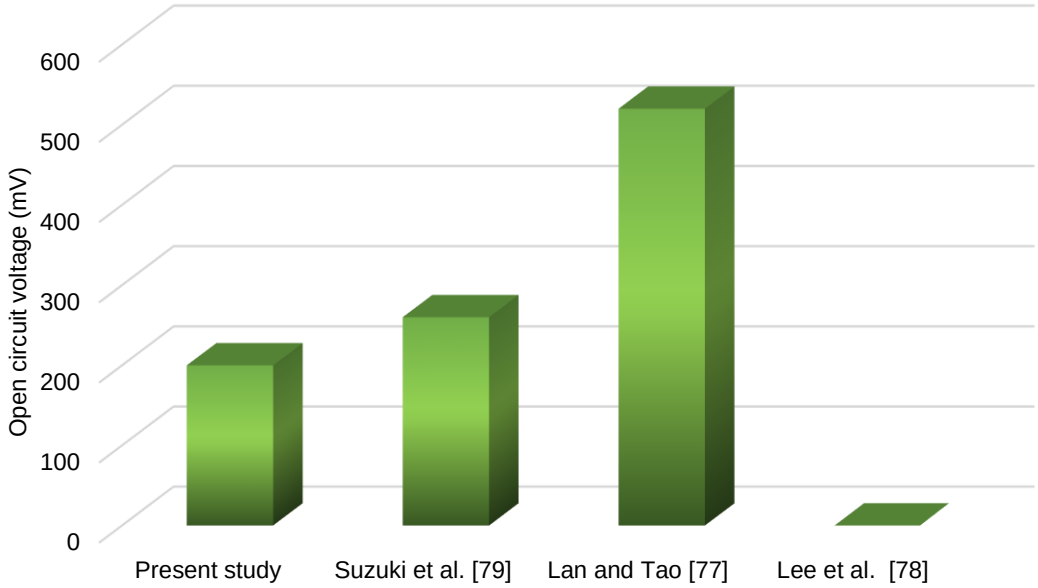


Fig. 5.29 A benchmarking of open circuit voltage at 100 A/m$^2$ current density obtained for the single cell anion exchange membrane direct ammonia fuel cell

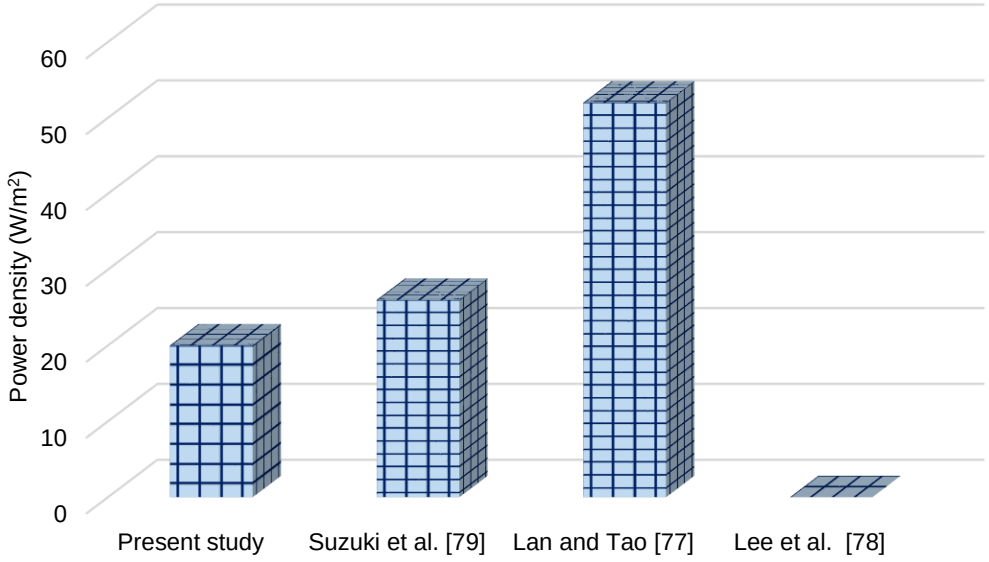


Fig. 5.30 A benchmarking of power density at 100 A/m$^2$ current density obtained for the single cell anion exchange membrane direct ammonia fuel cell

### 5.7 Electrochemical impedance spectroscopy results

Electrochemical impedance spectroscopy results are characterized through Nyquist and Bode plots. The Nyquist plot comprises of the impedance results with the y-axis showing the imaginary axis and the x-axis displaying the real axis at varying frequencies. The Bode

plot provides information about the resultant impedances with magnitudes displayed on the primary y-axis and the phase angles displayed on the secondary y-axis respectively. The x-axis contains the frequency values. The equivalent fuel circuit utilized in the present study is depicted in Fig.4.1. A detailed discussion on the modelling and analyses utilized in the present study to determine the electrochemical impedance parameters is described in the corresponding section. The Bode plots obtained are shown in Fig. 5.28 and 5.30. As can be depicted from the figure, the modelling and experimental results are in close conjunction. The frequency is varied from $10^5$ Hz to 0.1 Hz, the impedance magnitude is observed to increase considerably with decreasing frequency. The Nyquist plot is depicted in Figures 5.32. As can be observed from the figure, the experimental and modelling results fall in close conjunction. The results of the electrochemical impedance parameters described in chapter 4.2 are given in Table 5.2. The anodic resistance (Rf-anode) is obtained 13.26 Ohms and the cathodic resistance (Rf-cathode) is obtained as 23.53 Ohms. This resistance includes charge transfer as well as mass transfer resistances at the anode and cathode respectively. Furthermore, the high frequency resistance (HFR) is obtained as 2.97 Ohms. The HFR represents the total Ohmic resistances of the cell [88]. Moreover, in order to find the constant phase elements at the cathode and anode, the parameters Yo and a are required as depicted in equation (4.21). The obtained values for these parameters are listed in Table 5.2 for both electrodes. In addition, the inductance ($L_{stray}$) of the cell is obtained as 1.22 E-6 H.

Table 5.2 Results of electrochemical impedance spectroscopy

| **Parameter** | **Value** |
|---|---|
| HFR (Ohms) | 2.97 |
| Yo-cathode (S $s^a$) | 32.71 E-3 |
| Rf-cathode (Ohms) | 23.53 |
| a-cathode | 0.299 |
| Rf-anode (Ohms) | 13.26 |
| Yo-anode (S $s^a$) | 0.06 |
| a-anode | 0.795 |
| $L_{stray}$ (H) | 1.22E-6 |

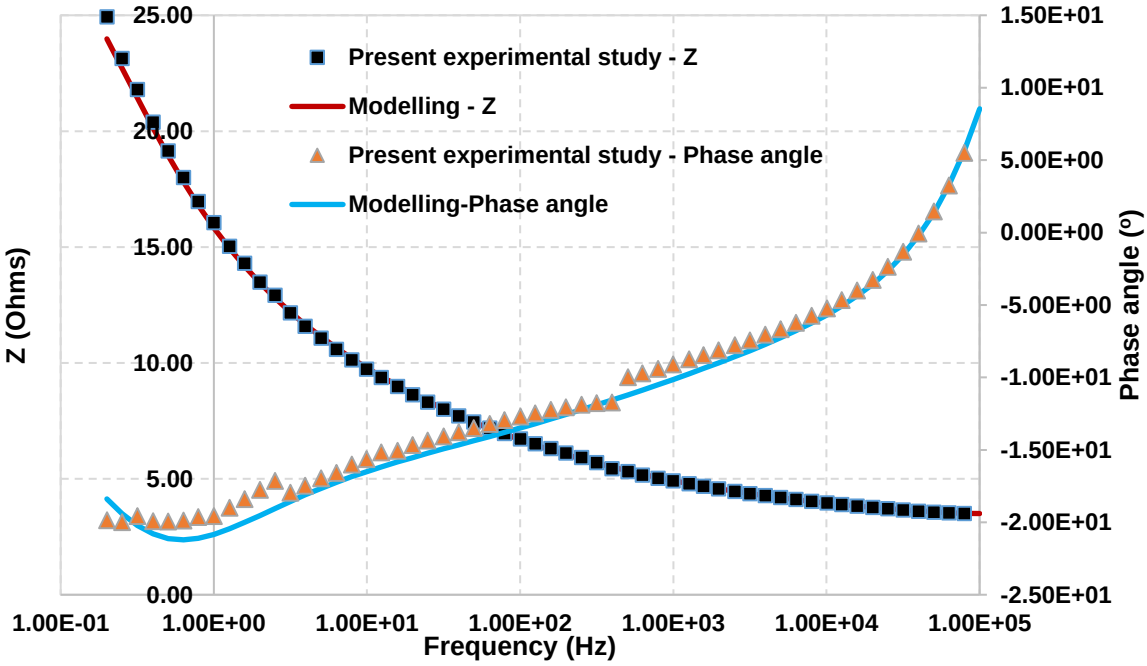


Fig. 5.31 Bode plot obtained from electrochemical impedance spectroscopy

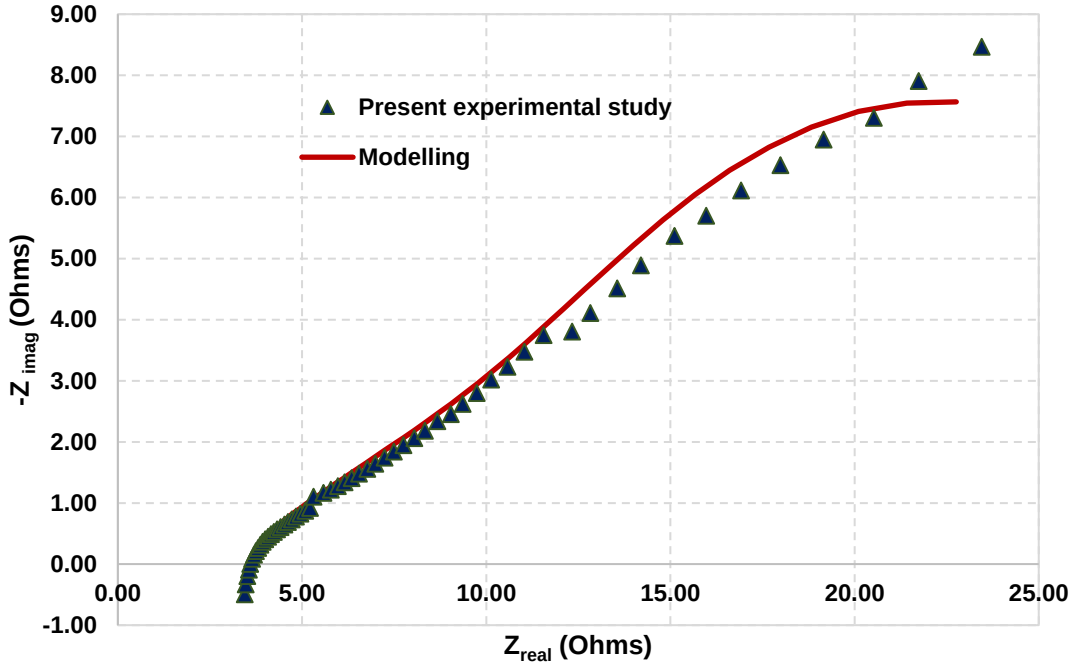


Fig. 5.32 Nyquist plot obtained from electrochemical impedance spectroscopy

### 5.7 Molten alkaline electrolyte based direct ammonia fuel cell results

The results obtained for the molten alkaline electrolyte based direct ammonia fuel cell are depicted in Figures 5.33 and 5.34. At an operating temperature of 220$^{o}$C, the open circuit voltage is observed to be 520±26 mV. Furthermore, the peak power density at this electrolyte temperature is found to be 2.1±0.1 W/m$^2$. In addition, higher electrolyte temperatures are also tested. The open circuit voltages are observed to be 484±24 mV and 388±19 mV for electrolyte temperatures of 250$^{o}$C and 280$^{o}$C respectively. The peak power densities are found to be 2.1±0.1 W/m$^2$ and 2.3±0.1 W/m$^2$ respectively for electrolyte temperatures of 250$^{o}$C and 280$^{o}$C. The open circuit voltages are observed to decrease with increasing electrolyte temperatures. However, the short circuit current densities are observed to increase with increasing temperatures. The increase in the short circuit current densities with rising electrolyte temperatures can be attributed to the increase in the conductivity of electrolyte with rising temperatures. The molten alkaline electrolyte conductivity increases as the temperature is increased. Hence, at higher conductivities the Ohmic losses tend to decrease, reducing the Ohmic polarization losses. Furthermore, the rate of ionic transport within the electrolyte increases as the temperature is increased. Thus, at higher electrolyte temperatures, considerably higher short circuit current densities are obtained. Figure 5.35 depicts a comparison of the energy and exergy efficiencies of the molten alkaline electrolyte based direct ammonia fuel cell at varying temperatures. The energy efficiency of the fuel cell is obtained as 24.9±1.3% at an electrolyte temperature of 220$^{o}$C. However, the energy efficiency is observed to decrease with increasing temperature. At the electrolyte temperatures of 250$^{o}$C and 280$^{o}$C, the energy efficiencies are evaluated as 22.2±1.2% and 18.1±0.9% respectively. Furthermore, the exergy efficiency is calculated to be 23.4±1.2% at a temperature of 220$^{o}$C and is found to decrease to 20.8±1.1% and 16.9 ±0.8% as the electrolyte temperatures are increased to 250$^{o}$C and 280$^{o}$C respectively. The decrease in efficiencies observed with increasing temperatures is attributed to the lower open circuit voltages obtained at higher temperatures.

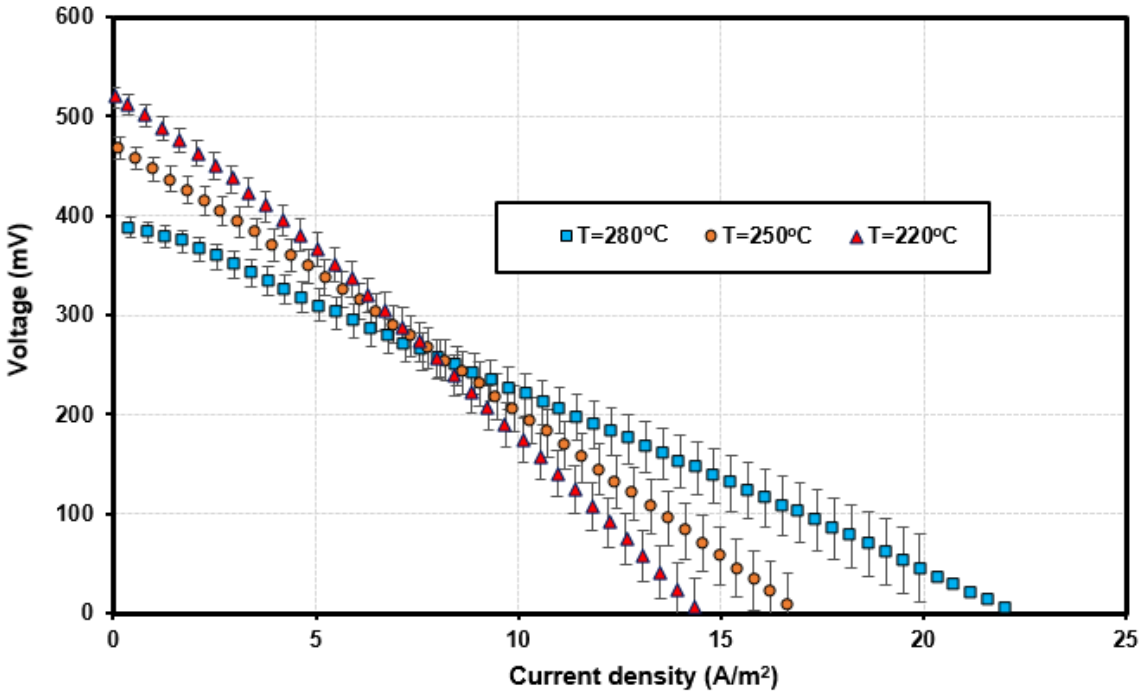


Fig. 5.33 Voltage vs current density curves for varying electrolyte temperatures for the molten alkaline electrolyte based direct ammonia fuel cell

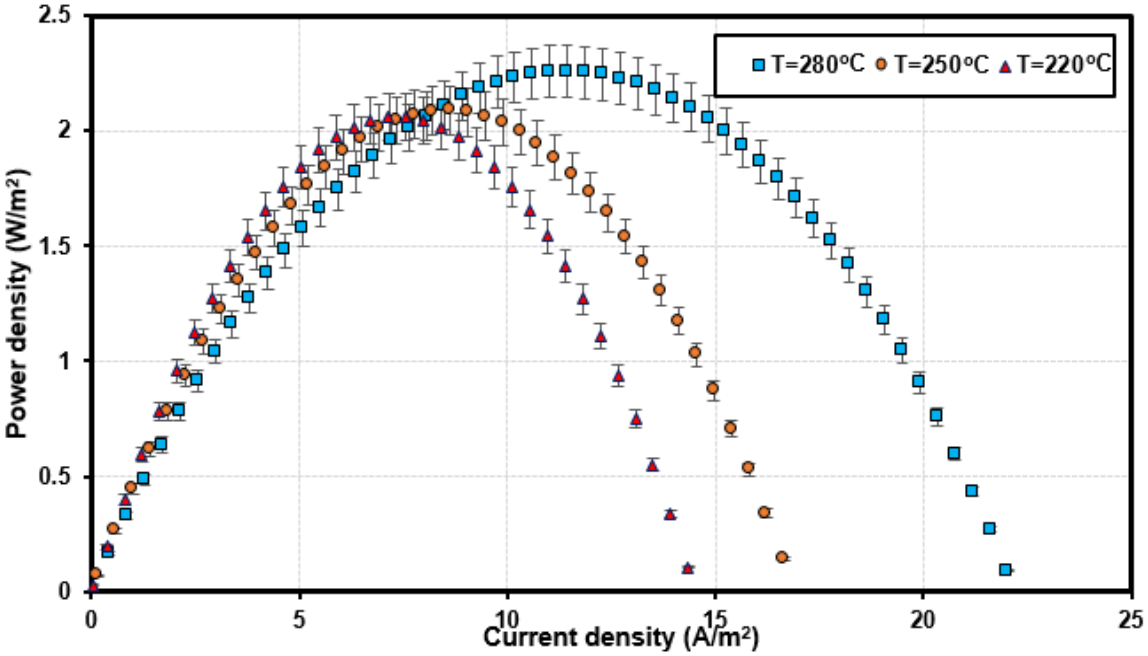


Fig. 5.34 Voltage vs current density curves for varying electrolyte temperatures for the molten alkaline electrolyte based direct ammonia fuel cell

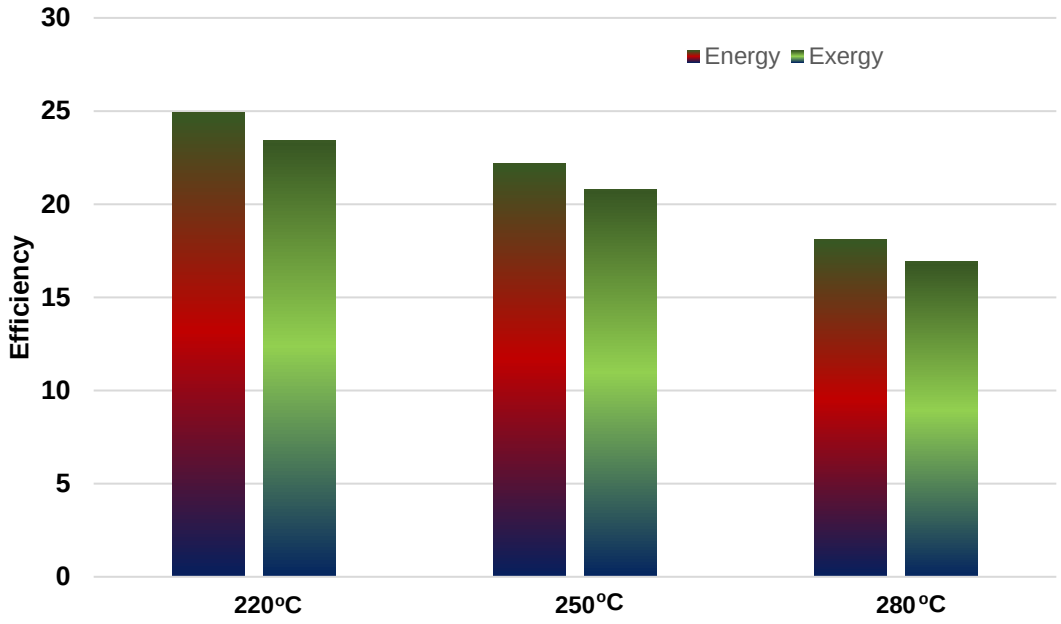


Fig. 5.35 Comparison of energy and exergy efficiencies of the molten alkaline electrolyte based direct ammonia fuel cell at varying electrolyte temperatures

### 5.8 Hybrid ammonia fuel cell and battery system results

In the present study, an electrochemical investigation of the proposed novel hybrid ammonia fuel cell and battery system is conducted, to investigate the performance of the proposed system. In addition, the effect of changing system parameters and conditions on the fuel cell and battery system is studied. The reversible fuel cell potential at standard conditions of 1 atm pressure and 25°C is evaluated as 0.54 V. The standard reversible battery voltage is calculated as 0.73 V. Fig. 5.36 depicts the comparison of open circuit voltages of the fuel cell and battery systems of the present study with a silver and copper electrode based TRAB [101] as well as CRRC [102] fuel cell system. Silver and copper electrode based regenerative ammonia batteries are found to have an open circuit voltage of 0.45 and 0.44 V respectively. The chemically regenerative redox cathode polymer electrolyte fuel cell is found to have an open circuit voltage of 0.65 V. In addition, the limiting current density of the fuel cell anode according to equation (4.9) is evaluated as 1.02 A/cm$^2$, and the cathodic limiting current density is calculated as 131 mA/cm$^2$. Furthermore, for the battery system, the cathodic and anodic limiting current densities are obtained as 337.7 mA/cm$^2$ and 131 mA/cm$^2$ respectively. The polarization curves obtained

for the fuel cell system for varying operating temperatures, electrolyte concentrations and input ammonia pressures are shown in Figures 5.37-5.43. Furthermore, the polarization curves for the battery system are shown in Figures 5.43-5.45. The variation of the of fuel cell energy and exergy efficiencies with the current density at varying operating temperatures and electrolyte concentrations is shown in Figures 5.39-5.42. The specific energy storage capacity of the nickel electrode is evaluated as 0.92 Ahr/g. Furthermore, the gravimetric energy density is evaluated as 563.1 kJ/kg. The efficiency of the battery system as described by equation (4.34) is evaluated as 75%. This indicates that in the proposed system, 75% of the stored chemical energy in the battery system, is converted to electrical energy. The 25% loss in the conversion efficiency can be attributed to the irreversibilities in the system. An ideal battery system with no irreversibilities would provide a conversion efficiency of 100%.

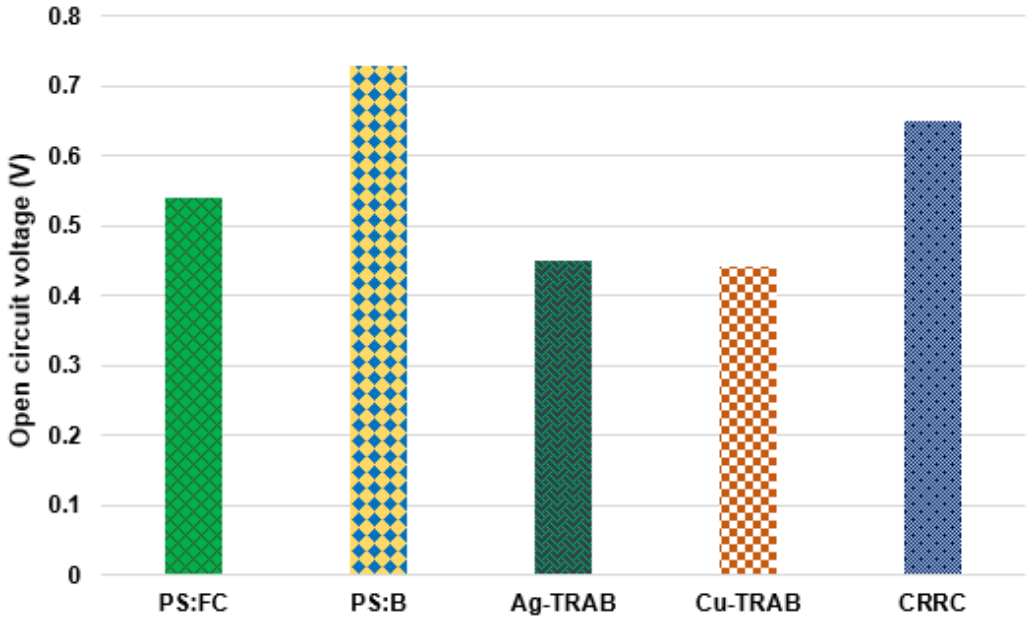


Fig. 5.36 Comparison of open circuit voltages between present study fuel cell system (PS:FC), present study battery system (PS:B), silver based thermally regenerative ammonia battery (Ag-TRAB), copper based thermally regenerative ammonia battery (Cu-TRAB) and chemically regenerative redox cathode (CRRC) polymer electrolyte fuel cell.

### 5.8.1 Effects of electrolyte concentration on the fuel cell and battery performance

The polarization curves for the fuel cell system at different KOH concentrations are shown in Fig. 5.33. In addition, Figures 5.43-5.45 depict the polarization curves of the battery system at varying concentrations of $NH_4Cl$ and $NiSO_4$ respectively. As can be depicted

from the figures, a significant activation polarization loss occurs in the fuel cell and battery systems. This is signified by the considerable voltage loss at initial increase of current density. The activation polarization loss is caused due to the reaction kinetics and the resistance to the specific electrochemical reaction. The activation polarization is a function of the current density and the exchange current density as can be observed from equation (4.6). Hence, the high activation polarization at low current densities is attributed to the low exchange current densities for electrochemical oxidation of ammonia and the reduction of nickel ions to nickel. Furthermore, increasing the KOH concentration is found to increase the open circuit voltage as well as the peak power density. At a KOH concentration of 1 M, the open circuit voltage is obtained as 0.54 V. However, as the concentration is increased to 5 M, the open circuit voltage increases to 0.58 V. This is attributed to the higher concentration of hydroxyl ions. At higher concentration of hydroxyl ions, the open circuit voltage increases according to Nernst equation. In addition, the peak power density is observed to increase from 22.78 mW/cm$^2$ at a concentration of 1 M to 28.13 mW/cm$^2$ at a KOH concentration of 5 M. The increase in power density is attributed to the increase in the voltage with increasing KOH concentration at the same current density.

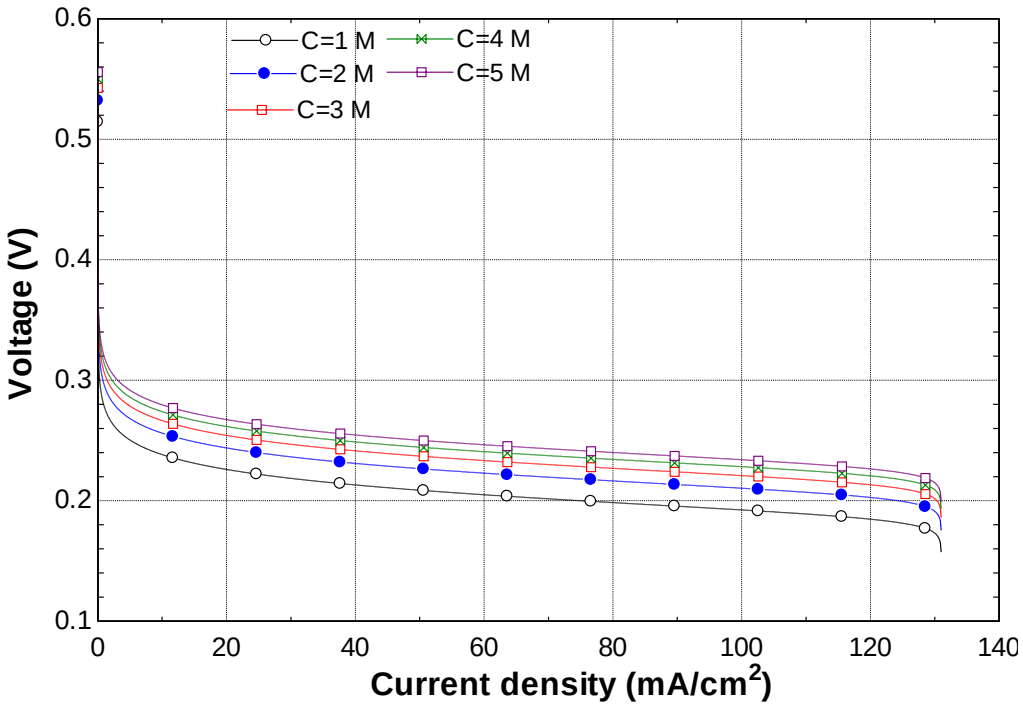


Fig. 5.37 Voltage Vs current density curves for different KOH concentrations for the fuel cell system.

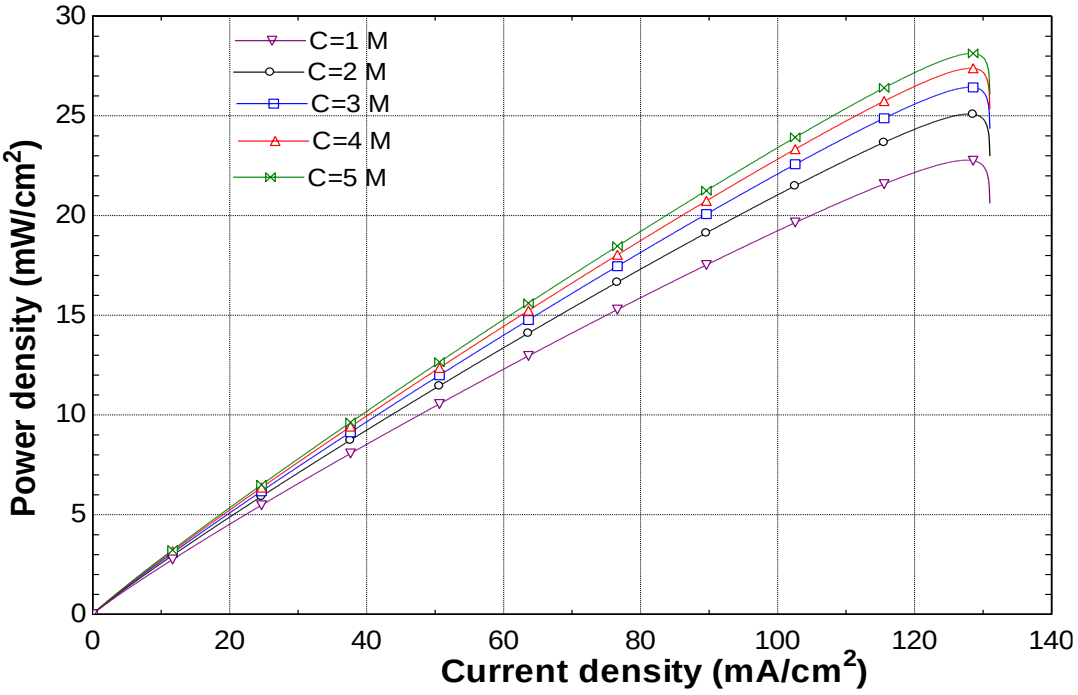


Fig. 5.38 Power density Vs current density curves for different KOH concentrations for the fuel cell system.

### 5.8.2 Effects of operating temperature on the fuel cell and battery performance

The effect of the operating temperature on the fuel cell performance is shown in Figures 5.39 and 5.40. In addition, Fig. 5.45 depicts the polarization curve for the battery system at varying operating temperatures. As can be observed from the figures, increasing the operating temperature increases the open circuit voltage and peak power density significantly. The open circuit voltage is observed to increase considerably to 0.89 V at an operating temperature of 85ºC from 0.54 V at a temperature of 25ºC for the fuel cell system. The effect of the operating temperature is analysed for constant electrolyte concentrations. The peak power density at a temperature of 25ºC and a KOH concentration of 1 M is evaluated as 22.78 mW $cm^{-2}$. However, as the operating temperature is increased to 85ºC, the peak power density is observed to increase to 72.6 mW $cm^{-2}$. Hence, the fuel cell performance is observed to enhance considerably with increasing temperature. The higher cell voltages, and thus the higher power densities at high temperatures can be attributed to the increase in the Gibbs function with temperature. The calculation of the Gibbs function is described in equation (4.1). The Gibbs function is observed to increase with increasing temperature.

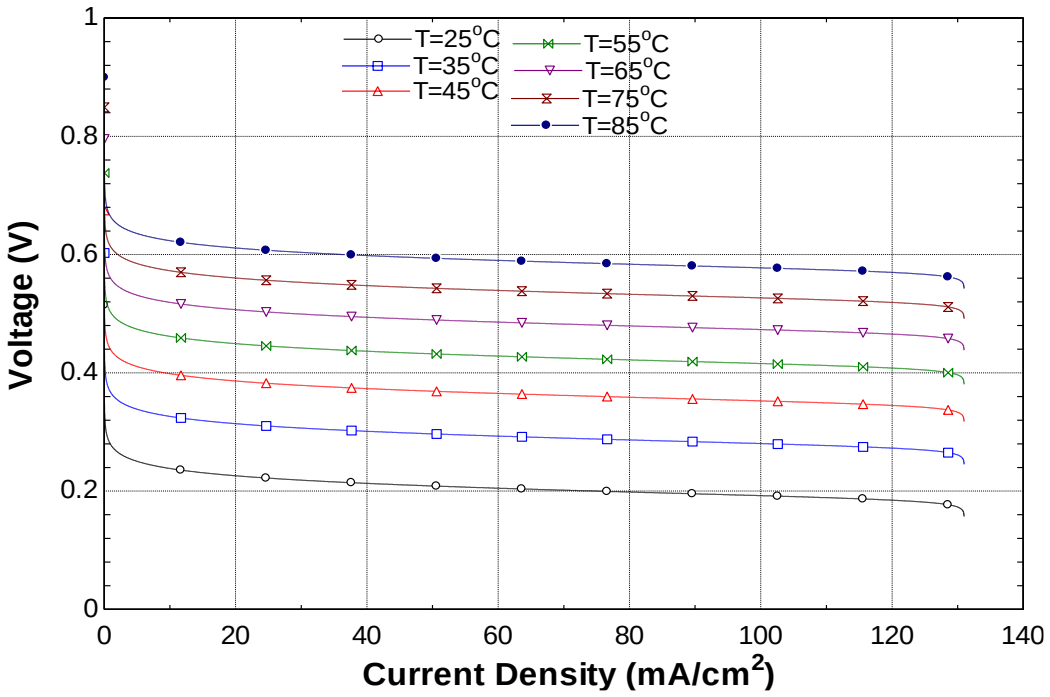


Fig. 5.39 Voltage Vs current density curves for different operating temperatures for the fuel cell system.

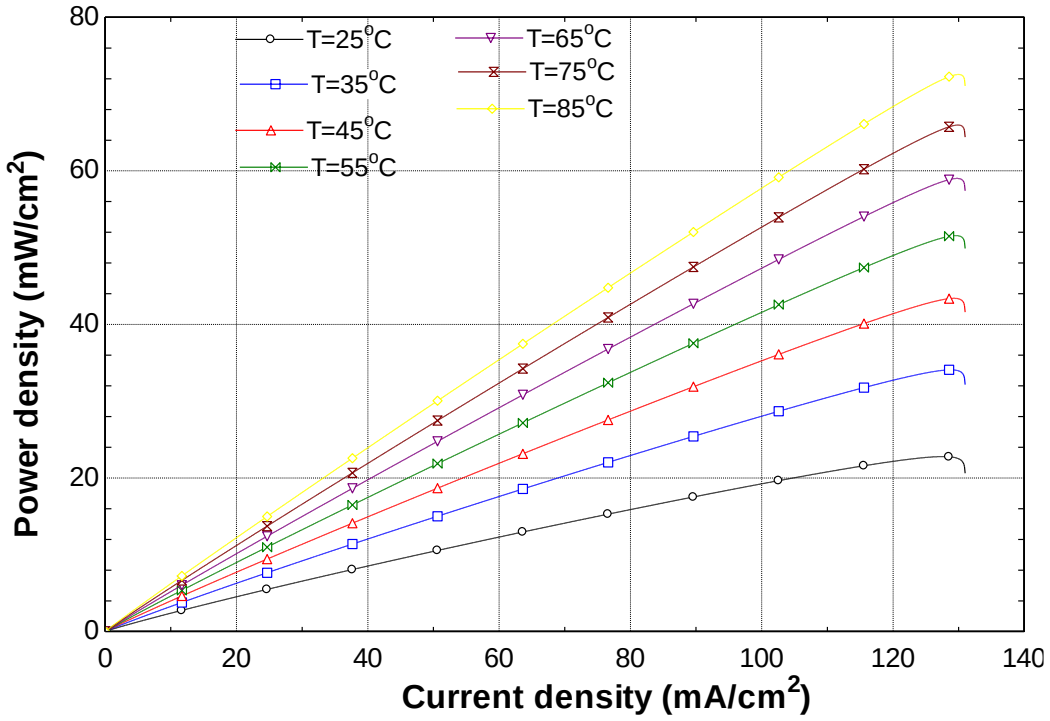


Fig. 5.40 Power density Vs current density curves for different operating temperatures for the fuel cell system

### 5.8.3 Effects of input ammonia pressure on the fuel cell performance

Ammonia is utilized as fuel in the fuel cell system. The input pressure of ammonia effects the fuel cell performance. The effect of input ammonia pressure on the fuel cell performance is shown in Figures 5.41 and 5.42. As the input pressure is increased, the open circuit voltage is also observed to increase. The open circuit voltage increases from 0.51 V to 0.53 V as the input pressure is increased from 101.25 kPa to 500 kPa. The peak power density is found to increase from 22.7 $mW/cm^2$ at input pressure of 101.25 kPa to 24.5 $mW/cm^2$ at an input ammonia pressure of 500 kPa. As the input pressure of ammonia is increased, the reversible potential is increased according to the Nernst equation. Hence, as higher cell voltages are obtained at the same current densities, higher power densities are obtained at the same current density values.

### 5.8.4 Effects of KOH concentration on the fuel cell energy and exergy efficiencies

The KOH concentration at the fuel cell anolyte affects the energy and exergy efficiencies. Figures 5.43 and 5.44 show the change in energy and exergy efficiencies with the current density at varying KOH concentrations and operating temperatures. The energy and exergy efficiencies are evaluated according to equations (4.32) and (4.33). The energy and exergy efficiencies are observed to decrease with increasing current density. For instance, the fuel cell energy and exergy efficiencies are evaluated as 57.8 % and 54.3% respectively at a current density of 0.1 $mA/cm^2$ at a KOH concentration of 1 M and a temperature of 25$^oC$. However, as the current density increased to 20 $mA/cm^2$, the energy and exergy efficiencies decreased to 41.1% and 38.7% respectively at the same conditions. The decrease in efficiencies is attributed to the increase in polarization losses with increasing current density. As the current density increases, the Ohmic losses in the cell also increase as denoted by equation (4.14). Furthermore, an increase in energy and exergy efficiencies is observed with increasing KOH concentration as can be depicted from Figures 5.39 and 5.40. For instance, at a KOH concentration of 1 M, the energy and exergy efficiencies are evaluated as 35.1% and 32.9% respectively at a current density of 100 $mA/cm^2$. However, as the concentration is increased to 5 M, the energy efficiency increases to 42.7% and the exergy efficiency increases to 40.1%. at the same current density. The increases in efficiencies is attributed to the increase in power densities. At higher concentrations, more hydroxyl ions are available for the electrochemical oxidation of ammonia.

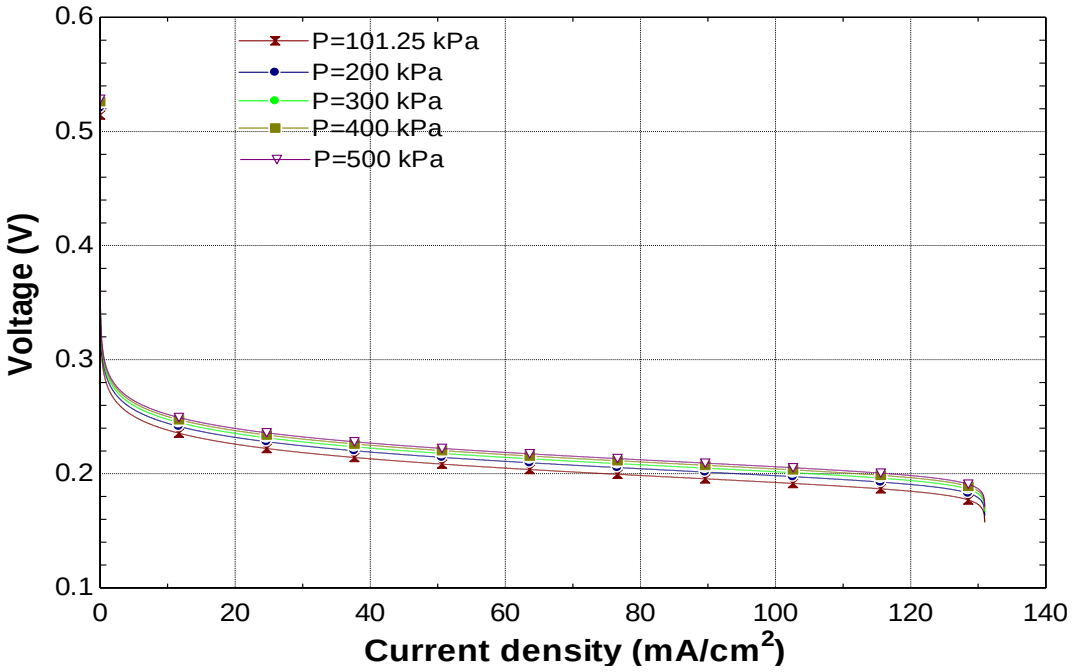


Fig. 5.41 Voltage Vs current density curves for different input ammonia pressures for the fuel cell system

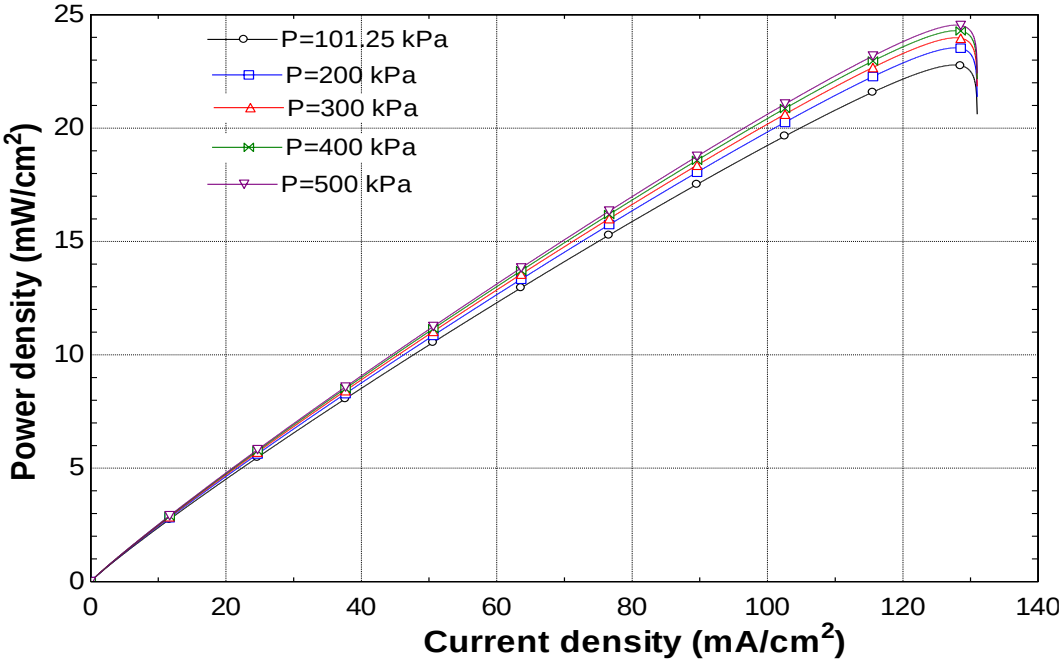


Fig. 5.42 Power density Vs current density curves for different input ammonia pressures for the fuel cell system

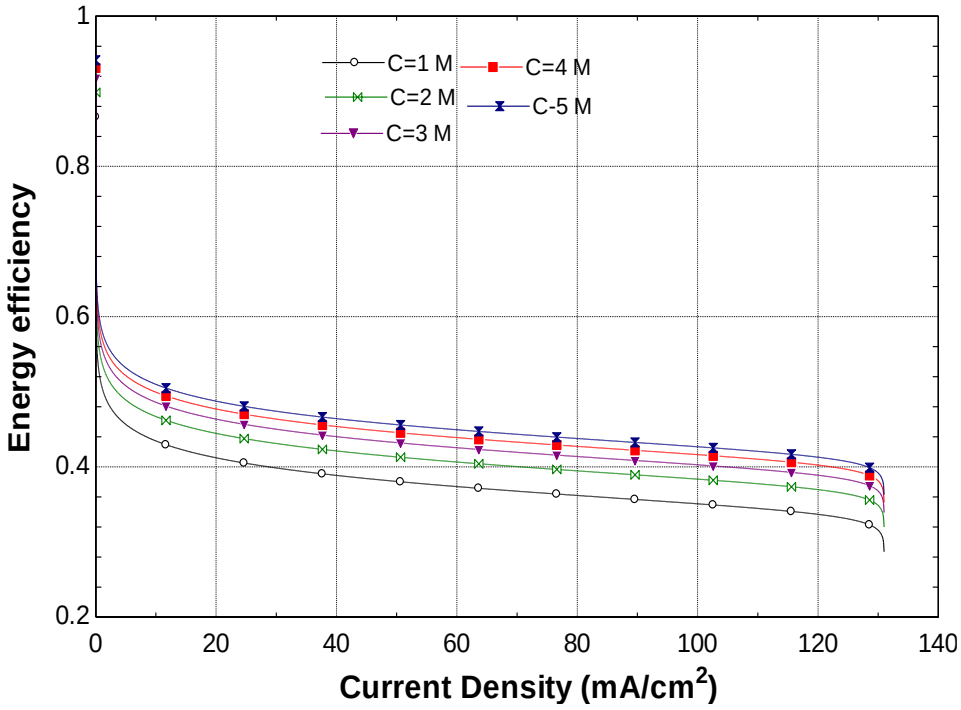


Fig. 5.43 Variation of fuel cell energy efficiency with current density at varying KOH concentrations

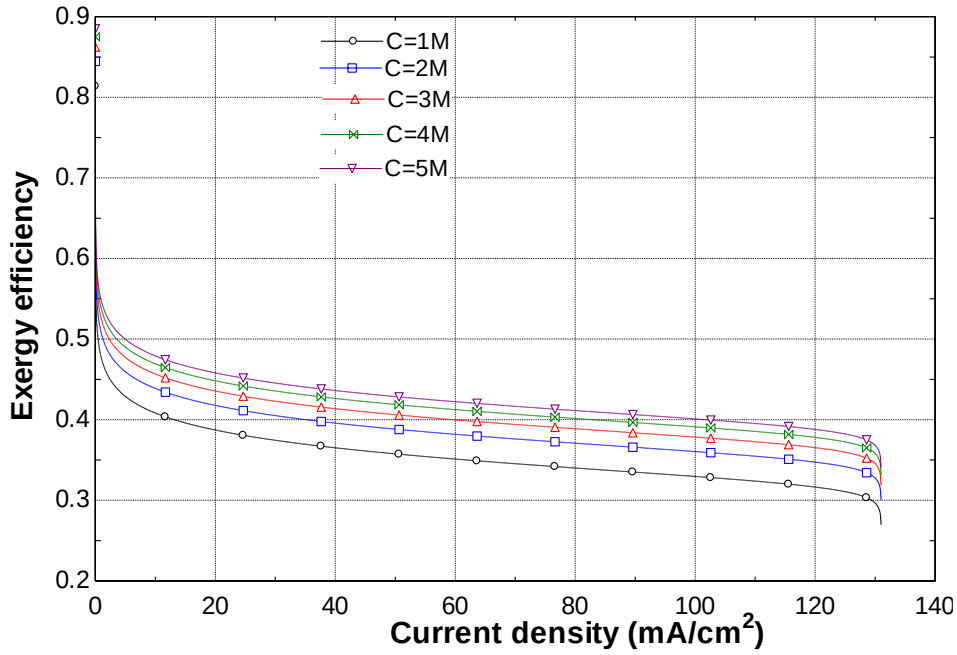


Fig. 5.44 Variation of fuel cell exergy efficiencies with current density at Varying KOH concentrations

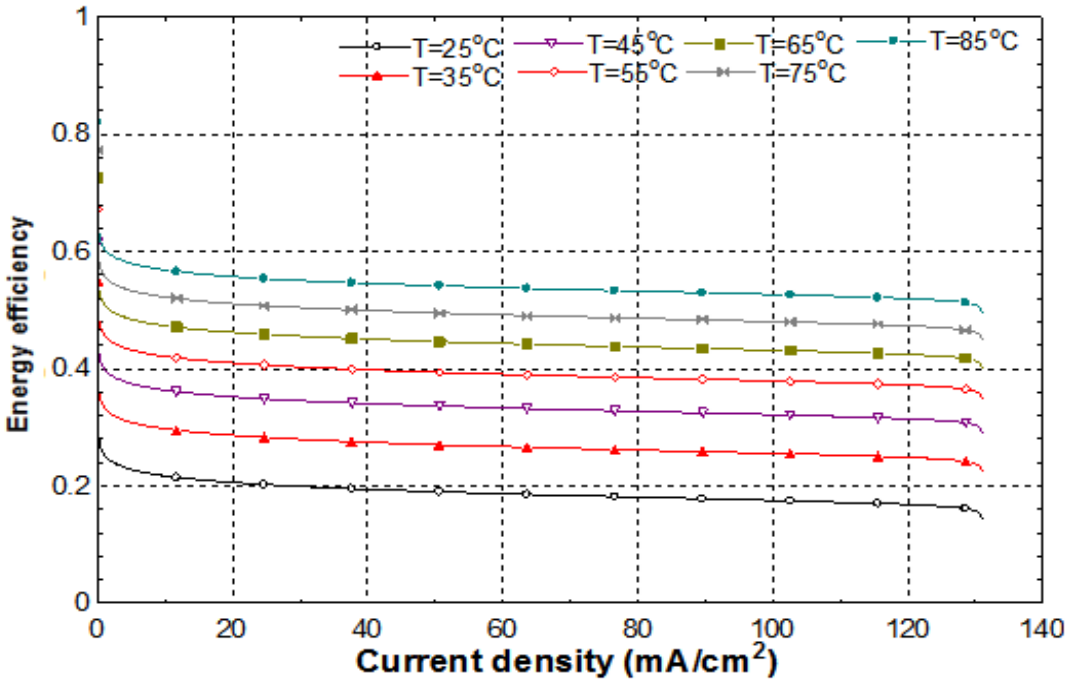


Fig. 5.45 Variation of fuel cell energy efficiencies with current density at varying operating temperatures.

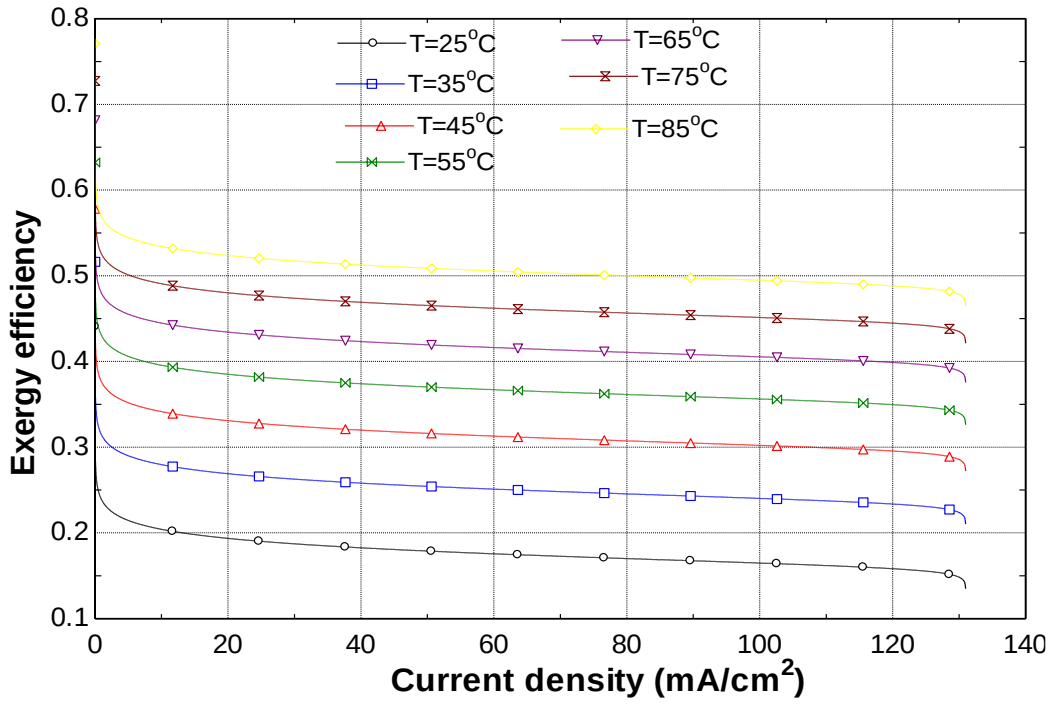


Fig. 5.46 Variation of fuel cell exergy efficiencies with current density at varying operating temperatures.

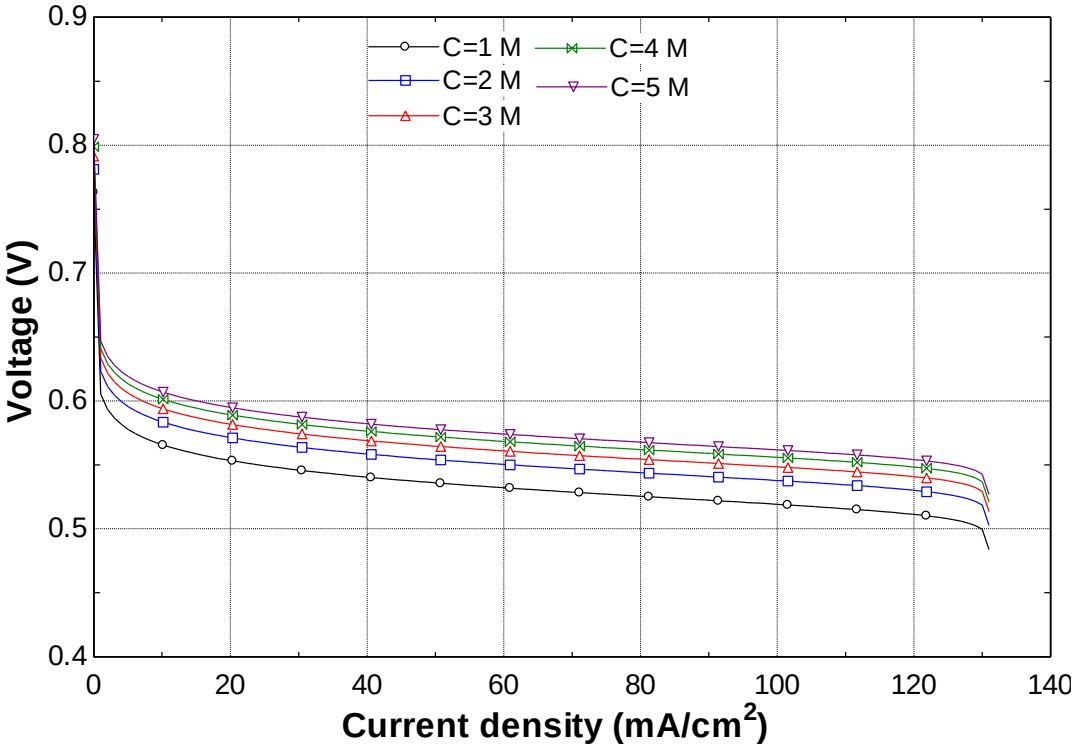


Fig. 5.47 Polarization curves for the battery system at different concentrations of $NH_4Cl$

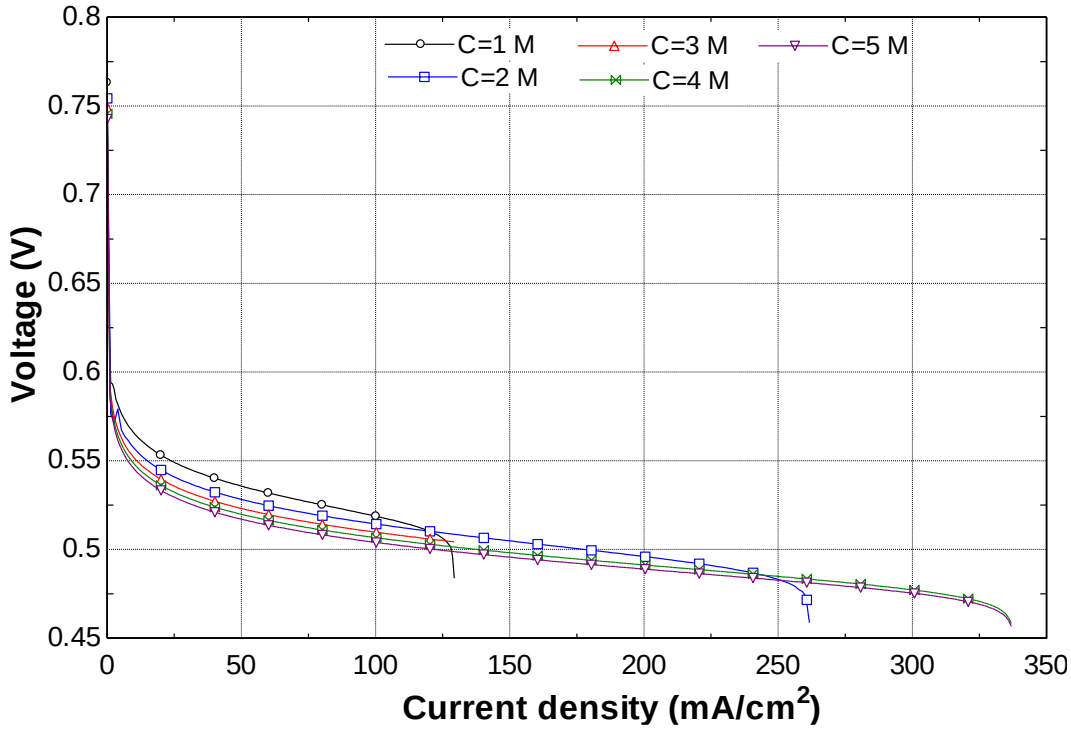


Fig. 5.48 Polarization curves for the battery system at different concentrations of $NiSO_4$

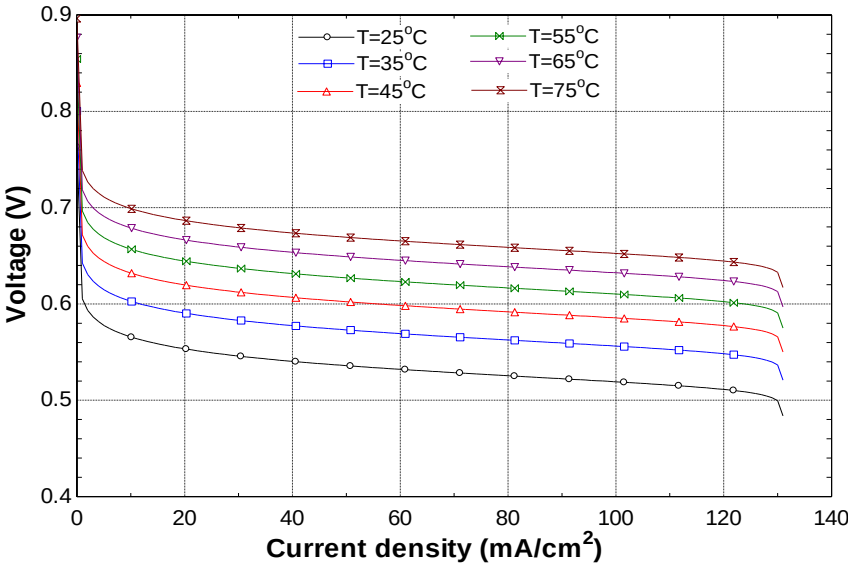


Fig. 5.49 Polarization curves for the battery system at different operating temperatures.

### 5.8.5 Advantages and disadvantages of the hybrid ammonia fuel cell and battery system

The proposed novel hybrid fuel cell and battery system provides a new method to utilize electrochemical energy through ammonia fuel cells. To provide a further comprehension of the proposed system, it is essential to analyse the pros and cons of the system as compared to other existing conventional fuel cell technologies. The advantages and disadvantages of the proposed system are listed in Table 5.3.

Table 5.3 Advantages and disadvantages of the novel hybrid ammonia fuel cell and battery system

| *Advantages* | *Disadvantages* |
|---|---|
| • Provides better utilization of electrochemical energy of ammonia by recharging the nickel electrode while operating on the fuel cell mode.<br>• Recycles the ammonia formed at the battery cathode during battery operation<br>• Provides a reversible fuel cell potential of 0.54 V is and a battery reversible voltage of 0.73 V.<br>• Circumvents the requirement of oxygen and water molecules as well as electrocatalyst for the electrochemical reaction of oxygen as in the case of conventional fuel cell systems. | • Requires re-circulation of potassium hydroxide as $OH^-$ ions are consumed during the electro-chemical oxidation of ammonia.<br>• Requires re-circulation of ammonium chloride as a battery catholyte as it is consumed during battery operation.<br>• Necessitates re-installation of manganese oxide battery cathode that is utilized during battery operation |

### 5.9 Comparison of energy and exergy efficiencies

A comparison of the energy and exergy efficiencies of the three types of developed direct ammonia fuel cell systems is depicted in Figure 5.50. The single-cell arrangement anion exchange membrane based direct ammonia fuel cell is found to have an energy and exergy efficiency of 15.2±1.3% and 14.4±1.2% respectively at the peak power densities. Comparatively, the molten salt alkaline electrolyte based direct ammonia fuel cell is found to have higher energy and exergy efficiencies of 24.9±1.3% and 23.4±1.2% respectively at an electrolyte temperature of 220$^{o}$C. Higher electrolyte temperatures are found to decrease the energy and exergy efficiencies of the cell. The hybrid system is evaluated to have higher efficiencies. The energy efficiency is evaluated to be 27.5% and the exergy efficiency is found to be 25% at nominal operating conditions.

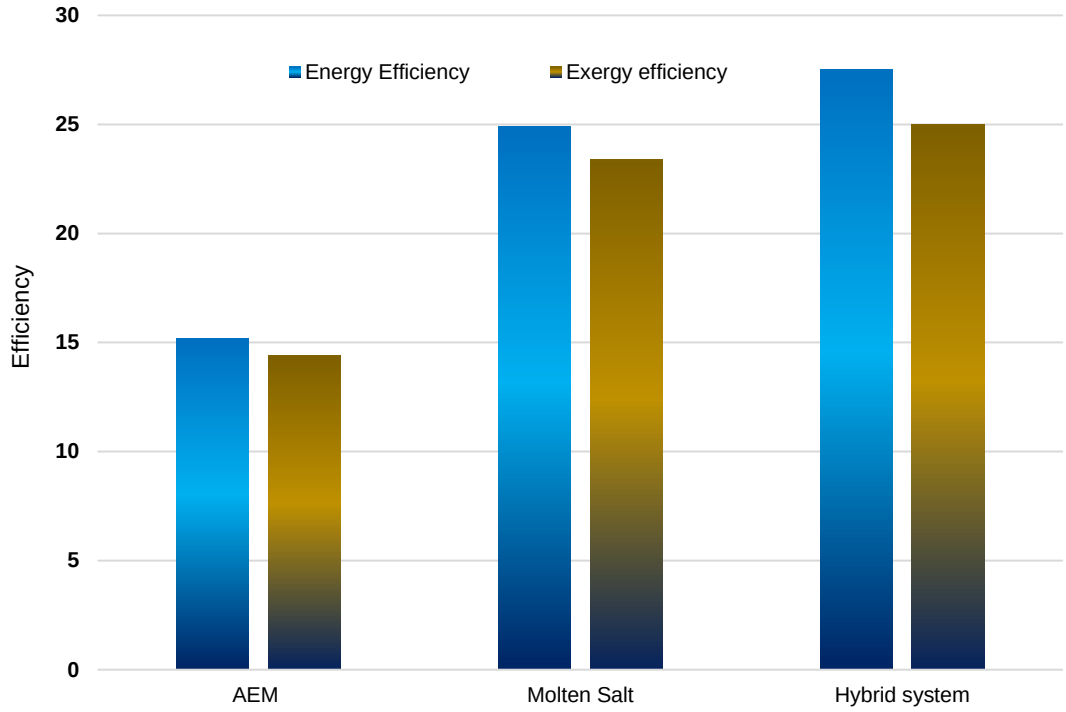


Fig. 5.50 A comparison of energy and exergy efficiencies of the developed direct ammonia fuel cell systems

# CHAPTER 6 : CONCLUSIONS AND RECOMMENDATIONS

In this chapter, conclusions of the conducted study are described by utilizing the main findings. In addition, recommendations for future work are provided in the following sub-section.

## 6.1 Conclusions

Alkaline electrolyte based direct ammonia fuel cells are developed and their performance investigated. A novel hybrid ammonia fuel cell and battery system is developed to better utilize electrochemical energy through a new regenerative electrode approach. For the cathodic fuel cell reaction, a nickel electrode is utilized that acts as the fuel cell cathode during fuel cell operation and battery cathode during cathode operation. Furthermore, an anion exchange membrane based direct ammonia fuel cell stack is developed and experimentally investigated. The humidifier temperatures are varied and the performance of fuel cell is investigated at each set of temperatures. Furthermore, aqueous ammonia is also investigated as a potential fuel for direct ammonia fuel cells. The developed fuel cell utilizes flow channel plates for convenient flow of reactant gases. The performance of the fuel cell is tested in the single-cell arrangement as well as with a five-cell stack arrangement. The humidifier temperatures are varied from ambient conditions of 25$^{o}$C to 80$^{o}$C. The results of the study indicated that an increase in humidifier temperature enhance the fuel cell performance in terms of the open circuit voltage, peak power density and short circuit current density due to lower polarization losses. Hence, higher temperatures can be utilized where possible for higher fuel cell performances. Furthermore, the fuel cell performance is observed to be significantly lower with aqueous ammonia as the fuel. This is attributed to lower ammonia electrochemical reaction sites with aqueous fuel. In addition, the five-cell stack performance is lower than expected from the single-cell arrangement results. Hence, addition of more cells increase the polarization losses. The primary quantitative findings of the present study are listed below:

- The average open circuit voltage for the single-cell anion exchange membrane is observed to be 279 mV at ambient conditions. Further, the average peak power density is observed to be 19.2 W/m$^2$. The fuel cell performance is observed to enhance with increasing humidifier temperatures. The open circuit voltage is

observed to increase by nearly 20.1% as the humidifier temperature is increased to 80$^{o}$C. Moreover, the average peak power density increased by 10.2% by the same temperature increase. The energy and exergy efficiencies of the developed fuel cell are found to be 15.2±1.3% and 14.4±1.2% respectively at the peak power densities.

- The single-cell average open circuit voltage obtained with a 10 wt% aqueous ammonia solution at ambient temperature is 110.2 mV and the average peak power density is observed to be 2.2 W/m$^2$. The solution temperatures are varied to analyse the effect on the fuel cell performance. The cell performance is observed to enhance with increasing temperatures. The open circuit voltage increased by 33.5% as compared to the voltage obtained at 25$^{o}$C. Furthermore, the average peak power density is observed to increase by 55%.
- The average open circuit voltage is observed to be 1185.3 mV at ambient conditions. An 18% increase in open circuit voltage is observed at humidifier temperatures of 65$^{o}$C. The peak power density is observed to be 35.9 W/m$^2$ at ambient conditions. A 20.8% increase in peak power density is observed. In addition, the average short circuit current density is observed to be 144 A/m$^2$ at a humidifier temperature of 60$^{o}$C. In addition, a 15.2 W/m$^2$ rise in the average peak power density is observed at a temperature of 80$^{o}$C. The five-cell stack performance is lower than expected from the single-cell arrangement results in terms of open circuit voltage and peak power density. This can be attributed to the increase in polarization losses due to the addition of more cell components.
- In the case of the molten salt alkaline electrolyte based direct ammonia fuel cell, at an operating temperature of 220$^{o}$C, the open circuit voltage is observed to be 520±26 mV. Furthermore, the peak power density at this electrolyte temperature is found to be 2.1±0.1 W/m$^2$. Higher electrolyte temperatures are observed to decrease the open circuit voltages and increase the short circuit current densities. The energy and exergy efficiencies are evaluated to be 24.9±1.3% and 23.4±1.2%.
- In the hybrid fuel cell-battery system, the reversible potentials of the fuel cell and battery systems are determined to be 0.54 V and 0.73 V respectively at standard conditions. The anodic limiting current density of the fuel cell system is evaluated as 1.02 A/cm$^2$. The fuel cell energy efficiency is evaluated to be 27.5% and the

exergy efficiency is found to be 25% at nominal operating conditions. The efficiency of the battery system is evaluated as 75%. The hybridized fuel cell and battery system provides a novel method to utilize electrochemical energy.

### 6.2 Recommendations

Based on the findings of the present study, several recommendation are made for future studies:

- Different mixtures of ammonia and other hydrogen containing fuels should be prepared and the fuel cell performances investigated with these fuels. Blending with other hydrogen containing fuels can enhance the performance of the direct ammonia fuel cell.
- New types of catalysts such as nickel, iron oxide, gold, rhenium, and iridium should be investigated for the electrochemical oxidation of ammonia. Better catalysts that can overcome the stable nature of ammonia need to be investigated. Ammonia has a lower reactivity as compared to hydrogen. Hence, in order to achieve similar fuel cell performances as with hydrogen fuel, the stable nature of ammonia molecules need to be further investigated.
- Exergoeconomic analysis should be conducted on the anion exchange membrane as well as the molten salt direct ammonia fuel cell.
- Life cycle assessment should be performed to better comprehend the environmental significance of direct ammonia fuel cells.
- Larger scale production should be carried out and the performances should be tested for large number of stacked cells.

## REFERENCES


[1] U.S. Energy Information Administration, "Monthly Energy Review," 2016.

[2] O. Siddiqui and I. Dincer, "Comparative assessment of the environmental impacts of nuclear, wind and hydro-electric power plants in Ontario: A life cycle assessment," *Journal of Cleaner Production*, vol. 164, pp. 848–860, 2017.

[3] Y. Yuksela, M. Ozturk, and I. Dincer, "Thermodynamic performance assessment of a novel environmentally-benign solar energy based integrated system," *Energy Conversion and Management*, vol. 119, pp. 109–120, 2016.

[4] I. Dincer, *Global warming : engineering solutions*. Springer, 2010.

[5] I. Dincer, C. O. Colpan, and F. Kadioglu, *Causes, impacts and solutions to global warming*. New York: Springer, 2013.

[6] A. Midilli, I. Dincer, and M. Ay, "Green energy strategies for sustainable development," *Energy Policy*, vol. 34, no. 18, pp. 3623–3633, 2006.

[7] I. Dincer, *Advanced power generation systems*, 1st ed. Elsevier, 2014.

[8] Y. Bicer and I. Dincer, "Life cycle evaluation of hydrogen and other potential fuels for aircrafts," *International Journal of Hydrogen Energy*, vol. 42, no. 16, 2017.

[9] I. Dincer, "Renewable energy and sustainable development: a crucial review," *Renewable and Sustainable Energy Reviews*, vol. 4, no. 2, pp. 157–175, 2000.

[10] REN 21, *Renewables 2016 global status report 2016*. 2016.

[11] I. Dincer, "Green methods for hydrogen production," *International Journal of Hydrogen Energy*, vol. 37, no. 2, pp. 1954–1971, 2012.

[12] E. Baniasadi, I. Dincer, and G. F. Naterer, "Exergy and environmental impact assessment of solar photoreactors for catalytic hydrogen production," *Chemical Engineering Journal*, vol. 213, pp. 330–337, 2012.

[13] I. Dincer, "Technical, environmental and exergetic aspects of hydrogen energy systems," *International Journal of Hydrogen Energy*, vol. 27, no. 3, pp. 265–285, 2002.

[14] S. Ghosh and I. Dincer, "Development and analysis of a new light-based hydrogen production system," *International Journal of Hydrogen Energy*, vol. 41, no. 19, pp. 7976–7986, 2016.

[15] I. Dincer, "Environmental and sustainability aspects of hydrogen and fuel cell systems," *International Journal of Energy Research*, vol. 31, no. 1, pp. 29–55, 2007.

[16] C. Acar and I. Dincer, "Impact assessment and efficiency evaluation of hydrogen production methods," *International Journal of Energy Research*, vol. 39, no. 13, pp. 1757–1768, 2015.

[17] Y. Kalinci, A. Hepbasli, and I. Dincer, "Biomass-based hydrogen production: A review and analysis," *International Journal of Hydrogen Energy*, vol. 34, no. 21,

pp. 8799–8817, 2009.

[18] A. Abuadala and I. Dincer, “A review on biomass-based hydrogen production and potential applications,” *International Journal of Energy Research*, vol. 36, no. 4, pp. 415–455, 2012.

[19] F. Suleman, I. Dincer, and M. Agelin-Chaab, “Comparative impact assessment study of various hydrogen production methods in terms of emissions,” *International Journal of Hydrogen Energy*, vol. 41, no. 19, pp. 8364–8375, 2016.

[20] F. Suleman, I. Dincer, and M. Agelin-Chaab, “Environmental impact assessment and comparison of some hydrogen production options,” *International Journal of Hydrogen Energy*, vol. 40, no. 21, pp. 6976–6987, 2015.

[21] E. Cetinkaya, I. Dincer, and G. F. Naterer, “Life cycle assessment of various hydrogen production methods,” *International Journal of Hydrogen Energy*, vol. 37, no. 3, pp. 2071–2080, 2012.

[22] U.S. Energy Information Administration, “U.S. Refinery Hydrogen Production Capacity as of January 1.” [Online]. Available: https://www.eia.gov/dnav/pet/hist/LeafHandler.ashx?n=PET&s=8_NA_8PH_NUS_6&f=A.

[23] U.S Department of Energy, “Hydrogen Storage Challenges.” 2018.

[24] U.S Department of Energy, “A Comparison of Hydrogen and Propane Fuels.” 2009.

[25] O. Siddiqui and I. Dincer, “A review and comparative assessment of direct ammonia fuel cells,” *Thermal Science and Engineering Progress*, vol. In Press, 2018.

[26] C. Zamfirescu and I. Dincer, “Using ammonia as a sustainable fuel,” *Journal of Power Sources*, vol. 185, no. 1, pp. 459–465, 2008.

[27] Y. Bicer and I. Dincer, “Life cycle assessment of nuclear-based hydrogen and ammonia production options: A comparative evaluation,” *International Journal of Hydrogen Energy*, vol. 42, no. 33, pp. 21559–21570, 2017.

[28] C. Zamfirescu and I. Dincer, “Ammonia as a green fuel and hydrogen source for vehicular applications,” *Fuel Processing Technology*, vol. 90, no. 5, pp. 729–737, 2009.

[29] E. Baniasadi and I. Dincer, “Energy and exergy analyses of a combined ammonia-fed solid oxide fuel cell system for vehicular applications,” *International Journal of Hydrogen Energy*, vol. 36, no. 17, pp. 11128–11136, 2011.

[30] F. Ishak, I. Dincer, and C. Zamfirescu, “Energy and exergy analyses of direct ammonia solid oxide fuel cell integrated with gas turbine power cycle,” *Journal of Power Sources*, vol. 212, pp. 73–85, 2012.

[31] E. Baniasadi, I. Dincer, and G. F. Naterer, “Exergoeconomic Analysis of a Combined Ammonia Based Solid Oxide Fuel Cell System,” *Fuel Cells*, vol. 12, no. 4, pp. 513–522, 2012.

[32] Y. Bicer, "Impact Assessment and Environmental Evaluation of Various Ammonia Production Processes," *Environmental management*, vol. 59, no. 5, pp. 842–855, 2017.

[33] C. Zamfirescu and I. Dincer, "Utilization of hydrogen produced from urea on board to improve performance of vehicles," *International Journal of Hydrogen Energy*, vol. 36, no. 17, pp. 11425–11432, 2011.

[34] J. Hogerwaard and I. Dincer, "Comparative efficiency and environmental impact assessments of a hydrogen assisted hybrid locomotive," *International Journal of Hydrogen Energy*, vol. 41, no. 16, pp. 6894–6904, 2016.

[35] Y. Bicer, I. Dincer, C. Zamfirescu, G. Vezina, and F. Raso, "Comparative life cycle assessment of various ammonia production methods," *Journal of Cleaner Production*, vol. 135, pp. 1379–1395, 2016.

[36] C. Zamfirescu and I. Dincer, "Thermodynamic performance analysis and optimization of a SOFC-H+ system," *Thermochimica Acta*, vol. 486, no. 1–2, pp. 32–40, 2009.

[37] I. Dincer and C. Zamfirescu, "A review of novel energy options for clean rail applications," *Journal of Natural Gas Science and Engineering*, vol. 28, pp. 461–478, 2016.

[38] C. Zamfirescu, "Ammonia as a green fuel for transportation," in *Proceedings of the 2nd International Conference on Energy Sustainability*, 2008, pp. 507–515.

[39] I. Dincer and C. Zamfirescu, "Potential options to greenize energy systems," *Energy*, vol. 46, no. 1, pp. 5–15, 2012.

[40] I. Dincer and C. Zamfirescu, "Renewable-energy-based multigeneration systems," *International Journal of Energy Research*, vol. 36, no. 15, pp. 1403–1415, 2012.

[41] M. Comotti and S. Frigo, "Hydrogen generation system for ammonia–hydrogen fuelled internal combustion engines," *International Journal of Hydrogen Energy*, vol. 40, no. 33, 2015.

[42] Z. Zhang, Z. Guo, Y. Chen, J. Wu, and J. Hua, "Power generation and heating performances of integrated system of ammonia–water Kalina–Rankine cycle," *Energy Conversion and Management*, vol. 92, pp. 517–522, 2015.

[43] I. Dincer, A. Hepbasli, A. Midilli, and T. Hikmet, *Global Warming*. Boston, MA: Springer, 2010.

[44] A. Fuerte, R. X. Valenzuela, M. J. Escudero, and L. Daza, "Ammonia as efficient fuel for SOFC," *Journal of Power Sources*, vol. 192, no. 1, pp. 170–174, 2009.

[45] X. Zhou, Y. Wang, and W. Wu, "Design and optimization of an ammonia fuel processing unit for a stand-alone PEM fuel cell power generation system," *International Journal of Energy Research*, vol. 41, no. 6, pp. 877–888, 2017.

[46] B. K.Boggs and G. G.Botte, "On-board hydrogen storage and production: An

application of ammonia electrolysis," *Journal of Power Sources*, vol. 192, no. 2, pp. 573–581, 2009.

[47] S. Ma, "Thermodynamic analysis of a new combined cooling, heat and power system driven by solid oxide fuel cell based on ammonia–water mixture," *Journal of power sources*, vol. 196, no. 20, pp. 8463–8471, 2011.

[48] T. Okanishi, K. Okura, A. Srifa, H. Muroyama, T. Matsui, M. Kishimoto, M. Saito, H. Iwai, H. Yoshida, T. Koide, S. Suzuki, Y. Takahashi, T. Horiuchi, H. Yamasaki, S. Matsumoto, S. Yumoto, H. Kubo, J. Kawahara, A. Okabe, Y. Kikkawa, T. Isomura, K. Eguchi, "Comparative Study of Ammonia-fueled Solid Oxide Fuel Cell Systems," *Fuel Cells*, no. 0, pp. 1–8, 2017.

[49] F. Schüth, R. Palkovits, R. Schlögl, and D. S. Su, "Ammonia as a possible element in an energy infrastructure: catalysts for ammonia decomposition," *Energy Environ. Sci.*, vol. 5, no. 4, pp. 6278–6289, 2012.

[50] "Yara International ASA," 2018. [Online]. Available: http://yara.com/doc/270416_2018-01-09_YAR_SEB_presentation.pdf.

[51] J. Bartels, "A feasibility study of implementing an Ammonia Economy," 2008.

[52] M. Appl, *Ammonia: principles and industrial practice*. WILEY-VCH, 1999.

[53] W. J. Van Zeist *et al.*, "LCI data for the calculation tool Feedprint for greenhouse gas emissions of feed production and utilization," 2012.

[54] R. D. Farr and C. G. Vayenas, "Ammonia High Temperature Solid Electrolyte Fuel Cell," vol. 127, no. 7, pp. 1478–1483, 1980.

[55] C. T. Sigal and C. G. Vayenas, "Nitric oxide in a solid electrolyte fuel cell," *Solid State Ionics*, vol. 5, pp. 567–570, 1981.

[56] Q. Ma, R. Peng, L. Tian, and G. Meng, "Direct utilization of ammonia in intermediate-temperature solid oxide fuel cells," *Electrochemistry Communications*, vol. 8, no. 11, pp. 1791–1795, 2006.

[57] G. Meng, C. Jiang, J. Ma, Q. Ma, and X. Liu, "Comparative study on the performance of a SDC-based SOFC fueled by ammonia and hydrogen," *Journal of Power Sources*, vol. 173, no. 1, pp. 189–193, 2007.

[58] M. Liu, R. Peng, D. Dong, J. Gao, X. Liu, and G. Meng, "Direct liquid methanol-fueled solid oxide fuel cell," *Journal of Power Sources*, vol. 185, no. 1, pp. 188–192, 2008.

[59] Z. Limin, C. You, Y. Weishen, and L. I. N. Liwu, "SHORT COMMUNICATION A Direct Ammonia Tubular Solid Oxide Fuel Cell," *Chinese Journal Of Catalysis*, vol. 28, no. 9, pp. 749–751, 2007.

[60] Q. Ma, J. Ma, S. Zhou, R. Yan, J. Gao, and G. Meng, "A high-performance ammonia-fueled SOFC based on a YSZ thin-film electrolyte," *Journal of Power Sources*, vol. 164, no. 1, pp. 86–89, 2007.

[61] G. G. M. Fournier, I. W. Cumming, and K. Hellgardt, "High performance direct ammonia solid oxide fuel cell," *Journal of Power Sources*, vol. 162, no. 1, pp. 198–206, 2006.

[62] A. Wojcik, H. Middleton, I. Damopoulos, and J. Van Herle, "Ammonia as a fuel in solid oxide fuel cells," *Journal of Power Sources*, vol. 118, no. 1–2, pp. 342–348, 2003.

[63] L. Pelletier, A. McFarlan, and N. Maffei, "Ammonia fuel cell using doped barium cerate proton conducting solid electrolytes," *Journal of Power Sources*, vol. 145, no. 2, pp. 262–265, 2005.

[64] N. Maffei, L. Pelletier, J. P. Charland, and A. McFarlan, "An intermediate temperature direct ammonia fuel cell using a proton conducting electrolyte," *Journal of Power Sources*, vol. 140, no. 2, pp. 264–267, 2005.

[65] N. Maffei, L. Pelletier, and A. McFarlan, "A high performance direct ammonia fuel cell using a mixed ionic and electronic conducting anode," *Journal of Power Sources*, vol. 175, no. 1, pp. 221–225, 2008.

[66] Q. Ma, R. Peng, Y. Lin, J. Gao, and G. Meng, "A high-performance ammonia-fueled solid oxide fuel cell," *Journal of Power Sources*, vol. 161, no. 1, pp. 95–98, 2006.

[67] L. Zhang and W. Yang, "Direct ammonia solid oxide fuel cell based on thin proton-conducting electrolyte," *Journal of Power Sources*, vol. 179, no. 1, pp. 92–95, 2008.

[68] A. McFarlan, L. Pelletier, and N. Maffei, "An Intermediate-Temperature Ammonia Fuel Cell Using Gd-Doped Barium Cerate Electrolyte," *Journal of The Electrochemical Society*, vol. 151, no. 6, p. A930, 2004.

[69] Y. Lin, R. Ran, Y. Guo, W. Zhou, R. Cai, J. Wang, Z. Shao, "Proton-conducting fuel cells operating on hydrogen, ammonia and hydrazine at intermediate temperatures," *International Journal of Hydrogen Energy*, vol. 35, no. 7, pp. 2637–2642, 2010.

[70] K. Xie, Q. Ma, B. Lin, Y. Jiang, J. Gao, X. Liu, G. Meng, "An ammonia fuelled SOFC with a BaCe0.9Nd0.1O3 thin electrolyte prepared with a suspension spray," *Journal of Power Sources*, vol. 170, no. 1, pp. 38–41, 2007.

[71] S. Antonio and A. Mcfarlan, "Renewable NH3 and Direct NH3 Fuel Cells : Canadian R & D for Clean Distributed Electricity Generation," in *9th Annual NH3 Fuel Conference*, 2012.

[72] N. Maffei, L. Pelletier, J. P. Charland, and A. McFarlan, "An ammonia fuel cell using a mixed ionic and electronic conducting electrolyte," *Journal of Power Sources*, vol. 162, no. 1, pp. 165–167, 2006.

[73] X. B. Zhang, S. Han, J. M. Yan, M. Chandra, H. Shioyama, K. Yasuda, N. Kuriyama, T. Kobayashi, Q. Xu, "A new fuel cell using aqueous ammonia-borane as the fuel," *Journal of Power Sources*, vol. 168, no. 1 SPEC. ISS., pp. 167–171, 2007.

[74] X. B. Zhang, J.M. Yan, S. Han, H. Shioyama, K. Yasuda, N. Kuriyama, Q. Xu, "A high performance anion exchange membrane-type ammonia borane fuel cell," *Journal of Power Sources*, vol. 182, no. 2, pp. 515–519, 2008.

[75] E. Gulzow, "Alkaline fuel cells: A critical view," *Journal of Power Sources*, vol. 61, no. 1–2, pp. 99–104, 1996.

[76] J. C. Ganley, "An intermediate-temperature direct ammonia fuel cell with a molten alkaline hydroxide electrolyte," *Journal of Power Sources*, vol. 178, no. 1, pp. 44–47, 2008.

[77] J. Yang, H. Muroyama, T. Matsui, and K. Eguchi, "Development of a direct ammonia-fueled molten hydroxide fuel cell," *Journal of Power Sources*, vol. 245, pp. 277–282, 2014.

[78] R. Lan and S. Tao, "Direct Ammonia Alkaline Anion-Exchange Membrane Fuel Cells," *Electrochemical and Solid-State Letters*, vol. 13, no. 8, p. B83, 2010.

[79] K. R. Lee, D. Song, S. B. Park, and J. Han, "A direct ammonium carbonate fuel cell with an anion exchange membrane," *RSC Advances*, vol. 4, pp. 5638–5641, 2014.

[80] S. Suzuki, H. Muroyama, T. Matsui, and K. Eguchi, "Fundamental studies on direct ammonia fuel cell employing anion exchange membrane," *Journal of Power Sources*, vol. 208, pp. 257–262, 2012.

[81] J. C. M. Silva, S.Silva, R. Souza, G. Buzzo, E. Spinacé, A. Neto, M. Assumpcao, "PtAu/C electrocatalysts as anodes for direct ammonia fuel cell," *Applied Catalysis A: General*, vol. 490, no. 133–138, 2015.

[82] "0.4 mg/cm$^2$ 40% Platinum on Vulcan - Carbon Paper Electrode." Available from: http://www.fuelcellstore.com/02-ptc-paper-electrode

[83] "Gamry Reference 3000 Potentiostat/Galvanostat/ZRA." Available from: https://www.gamry.com/potentiostats/reference-3000/

[84] "Mass and Volumetric Flow Meters - FMA-1600A Series Mass Flowmeters display Flow, Pressure and Temperature" Available from: https://www.omega.ca/pptst_eng/FMA1600.html

[85] "Portable Handheld Data Logger OM-DAQPRO-5300" Available from: https://www.omega.ca/pptst_eng/OM-DAQPRO-5300.html

[86] X. Li, *Principles of Fuel cells*. New York: Taylor & Francis, 2006.

[87] M. Orazem and B. Trobollet, *Electrochemistry. Electrochem. Impedance Spectrosc*. John Wiley & Sons, 2008.

[88] S. Asghari, A. Mokmeli, and M. Samavati, "Study of PEM fuel cell performance by electrochemical impedance spectroscopy," *International Journal of Hydrogen Energy*, vol. 35, pp. 9283–9290, 2010.

[89] C. Brunetto, A. Moschetto, and G. Tina, "PEM fuel cell testing by electrochemical impedance spectroscopy," *Electric Power Systems Research*, vol. 79, pp. 17–26, 2009.

[90] M. Pe´rez-Page and V. Pe´rez-Herranz, "Study of the electrochemical behaviour of a 300 W PEM fuel cell stack by Electrochemical Impedance Spectroscopy," *International Journal of Hydrogen Energy*, vol. 39, pp. 4009–4015, 2014.

[91] M. Mamlouk and K. Scott, "Analysis of high temperature polymer electrolyte membrane fuel cell electrodes using electrochemical impedance spectroscopy," *Electrochemica Acta*, vol. 56, pp. 5493–5512, 2011.

[92] X. Yuan, H. Wang, J. C. Sun, and J. Zhang, "AC impedance technique in PEM fuel cell diagnosis—A review," *International Journal of Hydrogen Energy*, vol. 32, pp. 4365–4380, 2007.

[93] O. Siddiqui and I. Dincer, "Analysis and performance assessment of a new solar-based multigeneration system integrated with ammonia fuel cell and solid oxide fuel cell-gas turbine combined cycle," *Journal of Power Sources*, vol. 370, pp. 138–154, 2017.

[94] I. Dincer and M. . Rosen, *Exergy: energy, environment and sustainable development*. Elsevier Science, 2012.

[95] C. Xu, A. Faghri, X. Li, and T. Ward, "Methanol and water crossover in a passive liquid-feed direct methanol fuel cel," *International Journal of Hydrogen Energy*, vol. 35, pp. 1769–1777, 2010.

[96] B. K. Kho, B. Bae, M. A. Scibioh, J. Lee, and H. Y. Ha, "On the consequences of methanol crossover in passive air-breathing direct methanol fuel cells," *Journal of Power Sources*, vol. 142, pp. 50–55, 2005.

[97] K. D. Baik, I. M. Kong, B. K. Hong, S. H. Kim, and M. S. Kim, "Local measurements of hydrogen crossover rate in polymer electrolyte membrane fuel cells," *Applied Energy*, vol. 101, pp. 560–566, 2013.

[98] Z. Qi and A. Kaufman, "Open circuit voltage and methanol crossover in DMFCs," *Journal of Power Sources*, vol. 110, pp. 177–185, 2002.

[99] S. A. Vilekar and R. Datta, "The effect of hydrogen crossover on open-circuit voltage in polymer electrolyte membrane fuel cells," *Journal of Power Sources*, vol. 195, pp. 2241–2247, 2010.

[100] E. C. M. Tse and A. A. Gewirth, "Effect of Temperature and Pressure on the Kinetics of the Oxygen Reduction Reaction," *The Jounal of Physical Chemistry A*, vol. 119, pp. 1246–1255, 2015.

[101] M. Rahimi, T. Kim, C. A. Gorski, and B. . Logan, "Development of a hybrid fuel cell/battery powered electric vehicle," *Journal of Power Sources*, vol. 373, pp. 95–102, 2018.

[102] D. . Ward, N. L. . Gunn, N. Uwigena, and T. J. Davies, "Performance comparison

of protonic and sodium phosphomolybdovanadate polyoxoanion catholytes within a chemically regenerative redox cathode polymer electrolyte fuel cell," *Journal of Power Sources*, vol. 375, pp. 68–76, 2018.